

ALMA MATER STUDIORUM - UNIVERSITA' DI BOLOGNA

ARCES - ADVANCED RESEARCH CENTER ON ELECTRONIC SYSTEM  
FOR INFORMATION AND COMMUNICATION TECHNOLOGIES E. DE CASTRO

EDITH - EUROPEAN DOCTORATE PROGRAM IN INFORMATION TECHNOLOGY

CYCLE XXI - ING-INF/01

**STATISTICAL METHODS FOR BIOMEDICAL  
SIGNAL ANALYSIS AND PROCESSING**

Ph.D. Thesis of

**Alessandro Palladini**

**Supervisor:**

**Professor Guido Masetti**

**Phd Coordinator:**

**Professor Claudio Fiegna**

January 2006 - March 2009



*"Those who seek should not stop seeking until they find.  
When they find, they will be disturbed.  
When they are disturbed, they will marvel, and will reign over all."*

*"Know what is in front of your face  
and what is hidden from you will be revealed to you.  
For there is nothing hidden that will not be revealed."*

Judas Thomas: 2,5



---

# Contents

---

<b>Contents</b>	<b>i</b>
<b>Introduction</b>	<b>iii</b>
<b>I BIOMEDICAL BACKGROUND</b>	<b>1</b>
<b>1 Ultrasound Imaging Systems</b>	<b>3</b>
1.1 Ultrasound physic . . . . .	3
1.2 Ultrasound imaging systems architecture . . . . .	15
1.2.1 Transmit section . . . . .	15
1.2.2 Receive section . . . . .	16
1.2.3 Probes . . . . .	17
1.2.4 Imaging modes . . . . .	19
1.3 Modeling and simulation of ultrasound imaging systems . . . . .	20
1.4 Future trends in ultrasound medical imaging . . . . .	20
<b>2 Ultrasound Aided Diagnosis of Prostate Cancer</b>	<b>23</b>
2.1 Prostate anatomy and pathologies . . . . .	23
2.2 Prostate cancer diagnosis procedure . . . . .	26
2.2.1 Digital rectal examination . . . . .	27
2.2.2 Prostatic specific antigen . . . . .	28
2.2.3 Prostate imaging . . . . .	28
2.2.4 TRUS guided biopsy protocols . . . . .	30
2.2.5 Cancer staging and risk assessment . . . . .	32
2.3 Future trends in US aided prostate cancer diagnosis . . . . .	34
<b>3 Neural signals analysis and modeling</b>	<b>37</b>
3.1 Brain structure and neurophysiology . . . . .	38
3.2 Experimental data and data analysis procedures . . . . .	41
<b>Bibliography</b>	<b>47</b>

<b>II APPLICATIONS</b>	<b>51</b>
<b>4 Ultrasound signal deconvolution</b>	<b>53</b>
4.1 Literature overview . . . . .	54
4.2 Proposed approach . . . . .	56
4.2.1 Estimation of system PSF . . . . .	57
4.2.2 Statistical approach to regularized inversion . . . . .	57
4.2.3 US radio frequency signal model . . . . .	60
4.3 Viterbi algorithm based deconvolution . . . . .	61
4.3.1 Viterbi algorithm . . . . .	64
4.3.2 Computational cost reduction . . . . .	65
4.4 Algorithm performance . . . . .	67
4.5 Disussion . . . . .	68
<b>Bibliography</b>	<b>77</b>
<b>5 Ultrasound signal segmentation and classification</b>	<b>81</b>
5.1 Ultrasound image segmentation . . . . .	82
5.2 Ultrasound aided tissue characterization . . . . .	86
5.3 Proposed system for ultrasound-aided prostate cancer diagnosis . . . . .	91
5.3.1 Regions of interest segmentation algorithm . . . . .	91
5.3.2 Feature estimation and selection for ROI characterization . . . . .	97
5.3.3 Classification . . . . .	98
5.4 Experimental results . . . . .	100
5.5 Discussion . . . . .	102
<b>Bibliography</b>	<b>107</b>
<b>6 Primate behavioural tasks modelling</b>	<b>111</b>
6.1 Third generation neural networks and liquid state machines . . . . .	111
6.2 Proposed model . . . . .	116
6.2.1 Behavioural tasks modelling and information representation . . . . .	116
6.2.2 Network architecture . . . . .	118
6.2.3 Model parameters tuning and network training . . . . .	121
6.3 Performance evaluation . . . . .	126
6.3.1 Linear classifier. . . . .	126
6.3.2 SVM classifier. . . . .	126
6.4 Discussion . . . . .	131
<b>Bibliography</b>	<b>135</b>

---

# Introduction

---

Statistical modelling and statistical learning theory are two powerful analytical frameworks for analyzing signals and developing efficient processing and classification algorithms. In this thesis, these frameworks are applied for modelling and processing biomedical signals in two different contexts: ultrasound medical imaging systems and primate neural activity analysis and modelling.

## Ultrasound medical imaging systems

In the context of ultrasound medical imaging, two main applications are explored: deconvolution of signals measured from a ultrasonic transducer and automatic image segmentation and classification of prostate ultrasound scans.

In the former application a stochastic model of the radio frequency signal measured from a ultrasonic transducer is derived. This model is then employed for developing in a statistical framework a regularized deconvolution procedure, for enhancing signal resolution.

In the latter application, different statistical models are used to characterize images of prostate tissues, extracting different features. These features are then used to segment the images in region of interests by means of an automatic procedure based on a statistical model of the extracted features. Finally, machine learning techniques are used for automatic classification of the different region of interests.

## Primate neural activity analysis and modelling

In the context of neural activity signals, an example of bio-inspired dynamical network was developed to help in studies of motor-related processes in the brain of primate monkeys. The presented model aims to mimic the abstract functionality of a cell population in 7a parietal region of primate monkeys, during the execution of learned behavioural tasks. This project was developed during an internship of six months at the Laboratory of Nonlinear Systems (LANOS) of the Polytechnical federal School of Lausanne - Switzerland, under the supervision of prof. Martin Hasler.

## Thesis structure

This thesis is organized in two parts. In part I the biomedical background concerning ultrasound medical imaging system (Chapter 1), prostate cancer diagnosis (Chapter 2) and neural signal analysis (Chapter 3). This part is meant to give the basic notions about the application context of the different project developed in this thesis. A common bibliography with the fundamental reference is given at the end of the part.

In part II the three main projects developed in this work are reviewed in detail. For each project, a dedicated bibliography is given at the end of the correspondent chapter.

In chapter 4, after a complete and original review on the state of the art of ultrasound signal deconvolution method, a novel stochastic model for the radio frequency signal recorded from ultrasound imaging system is presented. The model is then used in a MAP estimation framework for the development of a novel deconvolution algorithm, based on a reduced complexity Viterbi algorithm and an adaptive scalar quantization method. The proposed method is then applied on both synthetic and real *in vivo* signals.

In chapter 5, ultrasound signal characterization technique and machine learning method are used for the development of a computer aided procedure for prostate cancer diagnosis. The core of the proposed method is an automatic selection of region of interest to be classified based on an supervised and adaptive segmentation technique. The regions of interest are then classified with a supervised classifier trained and tested on a experimental database of *transrectal* prostate images.

In chapter 6, an abstract mathematical model of primate 7a area, based on a recurrent network of spiking neurons is developed. Such model was developed in order to assess the effect of some critical parameters in data analysis procedures conducted on real neural activity recorded from 7a area of primate monkey.

# Part I

## BIOMEDICAL BACKGROUND



## Chapter 1

---

# Ultrasound Imaging Systems

---

### 1.1 Ultrasound physic

Sound is related to the vibration motion of particles that constitute a material. In the linear acoustic theory, the propagation of sound is described through the model of elastic waves. Elastic waves are related to elastic material, i.e. material that follow Hooke's law.

In elastic waves, two types of wave can exist: transversal waves and longitudinal waves. For transverse waves the displacement of the medium is perpendicular to the direction of propagation of the wave. Transverse waves cannot propagate in a gas or a liquid because there is no mechanism for driving motion perpendicular to the propagation of the wave. In longitudinal waves the displacement of the medium is parallel to the propagation of the wave. Bones excluded, in all the biological tissue the transversal component is subject to an high attenuation and therefore it can be neglected.

The constitutive equations for a linear and lossless homogeneous medium are:

$$\rho_0 c^2 \nabla \cdot \bar{v} = -\frac{\partial p}{\partial t} \quad (1.1)$$

$$\nabla p = -\rho_0 \frac{\partial \bar{v}}{\partial t} \quad (1.2)$$

where  $p$  is the pressure associated to the perturbation of a particle with speed  $\bar{v}$ ,  $c$  is the propagation speed and  $\rho_0$  is the mass density in resting condition.

The wave equation for a lossless linear medium in absence of sources can be obtained differentiating eq.(1.2) with respect to  $t$  and multiplying both the terms of (1.2) for  $\nabla$ . Combining the two equations we obtain:

$$\nabla^2 p = \frac{1}{c^2} \frac{\partial^2 p}{\partial t^2} \quad (1.3)$$

that together with the initial conditions and boundary conditions, describes the propagation of the pressure field  $p$ .

**Velocity potential** The solution to wave equation can be simplified introducing the scalar function velocity potential:

$$\bar{v}(\bar{r}, t) = -\nabla \Phi(\bar{r}, t) \quad (1.4)$$

which allows to express the pressure field as

$$p(\vec{r}, t) = -\rho_0 \frac{\partial \Phi(\vec{r}, t)}{\partial t}. \quad (1.5)$$

This function will be used in the following sections to find the expression of the ultrasound field generated by a transducer.

### Solution of the homogeneous wave equation in Cartesian coordinate system

Wave eq. (1.3) can be solved with separation of variables method, expressing the solution in the exponential form:

$$p(\vec{r}, t) = A e^{j(\omega t - \vec{k} \cdot \vec{r})} \quad (1.6)$$

where  $\vec{k} = k_x \hat{x} + k_y \hat{y} + k_z \hat{z}$  is the wave vector.

To be solution of the eq. (1.3) we must have

$$k = k_x^2 + k_y^2 + k_z^2 = \frac{\omega^2}{c^2}$$

where  $k_i$  is the component along direction  $i$  of the wave vector. Therefore, eq. (1.3) admit an infinite number of solutions called plane waves.

**Acoustical impedance.** Let's consider a plane wave that propagates along the direction  $\hat{x}$

$$p(x, t) = A \exp\{j(\omega t - k_x x)\}$$

the speed of the particle oscillation around the propagation direction  $v$  can be obtained from the relation (1.2). We define acoustical impedance the quantity

$$Z = \frac{p}{v}. \quad (1.7)$$

This parameter has the physical dimension of a mechanical resistance and its unit of measured is called rail =  $\frac{kg}{sm^2}$ . The impedance for a plane wave is therefore

$$Z = \rho_0 c \quad (1.8)$$

that is related to propagation speed and to the density of the material. In tab. 1.1 values of propagation speed, mass density and impedance for several materials an biological tissues are reported.

**Acoustical intensity.** It is defined as the power of the acoustic field for surface unit along the propagation direction:

$$I = \lim_{T \rightarrow \infty} \frac{1}{T} \int_T p(t) v(t) dt \quad (1.9)$$

### Reflection and refraction of plane waves

The solution of eq. (1.3) found previously is valid only for an homogeneous region. If in the propagation medium are present discontinuities, both macroscopic and microscopic with respect to the field wavelength, it is still possible to describe the propagation in terms of plane wave introducing diffraction, refraction and diffusion phenomena.

Material	Speed of sound (m/s)	Density (Kg/m <sup>3</sup> )	Impedance ( $\mu$ rail)	Tissue	Speed of sound (m/s)	Density (Kg/m <sup>3</sup> )	Impedance ( $\mu$ rail)
Air	331	1.02	0.0004	Muscles	1580	1070	1.70
Water	1480	1000	1.48	Liver	1550	1060	1.64
Mercury	1450	13600	11.4	Fat	1459	920	1.38
Quarz	5736	2200	12.4	Brain	1560	1028	1.56
PZT	3791	7650	29.0	Kidney	1560	1040	1.62
				Spleen	1570	1059	1.66
				Blood	1575	1060	1.66
				Bones	4080	1620	6.6
				Eye	1670	1135	
				Lungs	650	430	0.28

(a)

(b)

**Table 1.1:** Speed of sound, mass density and acoustical impedance in some common materials (a) and biological tissues (b).

INTERFACE	REFLECTION
soft tissue - air	0.99
soft tissue - lung	0.52
soft tissue - bone	0.43
vitreous humor - eye lens	0.01
fat - liver	0.79
soft tissue - fat	0.0069
soft tissue - muscle	0.0004
water - lucote	0.13
oil - soft tissue	0.0043

**Table 1.2:** Reflection coefficient for common interfaces in medical field.

If in the propagation medium are present non homogeneous regions with dimension larger than the field wavelength, propagation medium can be modelled as a discrete set of homogeneous regions characterized by different acoustical properties and reflection and refraction phenomena can be modelled with the geometric acoustic theory.

In this model, when a plane wave encounter the separation surface between two homogeneous regions with propagation speed  $c_1$  and  $c_2$ , and acoustical impedance  $Z_1$  and  $Z_2$ , the incidence angle  $\theta_i$  is related to the reflection angle  $\theta_r$  and to the refraction angle  $\theta_t$  by the Snell's law:

$$\frac{\sin \theta_i}{\sin \theta_t} = \frac{c_1}{c_2}. \quad (1.10)$$

Reflection coefficient  $R$  and refraction coefficient  $T$ , which give the amplitude of the reflected and refracted wave respectively, can be computed as

$$R = \frac{Z_2 - Z_1}{Z_2 + Z_1} \quad T = \frac{2Z_2}{Z_2 + Z_1}. \quad (1.11)$$

Similarly, reflection and refractions coefficients can be defined for the acoustical intensity:

$$R = \left( \frac{Z_2 - Z_1}{Z_2 + Z_1} \right)^2 \quad T = \frac{4Z_1Z_2}{(Z_2 + Z_1)^2} \quad (1.12)$$

Eq. (1.11) and (1.12) show that while refraction is dependent on the propagation direction the reflection depends only on the impedance mismatch between the two regions. In tab.1.2, several values of reflection coefficients for several common interfaces in medical field.

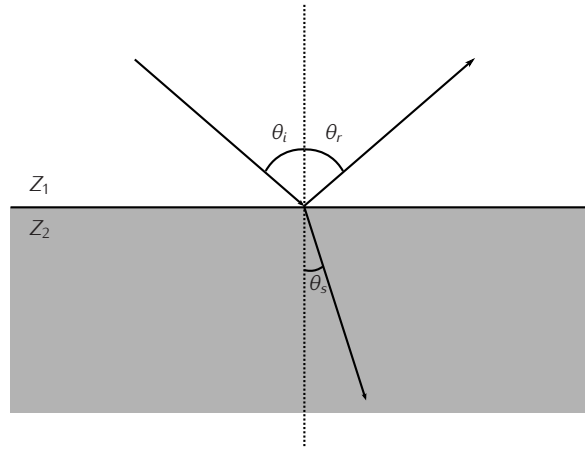


Figure 1.1: Reflection and refraction of plane waves in Snell law.

### Diffusion

If the non homogeneous regions present in the propagation medium have dimension lower or comparable with the field wavelength, the incident wave will be diffused towards different directions according to a radiation patter that is function of the field wavelength and of obstacle geometry. When the dimensions of the non homogeneous region are negligible with respect to the field wavelength, the obstacle can be modelled as a point scatter. In this case, the incident field is diffused uniformly along all the directions in the form of spherical waves.

Such phenomena takes place also when the non homogeneous regions are globally larger than the wavelength but are characterized by local structures with dimension comparable or lower than the filed wavelength. In this case the reflected field is composed by two components: a reflected wave which follows the Snell's law and a diffused (or non coherent) wave which propagates along all the direction with different phase and cause a destructive interference, often referred as speckle.

The diffusion phenomena can be analytically studied through the wave equation for a lossless non homogeneous medium. In particular, let's suppose that the acoustic parameters in the non homogeneous regions are slowly varying and all located in a region  $V$ , such that mass density and adiabatic compressibility can be written as

$$\rho(\vec{r}) = \begin{cases} \rho_0 + \rho_1(\vec{r}) & \vec{r} \in V \\ \rho_0 & \text{otherwise} \end{cases} \quad (1.13)$$

$$\beta(\vec{r}) = \begin{cases} \beta_0 + \beta_1(\vec{r}) & \vec{r} \in V \\ \beta_0 & \text{otherwise} \end{cases} \quad (1.14)$$

Imposing the boundary conditions on  $V$

$$\frac{\partial \rho(\vec{r})}{\partial n} = \frac{\partial \beta(\vec{r})}{\partial n} = 0 \quad (1.15)$$

the wave equation becomes

$$\nabla^2 p(\vec{r}, t) - \frac{1}{c^2} \frac{\partial^2 p(\vec{r}, t)}{\partial t^2} = \frac{1}{c^2} \frac{\partial^2 p(\vec{r}, t)}{\partial t^2} \tilde{\beta}(\vec{r}) + \nabla \cdot [\tilde{\rho}(\vec{r}) \nabla p(\vec{r}, t)] \quad (1.16)$$

where

$$\begin{aligned}\tilde{\rho}(\bar{r}) &= \frac{\rho(\bar{r})}{\rho_0} \\ \tilde{\beta}(\bar{r}) &= \frac{\beta(\bar{r})}{\beta_0}\end{aligned}$$

are the relative mass density function and the relative compressibility function in the region  $V$ , respectively. The eq. (1.16) constitutes a non homogeneous differential problem, which can be solved through the Green's function method [12]:

$$p(\bar{r}, t) = p_i(\bar{r}, t) + p_s(\bar{r}, t) \quad (1.17)$$

where  $p_i(\bar{r}, t)$  it's the solution of the homogeneous problem, i.e. the incident field, and

$$p_s(\bar{r}, t) = \int_{-\infty}^{\infty} dt_0 \int_V \left[ \frac{1}{c^2} \frac{\partial^2 p(\bar{r}, t)}{\partial t^2} \tilde{\beta}(\bar{r}_0) + \nabla \cdot [\tilde{\rho}(\bar{r}_0) \nabla p(\bar{r}_0, t_0)] G(\bar{r}, t | \bar{r}_0, t_0) \right] d^3 \bar{r}_0 \quad (1.18)$$

is the field diffused by the region  $V$ , while  $(\bar{r}, t)$  and  $(\bar{r}_0, t_0)$  are the respectively the target and source point of the Green's function

$$G(\bar{r}, t | \bar{r}_0, t_0) = \frac{\delta(t - t_0 - |\bar{r}_0 - \bar{r}|/c)}{4\pi |\bar{r} - \bar{r}_0|} \quad (1.19)$$

of the differential problem (1.16).

The eq. (1.18) has analytical solutions only if the integration region  $V$  has a simple geometry and a general solution can be found only doing some approximations. In particular, recurring to the Born approximation  $p(\bar{r}, t) = p_i(\bar{r}, t)$  we obtain:

$$p_s(\bar{r}, t) = \int_{-\infty}^{\infty} dt_0 \int_V \left[ \frac{1}{c^2} \frac{\partial^2 p_i(\bar{r}, t)}{\partial t^2} \tilde{\beta}(\bar{r}_0) + \nabla \cdot [\tilde{\rho}(\bar{r}_0) \nabla p_i(\bar{r}_0, t_0)] \right] G(\bar{r}, t | \bar{r}_0, t_0) d^3 \bar{r}_0. \quad (1.20)$$

Thanks to (1.13) and (1.14), eq. (1.20) can be simplified applying the divergence operator and exploiting the divergence theorem

$$p_s(\bar{r}, t) = \int_{-\infty}^{\infty} dt_0 \int_V \left[ \frac{1}{c^2} \frac{\partial^2 p_i(\bar{r}, t)}{\partial t^2} \tilde{\beta}(\bar{r}_0) + [\nabla \tilde{\rho}(\bar{r}_0) \cdot \nabla p_i(\bar{r}_0, t_0)] \right] G(\bar{r}, t | \bar{r}_0, t_0) d^3 \bar{r}_0. \quad (1.21)$$

Eq. (1.21) can be analytically solved for many elemental integration domains, like spheres and cylinders, which can be used in many circumstances for modeling with good approximation some characteristics of real biological tissues [12].

### Diffusion of plane waves

Let's suppose that the incident field is a plane wave

$$p_i(\bar{r}, t) = p_0 e^{i(\bar{k}_i \cdot \bar{r} - \omega t)}.$$

Substituting the incident field in the eq. (1.21) we get

$$p_s(\bar{r}, t) = p_0 e^{-j\omega t} \int_{V_0} \left[ k_i^2 \tilde{\beta}(\bar{r}_0) - j \nabla \cdot \tilde{\rho}(\bar{r}_0) \bar{k}_i \right] \left( \frac{e^{j(\bar{k}_i \cdot \bar{r}_0 - k|\bar{r} - \bar{r}_0|)}}{4\pi |\bar{r} - \bar{r}_0|} \right) d^3 \bar{r}_0 \quad (1.22)$$

where  $k = |\bar{k}_i| = \omega/c$ .

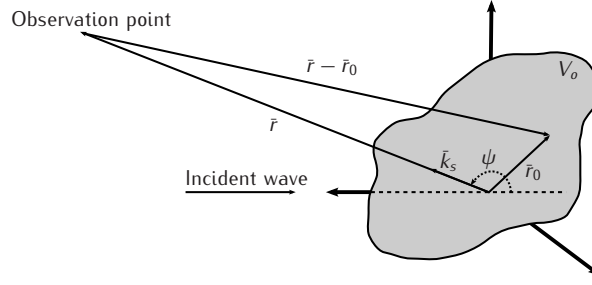


Figure 1.2: Reference system for the calculus of the diffused field with Born approximation.

Expanding the exponent of the exponential term which is depended on distance, considering target points that are far from the origin with respect to size of the region  $V_0$  and considering as reference system the one shown if fig. 1.2, we can write

$$k|\bar{r} - \bar{r}_0| \approx k|\bar{r}| \left( 1 - \frac{\bar{r} \cdot \bar{r}_0}{|\bar{r}|^2} \right) \approx k|\bar{r}| - \bar{k}_s \cdot \bar{r}_0$$

from which follows

$$\bar{k}_i \cdot \bar{r}_0 - k|\bar{r} - \bar{r}_0| = (\bar{k}_i - \bar{k}_s) \cdot \bar{r}_0 - k_r \quad (1.23)$$

where  $k_s$  is the wave vector parallel to  $\bar{r}$ , with magnitude  $k$  and  $k_r = \bar{k}_s \cdot \bar{r}_0$ . Substituting in eq. (1.22) we get

$$p_s(\bar{r}, t) = \frac{p_0 e^{-j(\omega t - k|\bar{r}|)}}{4\pi|\bar{r}|} \int_{V_0} \left[ k^2 \tilde{\beta}(\bar{r}_0) - j\nabla \cdot \tilde{\rho}(\bar{r}_0) \right] e^{j(\bar{k}_i - \bar{k}_s) \cdot \bar{r}_0} d^3 \bar{r}_0. \quad (1.24)$$

The scattered field can be interpreted as a plane wave, generated by a point source located in the origin of the reference system, with an anisotropic angular distribution defined by integral in (1.24). Defining the functions

$$\beta(\bar{k}) = \int_{V_0} \tilde{\beta}(\bar{r}) e^{-j\bar{k} \cdot \bar{r}} d^3 \bar{r} \quad (1.25)$$

$$\eta(\bar{k}) = \int_{V_0} \tilde{\rho}(\bar{r}) e^{-j\bar{k} \cdot \bar{r}} d^3 \bar{r} \quad (1.26)$$

$$\bar{K} = \bar{k}_i - \bar{k}_s \quad (1.27)$$

eq. (1.24) can be rewritten as

$$p_s(\bar{r}, t) = \frac{p_0 e^{-j(\omega t - k|\bar{r}|)}}{4\pi|\bar{r}|} k^2 [\beta(\bar{K}) + \rho(\bar{K}) \cos \psi] \quad (1.28)$$

where

$$\cos \psi = \frac{\bar{k}_i \cdot \bar{k}_s}{|\bar{k}_i|^2}. \quad (1.29)$$

The term  $[\beta(\bar{K}) + \rho(\bar{K}) \cos \psi]$  is called diffusion function and describes completely the diffusion properties of a medium, in the limits of Born's approximation.

Analyzing the expression of the diffusion function some interesting consideration can be deduced. First of all, if the variation of mass density and compressibility are small

and random,  $|\beta(\vec{r})|$  e  $|\rho(\vec{r})|$  will be almost constant for a large set of values of  $k$ , and the magnitude of the diffused field will be proportional to  $k^2$ , like in the so called Rayleigh's diffusion.

The angular variation of the field is rather determined by the spatial variations of mass density and compressibility. For example, if such variations are isotropic, also the diffused field will be isotropic with a radiation pattern of a dipole. Therefore, the diffused field contains many informations about the acoustical properties of the propagation medium. Such information can be deduced by a complete set of measurement for different values of  $\vec{K}$ , or for different  $(k_i, \phi_s, \theta_s)$  in a polar reference system. Such technique is called diffraction tomography.

In many practical situations, since only a limited set of measurement is available, it is not possible to reconstruct the diffusion function. This is the case of the medical imaging systems where the measurement are limited to  $\phi_s = 0$  e  $\psi = \pi$ , and therefore only the quantity  $\tilde{\beta}(\vec{r}) - \tilde{\rho}(\vec{r})$  can be measured. Moreover, in medical imaging system the maximum frequency is limited by the frequency dependent attenuation which reduces the frequency range to 1-40 MHz.

**Field diffused by a sphere.** If the non homogeneous region  $V_1$  is a sphere of radius  $a$ , the diffusion function can be found analytically using a polar reference system  $(s, \vartheta, \phi)$ :

$$\begin{aligned}\tilde{\beta}(\vec{r}_0) &= \begin{cases} \beta_1 & |\vec{r}_0| \leq a \\ 0 & |\vec{r}_0| > a \end{cases} \\ \tilde{\rho}(\vec{r}_0) &= \begin{cases} \rho_1 & |\vec{r}_0| \leq a \\ 0 & |\vec{r}_0| > a \end{cases} \\ f &= \int_0^a \int_0^{2\pi} \int_0^\pi (\beta_1 + \rho_1 \cos \theta) e^{j2\pi(\sin \theta/2 \cos \vartheta)s} s^2 \sin \vartheta \, d\vartheta d\phi ds \\ &= 2\pi \int_0^a s^2 (\beta_1 + \rho_1 \cos \theta) \int_{-1}^1 e^{js\mu x} d\alpha ds \\ &= k^2 \frac{4\pi}{\mu^3} (\sin \mu a - \mu a \cos \mu a) (\beta_1 + \rho_1 \cos \theta) \end{aligned} \quad (1.30)$$

where

$$\begin{aligned}\mu &= 2k_s \sin \theta/2 \\ \alpha &= \cos \vartheta\end{aligned}$$

For  $\mu a \rightarrow 0$  we have

$$f \rightarrow 4\pi(\beta_1 + \rho_1 \cos \theta)k_i^2 V$$

where  $V$  is the volume of the spherical region  $V_1$ . If no variation of mass density are present, the diffused field is isotropic and the diffused power is proportional to  $k_i^4 V^2$ . In fig. 1.3 the radiation patters of a sphere for different values of  $ka$  are shown.

**Field diffused by a set of obstacles.** If the volume  $V$  is constitute by many non homogeneous regions, the diffused field will depend on the characteristics of each region.

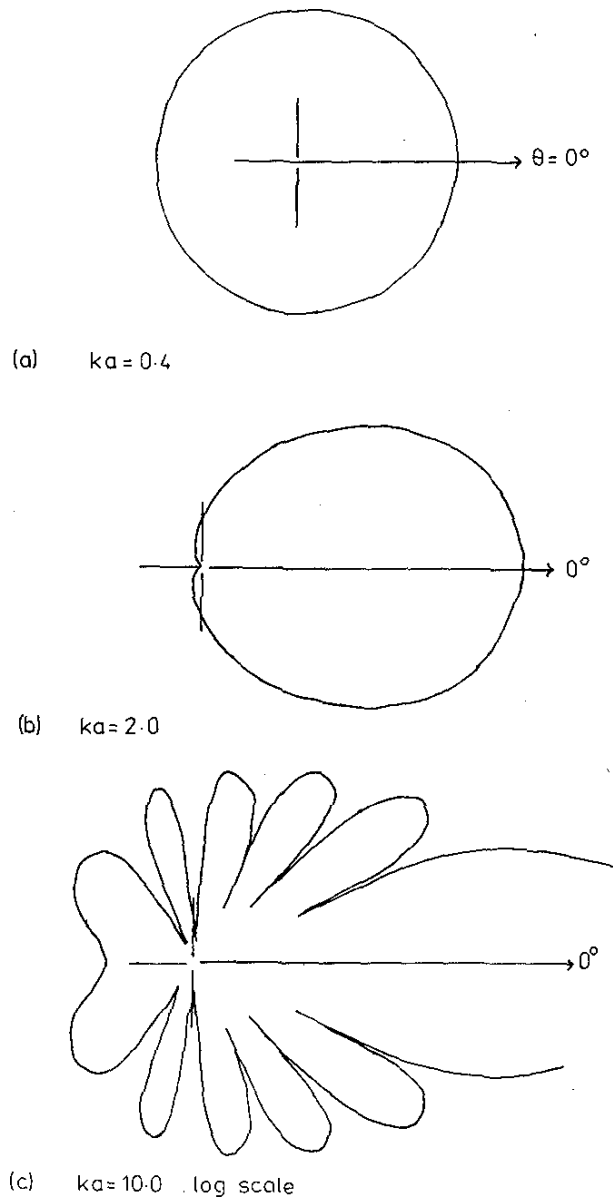


**Figure 1.3:** Radiation patterns of a spherical obstacle for different radius computed with the Born's approximation.

Neglecting the multiple diffusions, the diffusion function of a set of  $N$  identical obstacles can be written as

$$F(\theta, \phi) = f(\theta, \phi) \sum_{i=1}^N e^{i\vec{k} \cdot \vec{r}_i} \quad (1.31)$$

where  $\vec{r}_i$  is the position of the  $i$ -th obstacle and  $f(\theta, \phi)$  is the diffusion function of a single obstacle. This model allows to compute with good approximation the field diffused by tissues that are characterized by an high degree of regularity, evaluating the dependence on the frequency and scatter position and other effects due to the perturbation of structure regularity [12] (cap.6). However, since many biological tissue are characterized by an highly variable (or even random) microstructure, stochastic modelling is mandatory.

**Field diffused by a random medium: discrete model.** Let's consider the non homogeneous region  $V$  as a discrete set of obstacles, randomly positioned in an homogeneous substrate. Each obstacle is assumed to be small if compared to the incident field wavelength. By neglecting the multiple diffusion, the diffused field can be written as the sum of the field diffused by each obstacle.

The diffused field can be decomposed in two components: a coherent component and a non coherent component

$$p = p_c + p_{inc}$$

The coherent component  $p_c$  is given by the statistical average with respect all the possible geometrical configurations of the obstacles. The non coherent component is given by the random fluctuations around the coherent component, due to all the possible geometrical configuration of the obstacles.

The diffused field is therefore a random variable with mean value and variance

$$\langle p \rangle = p_c \quad \langle p^2 \rangle = |\langle p_c \rangle|^2 + \langle |p_{inc}|^2 \rangle.$$

The diffused component  $p_{inc}$  can be written as

$$p_{inc}(\vec{r}, t) = F(\theta, \phi) e^{i(k\vec{r} - \omega t)} \quad (1.32)$$

$$F(\theta, \phi) = \sum_n f_n(\theta, \phi) e^{i\vec{r} \cdot \vec{r}_n} \quad (1.33)$$

where  $\vec{r}_n$  is the position of the  $n$ -th obstacle. Since the obstacles are small if compared to the wavelength, their diffusion functions can be assumed to be the diffusion function of a sphere:

$$f_n(\theta, \phi) = k_i^2 a_n.$$

therefore, the overall diffusion function  $F(\theta, \phi)$  is a random variable with zero mean which statistic will be discussed later on.

The acoustical intensity of the non coherent component is proportional to

$$\langle |F(\theta, \phi)|^2 \rangle = k_i^4 \left[ \sum_{n=1}^N a_n^2 \right]$$

and therefore, in the case of identical obstacles, it is proportional to  $N$  and follow a quadratic law with respect to the frequency of the incident field. Such kind of diffusion is called Rayleigh's diffusion or Rayleigh's scattering.

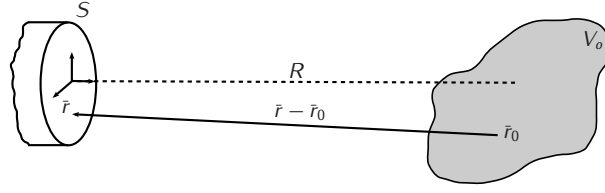


Figure 1.4: Reference system for calculating the signal received by a transducer.

**Field diffused by a random medium: continuous model.** In this model, the obstacle is characterized by continuous variation of mass density and compressibility around a constant mean value, characterized by specific autocorrelation functions. For the sake of simplicity, let's assume that the region  $V$  is non homogeneous only with respect to the compressibility. The non coherent component of the field is therefore

$$p_s(\bar{r}, t) = \frac{e^{-j(\omega t - \bar{r} \cdot \bar{r})}}{4\pi|\bar{r}|} k_i^2 \beta(\bar{k})$$

where in this case  $\beta(\bar{k})$  and  $P_s(\bar{r}, t)$ , are random variables with mean squared value

$$|\langle p_s(\bar{r}) \rangle|^2 = \frac{k_i^4}{16\pi^2|\bar{r}|^2} \langle \beta \rangle \quad (1.34)$$

$$|\langle \beta(\bar{r}) \rangle|^2 = \int_V N_\beta(\bar{r}) e^{j\bar{k} \cdot \bar{r}} d^3\bar{r} \quad (1.35)$$

and where  $N_\beta$  is the autocorrelation function of the compressibility variation.

### Diffusion of band-pass pulses

So far, only monochromatic incident fields have been taken into account. However, in medical imaging systems also band-pass pulses are used. The diffused field for a band-pass incident pulse can be computed with different methods in frequency or time domain. If the expression of the diffused field for a monochromatic incident field is known, the diffused field for a band-pass pulse can be found integrating its expression with the Fourier transform of the incident pulse.

Alternatively, the diffused field can be computed in time domain, integrating the eq. (1.21). In particular we want to calculate the signal received by the transducer after the diffusion of band-pass pulse caused by an obstacle. The received signal, expressed in terms of a voltage  $V(t)$ , can be calculated as

$$V(t) = E_m(t) *_{t'} \int_{S(\bar{r})} p_s(\bar{r}, t) dS(\bar{r}) \quad (1.36)$$

where  $E_m(t)$  is the transducer electromechanical impulse response and  $\bar{r}$  is the vector that indicates the points over the transducer surface  $S(\bar{r})$ , with respect to the reference system, shown in fig. 1.4.

The expression of the diffused field can be written in terms of the differential operator

$$L[.] = \frac{\tilde{\beta}(\bar{r}_0)}{c^2} \frac{\partial^2}{\partial t^2} + \nabla \tilde{\rho}(\bar{r}_0) \cdot \nabla \quad (1.37)$$

in the following way

$$p_s(\bar{r}, t) = \int_{-\infty}^{\infty} dt_0 \int_V L[p_i(\bar{r}_0, t)] \frac{\delta(t - t_0 - |\bar{r}_0 - \bar{r}|/c)}{4\pi|\bar{r} - \bar{r}_0|} d^3\bar{r}_0. \quad (1.38)$$

Substituting in the eq.(1.36) and integrating with respect to  $t_0$  over the transducer surface  $S(\bar{r})$  we get

$$V(t) = E_m(t) *_t \int_V L[p_i(\bar{r}_0, t)] d^3\bar{r}_0 *_t h(\bar{r}, t) \quad (1.39)$$

where

$$h(\bar{r}_0, t) = \int_{-\infty}^{\infty} \int_S \frac{\delta(t - t_0 - |\bar{r}_0 - \bar{r}|/c)}{4\pi|\bar{r} - \bar{r}_0|} dS(\bar{r}) dt_0 \quad (1.40)$$

it is the spatial impulse response over the transducer surface. Introducing the expression of the incident field that, as will be shown later on, is given by

$$\begin{aligned} p_i(\bar{r}_0, t) &= \int_{S(\bar{r})} \frac{A(t - |\bar{r}_0 - \bar{r}|/c)}{4\pi|\bar{r}_0 - \bar{r}|} dS(\bar{r}) \\ &= A(t)h(\bar{r}_0, t), \end{aligned} \quad (1.41)$$

(where  $A(t)$  is the electrical excitation of the transducer) the expression of the received signal is

$$V(t) = E_m(t) *_t \int_V L[A(t)h(\bar{r}_0, t)] d^3\bar{r}_0 *_t h(\bar{r}, t). \quad (1.42)$$

Moving the temporal convolution inside the differential operator we get

$$\begin{aligned} V(t) &= E_m(t) *_t \int_V L[A(t)h(\bar{r}_0, t) *_t h(\bar{r}_0, t)] d^3\bar{r}_0 \\ &= E_m(t) *_t \int_V L[q(\bar{r}_0, t)] d^3\bar{r}_0. \end{aligned} \quad (1.43)$$

The function  $q(\bar{r}_0, t) = A(t)h(\bar{r}_0, t) *_t h(\bar{r}_0, t)$  pulse-echo spatial impulse response, and it represents the signal diffused by a point scatter located in  $\bar{r}_0$ , and subject to the incident field generated by  $A(t)$ . This function, which is only dependent by the transducer geometry, allows characterizing the distribution of the field generated by a transducer and therefore, its resolution. Such function is often called also *point-spread function* (PSF).

The received signal can be calculated integrating above the region  $V$  the function  $L[q(\bar{r}_0, t)]$ :

$$V(t) = E_m(t) *_t \int_V \left[ \frac{\tilde{\beta}(\bar{r}_0)}{c^2} \frac{\partial^2 q(\bar{r}_0, t)}{\partial t^2} + \nabla \tilde{\rho}(\bar{r}_0) \cdot \nabla q(\bar{r}_0, t) \right] d^3\bar{r}_0.$$

Manipulating again the expression of the received signal, it can be expressed as the convolution between the transducer electromechanical impulse response  $E(t)$ , the system point-spread function  $q(\bar{r}_0, t)$  and the propagation medium impulse response  $T(\bar{r}_0)$

$$V(t) = E_m(t) *_t T(\bar{r}_0) *_t q(t, \bar{r}_0). \quad (1.44)$$

where

$$T(\bar{r}) = \left[ \tilde{\beta}(\bar{r}_0) + \tilde{\rho}(\bar{r}_0) \right] \nabla^2. \quad (1.45)$$

This formulation of the received signal is called convolution model and allows separating the effects due to imaging system by the effects due to the propagation medium. Such model will be used in this work as reference model for developing a deconvolution model.

MATERIAL	f = 1 MHz	f = 5 MHz
Water	1360	54
Air	0.25	0.01
Brain	3.5	1
Liver	3	0.5
Fat	5	1
Muscle	1.5	0.3
Oil	3	0.12
Bone	0.2	0.04
Perspex	1.5	0.3
Polyethylene	0.6	0.12
Kidney	3	0.5
Blood	17	3
Vitreous humor	-	6

Table 1.3: Penetration depth at -3 dB for common materials and tissues.

### Absorption and attenuation

So far, only lossless medium were considered. Real materials as well as biological tissues are characterized by absorption phenomena due to the conversion of mechanical energy into heat. Such conversion is due to different physical mechanism like:

- viscosity, caused internal friction in the materials;
- thermal diffusion and mass diffusion, i.e. molecular movements respectively due to temperature and concentration gradients, that perturb waves motion;
- molecular inertia.

Absorption can be modeled as an exponential reduction of acoustic wave amplitude as function of the distance

$$A_s(\vec{r}) = A_0 e^{-\alpha|\vec{r}|} \quad (1.46)$$

where  $\alpha$  is called absorption coefficient, while  $A_0$  is the wave amplitude. it can be shown that the absorption coefficient is dependent by the frequency of the incident field according to the relation

$$\alpha = c \cdot f^\beta \quad (1.47)$$

where  $c$  is the propagation speed,  $f$  is the frequency of incident field and  $\beta$  is characteristic parameter of the propagation medium.

Moreover, like reviewed in sec. 1.1, the material non homogeneities cause reflection and refraction phenomenas, that causes a reduction of the acoustic field during its propagation. The overall effect of reflection, diffusion and absorption causes an attenuation that can be modeled as an exponential law:

$$A(\vec{r}) = A_0 e^{-a|\vec{r}|} \quad a = \alpha + \alpha_s \quad (1.48)$$

where  $\alpha_s$  is the attenuation coefficients due to field diffusion.

Such attenuation can be also expressed in term of acoustical intensity:

$$I(\vec{r}) = I_0 e^{-\mu|\vec{r}|}$$

where  $\mu$  is the intensity attenuation coefficient, related to the attenuation coefficient by the relation

$$\mu = 2a$$

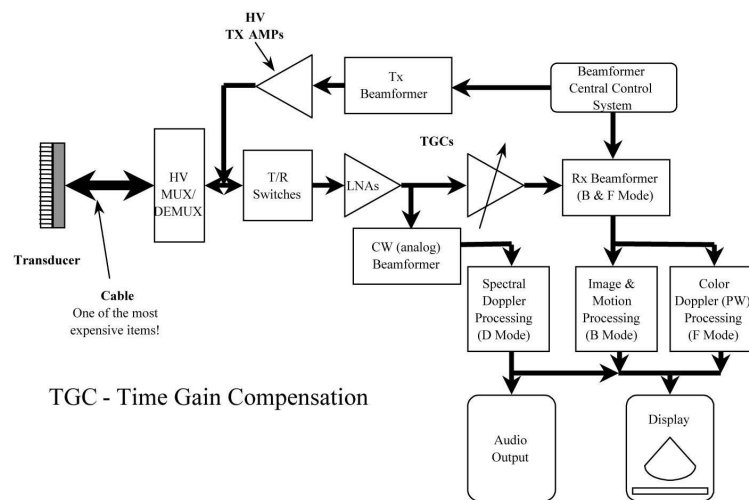


Figure 1.5: Functional block diagram of a generic digital ultrasound imaging system

Typically the attenuation of materials is expressed in dB by the expression

$$A(\text{dB}) = \mu \cdot f \cdot |\bar{r}|$$

where  $\mu$  is the attenuation coefficient expressed in  $\frac{\text{dB}}{\text{cmMHz}}$ . Another common way for expressing material attenuation is the penetration depth for different frequencies, which indicates the depth at which the acoustic intensity is attenuated of 3 dB. In tab. 1.3, values of penetration depth for different material and biological tissues are reported.

(intro)

## 1.2 Ultrasound imaging systems architecture

A functional block diagram of a generic digital ultrasound imaging system is shown in fig. 1.5. This block diagram is composed of two different sections: the transmit section, which drives the ultrasound transducer to generate the ultrasound beam, and the receive section, which performs all the processing related to signal acquisition like, amplification and pre-conditioning, analog to digital conversion, scan conversion and display. Transmit and receive sections are then synchronized by a timing system (T/R switch), which guarantees an exclusive access to the system probe.

### 1.2.1 Transmit section

This section is composed of all the components necessary for generating the tension pulses used for exciting the piezoelectric elements that compose the probe and generate the ultrasonic beam. Operating frequencies for medical ultrasound are in the 1-40 MHz range, with external imaging machines typically using frequency of 1-15 MHz, while intravenous cardiovascular machines use frequencies up to 40 MHz. The main limitation in using high frequency pulses is the frequency dependent attenuation of biological tissues, which increases with the frequency and at 10 MHz is already 1 dB/Cm/MHz. Such big attenuation, together with the transmission power limit poses a compromise between the maximum imaging depth and the maximum frequency of the ultrasound field.

Older and simpler imaging systems are equipped only with a mono-element probe. The transmit section is composed of a pulse generator and an high voltage amplifier necessary for pulse amplification. Very high voltages are in fact required for driving the piezoelectric transducers that generate the ultrasonic field. The focusing of the ultrasound beam is usually made with a focused transducer, while the image scan is done mechanically moving the probe.

Modern and more complex imaging systems are equipped with multi-element phased array probes, which allow to implement focusing and image scan electronically. Either one focus at fixed depth or multiple focus at different depth can be used. All that is made by the beamforming stage, which drives all the probe elements with a pattern of delayed pulses in order to focus the ultrasound beam and move it in the desired position, reducing the secondary lobes of the radiation pattern. Typically, when probes with a high number of elements are employed, in order to reduce the complexity of the transmit system, an high-voltage multiplexer is used for selecting and driving groups of elements with pulses that are generated serially by the pulse generator.

### 1.2.2 Receive section

This section is more complex than the transmit one, both from a circuitual and functional point of view. Here, all the processing necessary for signal acquisition, memorization and display are done. In fig. 1.5 all the blocks composing the receiving stage are shown.

**Low noise pre-amplifier.** This is the first block immediately after the ultrasound transducer and it serves to amplify the received signal which amplitude is just some  $\mu\text{V}$ , due to the high attenuation encountered during the propagation. To have an idea of the order of magnitude of the overall acoustical attenuation it should be noted that the attenuation experienced by a sinusoidal wave with frequency of 3 MHz, reflected by a structure at 15 cm of depth can vary from 60 up to 80 dB. A low noise figure and high dynamical range is therefore mandatory in this stage.

**Time gain compensation amplifier.** During the propagation through the tissues, the ultrasound field is affected by depth dependent attenuation. Therefore, structures that have the same reflectivity but are located at different depth will have a different intensity. In order to have a uniform representation of tissue reflectivity a time dependent amplification, usually called time gain compensation (TGC), is required. To adapt this amplification to the different operating conditions, the manufacturers provide on the system control interface different variable controls to adjust amplifier gain at the different depth or modify the parameters of the gain curve.

Time gain compensation is also necessary to reduce the signal dynamic before the analog to digital conversion. Due to large tissue attenuation, ultrasonic echo RF signal is characterized by a very large desired dynamic range (qualitatively about 160 dB), which can hardly be obtained by an ADC at the conventional sampling rate that in commercial equipment ranges from 33 MHz to 50 MHz [10]. For these reasons, preliminary fixed time gain compensation is usually applied to the RF signal before its conversion, in order to partially compensate the tissue attenuation and reduce the required dynamic range to about 100 dB. Then, usually up to 1024 levels (12 bits) are employed for signal quantization.

**A/D converter.** This stage converts the radio frequency signal from analog to digital. The sampling can be done before or after the beamforming stage according to the type of beamforming system (analog or digital). In system equipped with analog beamforming, the A/D conversion is done after the beamforming block in the receive stage and it's missing in the transmit stage. In system equipped with digital beamforming, the conversion is done after the TGC block in the receive stage and before the beamforming stage in the transmit stage. The resolution and sampling frequency of the converter depend on the characteristics of the imaging system and on its position in the imaging system scheme.

**Focusing and beamforming stage.** In all the system equipped with multi-element probes, as in the transmit chain, there is a beamforming block that provide for focusing and image scan in reception. Transmit and receive beamforming blocks are usually synchronized by the beamforming control system. Like in transmission, one fixed focus or multiple focus located at different depth can be used in the receive stage. Of course, multiple focus in transmission and in reception provide a better focusing and therefore image of higher quality. However, the higher is the number of focus, the more complex and slower will be the beamforming. Together with the probe, beamforming stage is the most critical part of imaging system and it strongly determines system resolution. For further details about beamforming and system resolution see [29].

**Demodulation stage.** After the amplification, the received signal is ready to be analyzed for extracting the desired information and processed to be displayed. The information necessary to generate the B mode image is contained in the signal envelope. The envelope amplitude is in fact related to the tissue reflectivity. Therefore, in most of the equipment, the focusing stage is followed by a envelope detection stage and only the B mode image is available to the user. Recently, some manufactures gave access to the radio frequency signal before the envelope detection in their equipment. As claimed by many authors, this approach is fundamental for tissue characterization purposes [26][25], since many information concerning the tissues microstructure is contained in the radio frequency signal.

**Preprocessing stage.** With pre-processing are meant all the processing performed on the B mode image before its display on the screen, with the purpose of increasing the image intelligibility. Such processing are usually guided by the user through different controls that are available on the system interface. An example of pre-processing is gamma correction, which consist in re-mapping through a nonlinear function the signal dynamic on the gray-level scale.

### 1.2.3 Probes

The main distinction in ultrasound probes is between mono-element and multi-element transducers. Historically developed as first type of probe, mono-element transducers are now more diffused in industrial applications for nondestructive material inspection, since they require simpler control hardware and can easily handle high operating powers. The main drawback of mono-element transducer is the need of mechanical focusing.

Thanks to electronic focusing, multi-element probes are preferred in medical imaging applications. Driven by many clinical needs, transducers for medical imaging appear in a wide variety of forms and sizes according to diagnostic field, as shown in fig. 1.6. Multi-



**Figure 1.6:** Examples of medical ultrasound probes. From left to right: convex cardiac probe, rectal probe, high frequency linear array, transvaginal probe and convex array probe. (Picture taken from <http://www.newtech-medical.com>)

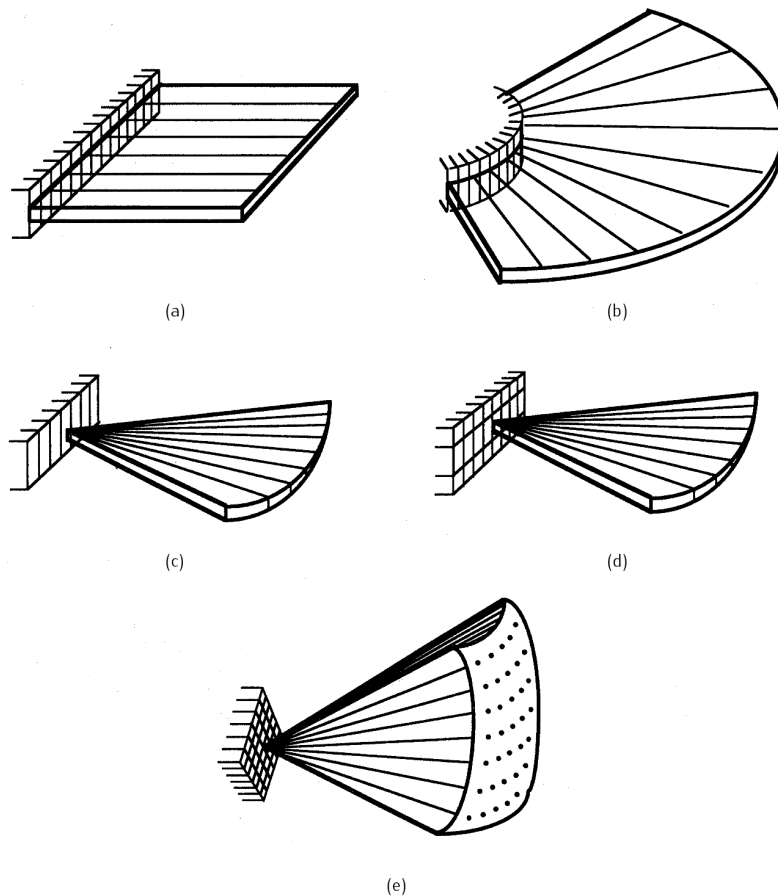


**Figure 1.7:** Configuration of multi-element probes and possible region scanned by the acoustic beam: sequential linear array (a), curvilinear array (b), linear phased array (c), 1.5D array (d) and 2D array (e).

element probes can be further classified according to their geometry: linear sequential, curvilinear, 1D, 1.5D or 2D, as schematized in fig 1.7.

Linear Sequential Arrays can have up to 512 elements in current commercial equipment. A subset of the available elements is selected to image lines that are directed perpendicular to the face of the transducer, as shown in fig. 1.7(a); the acoustic beam is therefore focused but not steered. The advantage of this scheme is that the array elements have high sensitivity when the beam is directed straight ahead. The disadvantage is that the field of view is limited to the rectangular region directly in front of the transducer. Linear-array transducers must have a large footprint to obtain an adequate field of view.

Curvilinear or convex arrays have a different shape than sequential linear arrays, but they operate in the same manner. In both cases, the scan lines are directed perpendicular to the transducer face, but because of its convex shape, scans a wider field of view, as shown in fig. 1.7(b).

The more advanced linear phased arrays have 128 elements. All the elements are used to transmit and receive each line of data. As shown in fig. 1.7(c), by driving all the element with a phased pulses pattern, the scanner steers the ultrasound beam through a sector-shaped region in the azimuth plane. With this technique it is possible to scan a region that is significantly wider than the footprint of the transducer, making them suitable for scanning through restricted acoustic windows. As a result, these transducers are ideal for cardiac imaging, where the transducer must scan through a small window to avoid the obstructions of the ribs (bone) and lungs (air). However the image obtained as a depth dependent axial resolution.

The so-called 1.5D array is similar to a 2D array in construction but operates as a 1D array. The 1.5D array contains elements along both the azimuth and elevation dimensions. Features such dynamic focusing and phase correction can be implemented in both dimensions to improve image quality. Since a 1.5D array contains a limited number of elements in elevation (e.g., 3 to 9 elements), steering is not possible in that direction. Fig. 1.7(d) illustrates a B-scan made with a 1.5D phased array. Linear sequential scanning is also possible with 1.5D arrays.

A 2D phased-array has a large number of elements in both the azimuth and elevation dimensions. Therefore, 2D arrays can focus and steer the acoustic beam in both dimensions. Using parallel receive processing, a 2D array can scan a pyramidal region in real time to produce a volumetric image, as shown in fig. 1.7(e).

In medical imaging conventional linear, curved and phased array have typical azimuth apertures that vary in length from 25 to 60 mm and elevation apertures that are 2-16 mm. The number of elements in 1D dimensional array varies from 32 to 400 and typical frequency range from 1 MHz (for harmonic imaging) to 15 MHz (for high resolution imaging of superficial structures). Finally, the fractional bandwidth range from 30-100 % [29].

#### 1.2.4 Imaging modes

**A-Mode.** Amplitude Mode is the first and the simplest ultrasound imaging mode. It consist in a one dimensional track in which the amplitude of the returned echo along a single line is displayed.

**M-Mode.** Motion Mode is the first imaging mode to display movements. It is realized displaying different A- Mode scanline acquired in different moments and it allows the

DEPTH (cm)	SCANLINES			
	25	50	100	200
5	616	308	154	77
10	308	154	77	38
15	205	103	51	26
20	154	77	38	19
25	123	61	30	15
30	103	51	25	12

**Table 1.4:** Maximum achievable frame per seconds for a give number of scanlines and imaging depth.

monitoring of position, impedance and speed of the moving interfaces.

**B-Mode.** The brightness modulated mode is the 2D extension of the A-mode, where the returned echoes are displayed in a 2D image which intensity is proportional to echoes amplitude. Through B-mode imaging it is possible to obtain an anatomical cross section of tissues. This section is obtained by scanning manually or electronically the area of interest with several A-mode in different directions and displaying the different scanlines in an image.

**Real time B-Mode.** With real time B mode it is meant a succession of B mode images that display the tissue in different time instant. In order to have real time imaging of a tissue, the scansion must be performed electronically. Although fast, due to the fine propagation speed of the ultrasonic filed, the time required for scanning and area is not negligible and it strongly dependent on several factors like the imaging equipment and the area to be imaged. If we neglect the delay due to the electronic circuits, the maximum number of B mode images per second that can be acquired is called frame rate, and is given by

$$FR = \frac{c}{2DN} \quad (1.49)$$

where  $D$  and  $N$  are respectively the maximum scanning depth and the number of scanlines, while  $c$  is the speed of sound in the tissue. This expression put in evidence the compromise between the achievable frame rate and the area to be imaged. In table 1.4 the maximum frame rate achievable as function of the scansion depth and scan lines number is shown.

### 1.3 Modeling and simulation of ultrasound imaging systems

(review of available models and software for ultrasound simulation: to be written)

### 1.4 Future trends in ultrasound medical imaging

Diagnostic ultrasound is used in almost all medical fields and has already become the preferred imaging modality in a variety of clinical situations. For example, as reviewed in chap.2, ultrasound imaging plays a keyrole in diagnostic procedure for prostate cancer assessment, management and therapy. The reasons of its success in many clinical context are basically three: ultrasound imaging systems are in general less invasive, faster and chapter than the other imaging techniques. Ultrasound imaging is therefore particularly

well suited to offer noninvasive and economic solution to mass screening, allowing earlier detection of pathologies and effective treatment of presymptomatic disease.

Unfortunately, the quality of the images obtained with ultrasound imaging systems is always poor if compared to the quality provided by other techniques. However, in the last decades ultrasound image quality has improved significantly. This improvement is due to several engineering and technological innovations and breakthroughs like the introduction of a new generation of enhanced bandwidths transducers or scanheads, the introduction of digital imaging systems, and the advent of contrast agents [17].

Within this framework, signal processing techniques play a important role for enhancing image quality, for the development of new imaging technique and methods for computer aided detection of pathologies. In this work, among the possible future applications we will focus on:

- image quality enhancement through signal deconvolution (chapter 4);
- automatic image segmentation (chapter 5);
- computer aided diagnosis of pathologies (chapter 5).



## Chapter 2

---

# Ultrasound Aided Diagnosis of Prostate Cancer

---

Prostate carcinoma is the most frequent diagnosed visceral cancer and the second most common cause of cancer death. As a significant cause of morbidity and mortality, prostate cancer is now a major health care problem. The development of computer aided procedure for prostate cancer diagnosis is therefore an important and challenging field of research. The development of tools that can assist radiologist to accurately identify suspicious regions require a deep knowledge about anatomy, biology and medical procedures involved. In this chapter, some fundamental information about prostate anatomy, pathologies and clinical procedures for cancer diagnosis are reviewed.

**Author contributes.** An original overview of the current procedure and future trend for prostate cancer diagnosis from an biomedical engineering point of view is given.

### 2.1 Prostate anatomy and pathologies

The prostate is a compound tubuloalveolar exocrine gland of the male mammalian reproductive system and it differs considerably among species anatomically, chemically, and physiologically [33]. The main function of the prostate is to store and secrete a clear, slightly alkaline (pH 7.29) fluid that constitutes 10-30 % of the volume of the seminal fluid that, along with spermatozoa, constitutes semen. The rest of the seminal fluid is produced by the two seminal vesicles [33].

A healthy adult human prostate is a chestnut shaped gland enveloped in a fibrous capsule. Its base is attached below the urinary bladder neck, and the apex is fixed to the urogenital diaphragm urinary (see fig. 2.1). It borders on the posterior side with the *rectum* and on the anterior side with the fibromuscular stroma connected to the pubis through the puboprostatic ligaments. On the superior posterior side it is attached to the *seminal vesicles*, a pair of simple tubular glands that secrete a significant proportion of the fluid that ultimately becomes semen [32]. The excretory ducts of seminal vesicles open into the vas deferens, as they enter the prostate gland, and they are lined with the epithelium of the transition zone. Within the prostate, the urethra coming from the bladder is called the prostatic urethra and

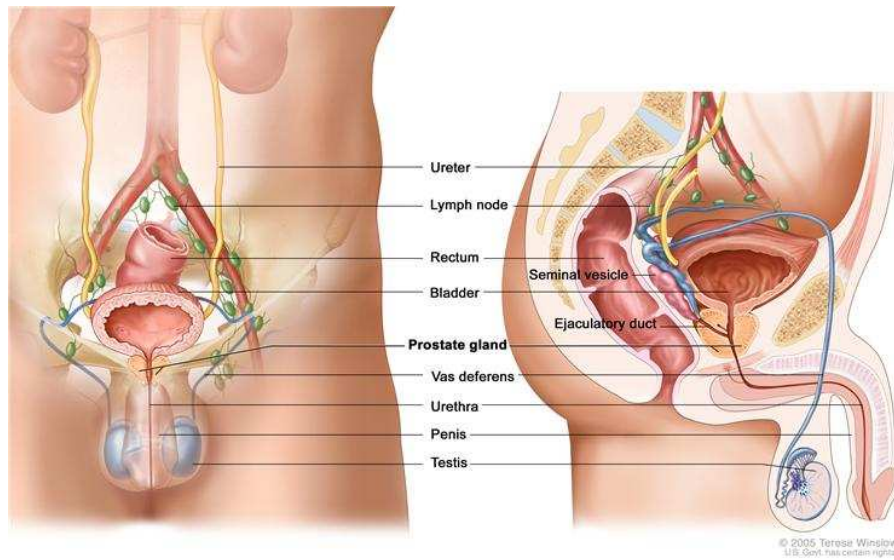


Figure 2.1: Prostate location and anatomy. (picture taken from <http://www.cancer.gov/>)

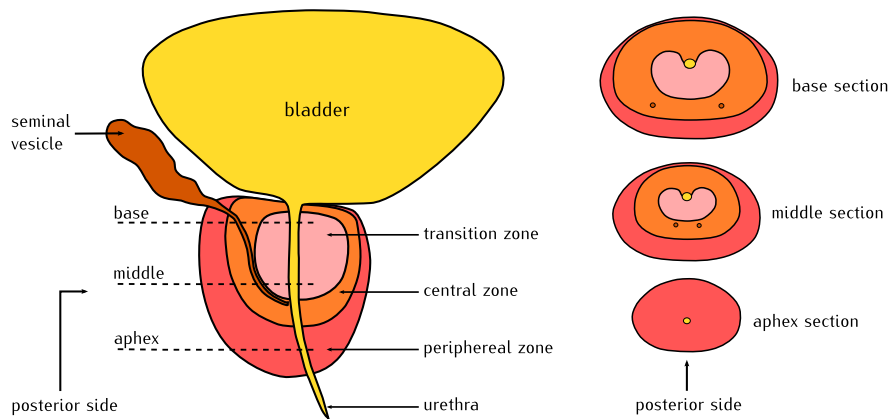


Figure 2.2: Schematic illustration of prostate sagittal (left) and axial (right) sections.

merges with the two ejaculatory ducts. (The male urethra has two functions: to carry urine from the bladder during urination and to carry semen during ejaculation.) The prostate is finally sheathed in the muscles of the pelvic floor, which contract during the ejaculatory process.

According to the classic work of McNeal [19] the prostate gland is divided in three different zones: the transition zone, the central zone, and the peripheral zone (see fig. 2.2). The transition zone surrounds the urethra and extends from the ejaculatory ducts proximally. The peripheral zone encompasses the peripheral zone from the base to the apex. The central zone is composed of tissue immediately surrounding the ejaculatory ducts and it expands inferiorly. The significance of this architecture is based upon the relationship of these three zones to prostatic disease [2]. In the young male the peripheral zone comprises 75% of prostate volume, the transition zone 20% and the central zone 5%. But with the age

this ratios change and after 40 years, since benign hyperplasia is almost inevitable, the transition zone may enlarge and occupy most of the gland.

Before describing the different prostate pathologies, their locations and incidences, we will briefly discuss some medical terminology. With *tumor* and *cancer* are meant a class of swellings or lesions formed by an abnormal growth of cells (termed *neoplastic*) [1][34][30]. *Tumor* is not synonymous with cancer since a tumor can be benign, pre-malignant or malignant, whereas cancer is by definition malignant. Benign lesions do not grow in an unlimited, aggressive manner, does not invade surrounding tissues, and does not metastasize. On the contrary, *cancer* cells display uncontrolled growth (division beyond the normal limits), invasion (intrusion on and destruction of adjacent tissues), and sometimes metastasis (spread to other locations in the body via lymph or blood). According to the tissue involved, several main types of cancer can be distinguished:

- *carcinoma* is cancer that begins in the skin or in tissues that line or cover internal organs;
- *adenocarcinoma* is carcinoma that originates in glandular tissues, as the prostate;
- *sarcoma* is cancer that begins in bone, cartilage, fat, muscle, blood vessels, or other connective or supportive tissue;
- *leukemia* is cancer that starts in blood-forming tissue such as the bone marrow, and causes large numbers of abnormal blood cells to be produced and enter the blood;
- *lymphoma* and *multiple myeloma* are cancers that begin in the cells of the immune system;
- central nervous system cancers are cancers that begin in the tissues of the brain and spinal cord.

Prostate diseases can be distinguished in three main categories [33]: *Prostatitis*, *benign hyperplasia* and *Prostate cancer*.

Prostatitis, is an inflammation of prostate gland. It's a benign pathology and in the acute case is mainly treated with antibiotics [31].

Benign hyperplasia (BPH) consists in prostate enlargement. Due to prostate volume growth, the urination becomes difficult and the main symptoms of BPH include needing to go to the toilet often and/or taking a while to get started. It is fairly common among aging men and it occurs mainly in the transition zone. BPH can be treated with medication, a minimally invasive procedure or, in extreme cases, surgery that removes the prostate.

Prostate cancer, often referred as prostate carcinoma (or adenocarcinoma), is a malignant pathology, and as all the cancers is characterized by an abnormal and uncontrolled cells mutation and replication. As BPH, prostate cancer might cause pain, difficulty in urinating, problems during sexual intercourse, erectile dysfunction and other symptoms. If not detected early and in more aggressive forms, the disease can advance to stages characterized by local invasion of the surrounding tissues (seminal vesicles, bones, rectum), usually resulting in lethality (see fig. 2.12).

The heterogeneous and multifocal nature of prostate cancer lesions poses significant difficulties in their detection. With regard to heterogeneity, prostate cancer tissue typically reveals a juxtaposition on benign cells, preneoplastic lesions and neoplastic lesions of varying severity [2]. With regard to multifocality, individual cancer lesions in a given section of

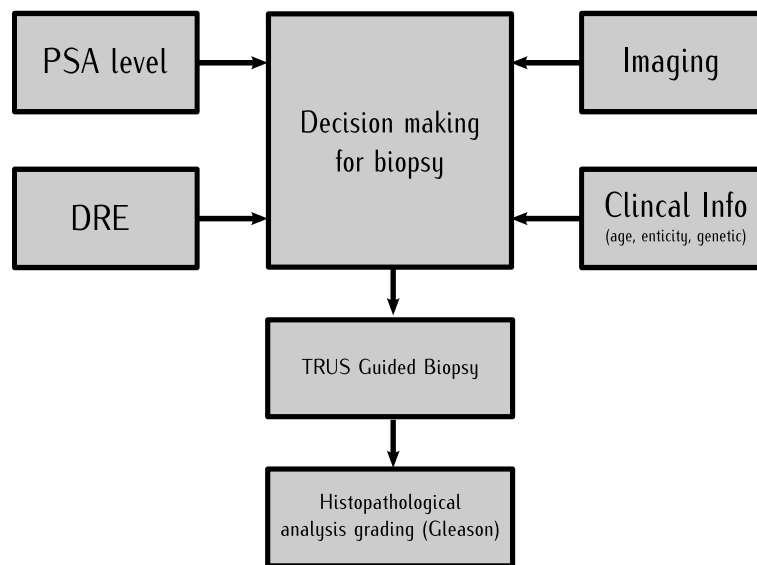


**Figure 2.3:** Schematic representation of clinical procedures steps for detection and grading of prostate cancer.

prostate cancer tissue have been described as genetically distinct. This observation suggests that multiple cancer lesion may emerge and evolve independently, posing significant difficulties in their detection. Concerning prostate cancer emerging locations, typically 70% of prostate carcinoma arise in peripheral zone, 25% in the transition zone and 5% in the central zone [16].

## 2.2 Prostate cancer diagnosis procedure

Prostate cancer is now the second most frequently diagnosed cancer in men, with about 782.600 news cases occurred during the 2007 [6]. Incidence rates of prostate cancer vary significantly worldwide, with the highest recorded rate in United States. With about 254.000 deaths in 2007, prostate cancer is the sixth worldwide leading cause of cancer death in men [6].

The only well established risks factors for prostate cancer are older age, ethnicity (black highest, white average, asian lowest), diet, environment, and family history of disease [6]. Autopsy data from American males revealed that for 50-year-old male the lifetime risk of developing prostate cancer is nearly 42%, although the lifetime risk of having clinically-detected cancer is 17.2% [14]. These statistics highlight how this disease has an high prevalence but a variable aggressiveness. In other words, most men die with, rather than because of their prostate cancer. Therefore, early detection, as well as accurate knowledge of the biological potential of each case is fundamental for cancer management.

A schematic representation of the different steps of current clinical screening protocols for prostate cancer diagnosis is shown in fig. 2.3. All the protocols are based on standard clinical tests like digital rectal examination, prostate specific antigen level measurement and prostate imaging, whose results are used in decision for making and/or repeating biopsy. Hystopatological analysis is in fact the standard and most reliable test for cancer diagnosis and for cancer aggressiveness assessment.

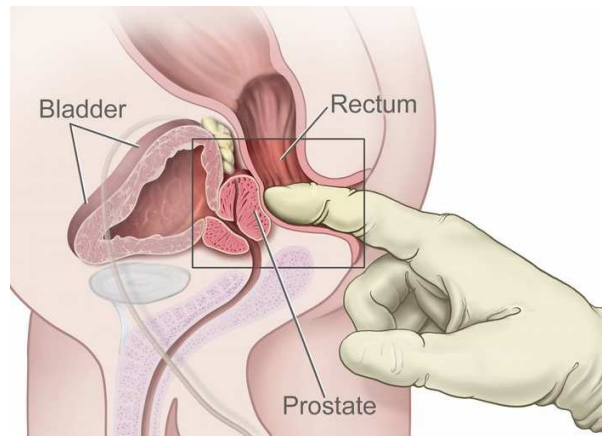


**Figure 2.4:** Digital rectal examination of prostate. (picture taken from <http://cancerinfo.tri-kobe.org/>)

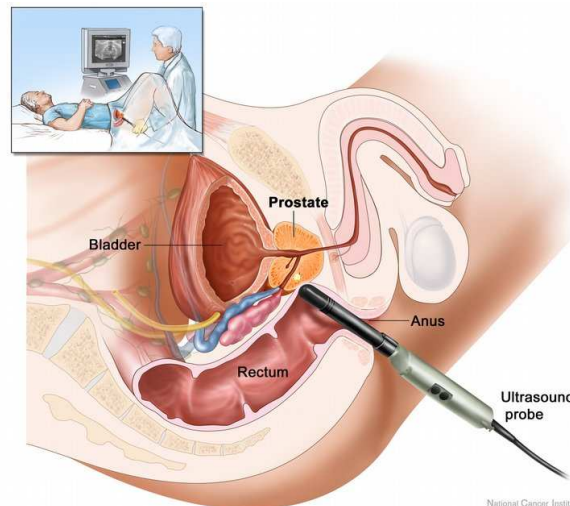


**Figure 2.5:** Transrectal ultrasound imaging of prostate. (picture taken from <http://cancerinfo.tri-kobe.org/>)

### 2.2.1 Digital rectal examination

Digital rectal examination (DRE) is an internal examination of the rectum consisting in palpation of the organs adjacent to the rectum wall (see fig. 2.4). This noninvasive and non-expensive examination is commonly used in prostate cancer screening to check for growths in or enlargement of the prostate gland and a tumour in the prostate, can often be felt as a hard lump. Unfortunately, since only the back wall of the prostate gland is accessible to a doctor, only abnormalities located in the middle or front part of the gland can be detected with this exam. Moreover, only superficial and relatively large lesions can be detected. Therefore, this test is always used in combination with the prostate specific antigen (PSA) test.

### 2.2.2 Prostatic specific antigen

This test measures the amount of PSA in the blood, a *glycoprotein* produced almost exclusively in the epithelium of the prostate gland. While usually abundant in the seminal fluid, PSA is normally found in low concentration in *blood serum*. Two forms of PSA exist in the serum: a protein-bound form and a free or unbound form. PSA produced by normal tissues, is less likely to be bound to proteins whereas the PSA produced by cancer binds to proteins in a higher percentage. Thus, when free PSA is  $> 30\%$  the likelihood of cancer is low, whereas when it is  $<25\%$  the likelihood of cancer increases.

The normal value for total PSA level is controversial but it is generally quoted as  $<4$  ng/mL and adjusted with different criteria according to the screening protocols. However, almost 27% of biopsy-proven prostate cancers present with a normal PSA, and 70–80% of patients with elevated PSA levels do not have prostate carcinoma [16]. This lack of specificity is due to the fact that the amount of PSA increases also with aging, and in presence of prostatitis and benign hyperplasia. PSA velocity, the PSA variation per year, can be useful for differentiating prostate cancer forms: values  $> 0.75$  ng/ml/year is not only a suggestive cancer but also may be related to tumour aggressiveness.

Patients with abnormal DRE and elevated PSA values should be further evaluated for presence of prostate cancer via imaging of the prostate.

### 2.2.3 Prostate imaging

Several types of imaging test can be used for prostate cancer diagnosis and management: transrectal ultrasound (TRUS), computer axial tomography (CAT) and magnetic resonance imaging (MRI) are among the most common. For a complete review about prostate imaging techniques see [23, 16].

**Transrectal ultrasound.** TRUS allows the radiologist to closely examine the prostate gland by inserting a transrectal ultrasound probe into the rectum and illuminating with the ultrasound beam the gland from the posterior side (see fig. 2.2 and 2.5). Currently, the most widely used probe is a 7 MHz transducer with an endorectal probe, which allow the radiologist to obtain imaging of prostate axial or sagittal sections (see fig. 2.6 and 2.7 ). Scanning usually begins in the axial plane at the base of the prostate. Seminal vesicles are visualized first, identified bilaterally as dark anechoic cystic structures. Then prostate gland is imaged starting from the base down to the apex.

The different anatomical zones of the gland appear in different ways [5] [28]. The anatomical distinction between peripheral and central zones is in fact generally not visible by ultrasound, since in a normal man, these two zones are seen as an homogeneous isoechoic area in the posterior section of the prostate. Their normal echo pattern is used as reference for defining the other structures as hyperechoic or hypoechoic. According to this criteria, the prostate capsule appears as an hyperechoic structure that can be identified all around the gland. Several hypoechoic rounded structures can be identified around the prostate gland; these are venous of the prostatic vascular system. The transition zone is the central part of the gland and in a normal young man comprises only a small percentage of the whole gland and thus is difficult to image. In older men with BPH, the transition zone expand compressing its surrounding fibromuscular tissue becoming visible as moderately hypoechoic compared to the central and peripheral zones and it is often filled with cystic spaces.

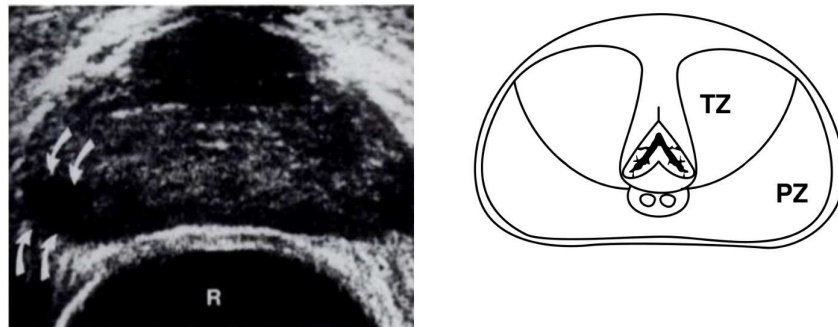


**Figure 2.6:** Schematic representation of prostate axial section (right) and correspondent angular array TRUS image (pictures taken from [5] and [24] respectively). Bottom of the picture corresponds to posterior side.

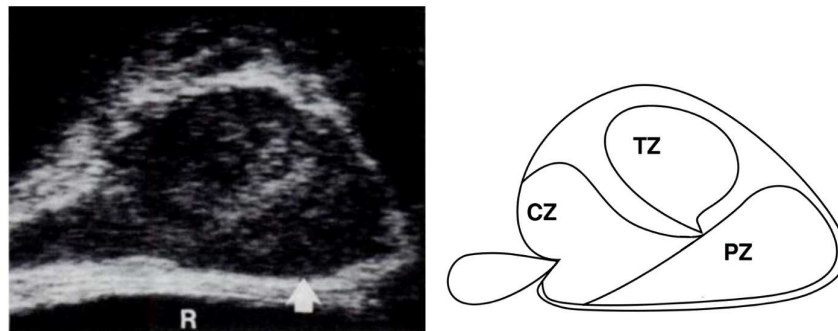


**Figure 2.7:** Schematic representation of prostate sagittal section (right) and correspondent linear-array TRUS image (pictures taken from [5] and [24] respectively). Bottom of the picture corresponds to posterior side.

TRUS is currently the most used imaging technique because it is relatively inexpensive, non-invasive and, mainly, because allows real-time imaging and it is therefore suitable for guiding biopsy protocols. Unfortunately, the diagnostic ability of grey scale TRUS is limited by the intrinsically poor visibility of most of prostate cancers [22]. The parameters that govern the sonographic appearance of prostate cancer are still uncertain and the described appearance of common cancers range from hyperechoic to hypoechoic lesions. For examples, it has been suggested that *fibrosis* often appears as an increased echogenicity lesion [24] and edema and neo-vascularity explain hypoechoic tumors. While hyperechoic cancers are rare, and hypoechoic cancers more common, especially at advanced stages, at early stages most of the contemporary tumors appears either isoechoic or distinguished by a non-specific echo irregularity [22]. TRUS is also rarely useful in detecting extra capsular extension (ECE), i.e. spreading of the tumor outside prostate gland. However, TRUS enables an accurate measurement of prostate size, which is an useful information in determining the PSA density (PSA level/prostate volume). Therefore, TRUS is mainly used to guide prostate biopsys

and not for cancer staging.

Finally, some authors reported that the employment of TRUS doppler improves the accuracy of gray-scale imaging by around 8-10% and its use seems to be promising [22].

**Computer axial tomography.** It is an X-ray based imaging procedure which can be used for obtaining cross-sectional images of prostate gland. Although this technique is widely used in diagnosing many tumours, due to its lack of contrast resolution it is insufficient to distinguish the prostate from its surrounding structures. Therefore its use is limited to verify if known tumours are spreading to the surrounding organs.

**Magnetic resonance.** It uses radio waves and strong magnetic fields for creating very clear cross-sectional images and views from different angles of prostate gland with better soft tissue resolution than any other imaging modality [23]. However a comparison between MRI and TRUS demonstrated that the MRI is more sensitive but less specific than TRUS and in general it doesn't effectively change the level of accuracy of the diagnosis process [18, 20]. The advantage provided by MRI imaging is the possibility of monitoring with better resolution and definition also the extension of the tumour to the surrounding organs with the same scan.

## 2.2.4 TRUS guided biopsy protocols

Historically, the prostate was evaluated for cancer by simple digital rectal examination, and biopsy to obtain a tissue diagnosis was performed blindly. The advent of ultrasound imaging technology offered a new way to evaluate the prostate, and biopsy protocols were soon developed to incorporate ultrasound guidance. However, uniquely among image-guided biopsies, prostate biopsy is not lesion-directed but rather based on a systematic sampling of those areas where cancer incidence is higher. As the disease is often multi-centric, the different areas throughout the whole gland are sampled. In particular, since most of the cancers arises in the peripheral zone, most of the protocols aim to maximize its sampling.

The motivation behind this, as discussed before, is the weak diagnostic significance of imaging inspection techniques due to the high variability of prostate cancer patterns. In other words, ultrasound imaging is used to guide and monitor the biopsy needles insertions in the different areas of the prostate gland. Since metal, if compared to soft tissues, has a high acoustic impedance, biopsy needles appears as hyperechoic lines in TRUS scans, as shown in fig. 2.9.

The first landmark sampling technique was the sextant protocol reported in 1989 [11]. As originally described, six biopsies were obtained in a parasagittal line drawn halfway between the lateral border and midlines bilaterally, from the base, midgland and apex, as shown in fig. 2.8. Although the sextant biopsy protocol was a major advance, with a 20-25% of positive biopsy rate, with a wider experience it was found also inaccurate, principally because it under-samples the peripheral zone [22].

Modifications of the sextant protocol were introduced from the mid 1990s onwards. For example, in the modified sextant biopsy protocol a better sampling of the peripheral zone around the lateral margins is obtained moving laterally and angling anterolaterally the biopsy trajectories. This improved in some cases the detection rate from 80 to 89 % [22]. However, with time even the modified sextant protocol was found to miss some tumours and many alternatives were explored. Therefore, several extended protocols using more

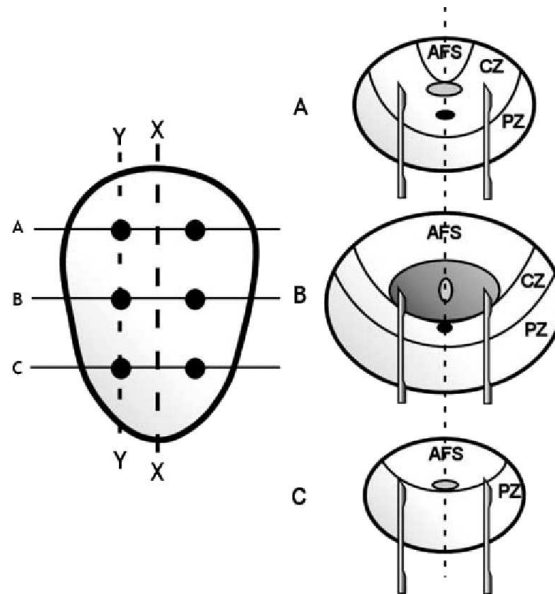


**Figure 2.8:** Diagrammatic representation of sextant biopsy protocol sampling patterns (left) and biopsy needle trajectories in the axial sections of prostate gland (right)

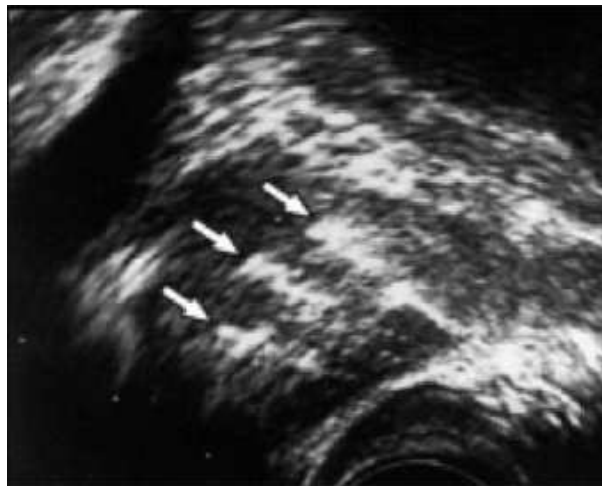


**Figure 2.9:** Example of biopsy needles appearance (pointed by white arrows) in a sagittal section TRUS image during prostate biopsy.

cores (8 or 10) directed to the peripheral zone were introduced. Although the available results show that the extended protocols can improve diagnosis accuracy it is still a matter of debate whether extended protocols are substantially better than the modified sextant protocol.

**Repeated biopsies.** In some cases, there can be clinical suspicion of undisclosed cancer after a negative biopsy. Examples include patients with high PSA level or with rising PSA level. Among these patients, repeated biopsy may detect cancer in 19–41% of the cases [22]. Logically with repeated negative biopsy, the likelihood of missing cancer diminishes with each sampling. However, biopsy is a quite invasive procedure and many complications like bleeding, pain/discomfort, infections and urinary retentions can be encountered, especially in case of repeated or systematic sampling protocols involving many cores.

### 2.2.5 Cancer staging and risk assessment

The dominant and most reliable method for prostate carcinoma diagnosis and aggressiveness assessment, in research as well as in clinical procedure, is the *Gleason grading* [13]. This method is based entirely on histological pattern of arrangement of carcinomas cells in contrast agents stained prostatic tissue sections. Specifically the method is a categorization of glandular differentiation and pattern of growth of the tumour, at relatively low magnification (x10 - x40) in five basic grades patterns [13] (see fig. 2.11). Due to the heterogeneous nature of prostate cancer lesions, histopathological inspection of prostate tissues often reveal an ensemble of benign lesions, preneoplastic lesions and neoplastic lesions with different aggressiveness. To take into account this heterogeneity, the five basic grade patterns are used to generate an histological score, which can range from 2 to 10, by adding the primary grade pattern and the secondary grade pattern. The primary pattern is the one that is predominant in area, by simple visual inspection. The secondary is the second most common pattern. For complete review of the method see [13].

The Gleason grading score is therefore an indicator of cancer stage: the higher is the grade, the more advanced is the cancer. Typically, cancers with Gleason scores lower than 6 are considered well differentiated and associated with a good prognosis. Those with a Gleason score of 8–10 have the worst prognosis and the highest risk of recurrence.

Gleason score is often combined with PSA level and clinical stage for risk assessment. The primary goal of staging is to distinguish patients with organ-confined, locally invasive, or metastatic diseases. For a complete review of prostate cancer staging and risk assessment see [16].

In fig. 2.12 different prostate cancer clinical stage stages are shown. At its initial stages (stage I), when confined into the prostatic capsule, prostate carcinoma is essentially curable by surgical intervention and/or radiation therapy. It cannot be felt during a digital rectal exam and usually is not visible by imaging. It is typically found accidentally during surgery for other reasons, such as benign prostatic hyperplasia. The Gleason score is low. Stage I prostate cancer may also be called stage A1 prostate cancer.

In stage II, cancer is more advanced than in stage I, but has not spread outside the prostate. The Gleason score can range from 2–10. Stage II prostate cancer may also be called stage A2, stage B1, or stage B2 prostate cancer.

In stage III, cancer has spread beyond the outer layer of the prostate to nearby tissues. Cancer may be found in the seminal vesicles. The Gleason score can range from 2–10.

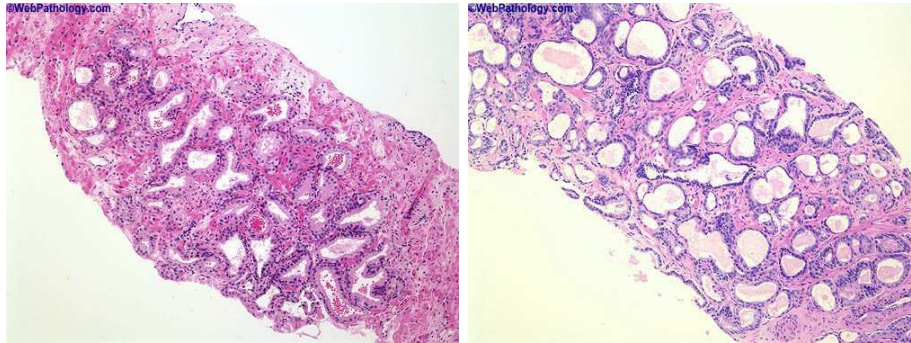


Figure 2.10: Examples of histologies, obtained with needle biopsy, of humane prostate tissue affected by atypical benign hyperplasia (left) and atrophic adenocarcinoma (right) respectively.

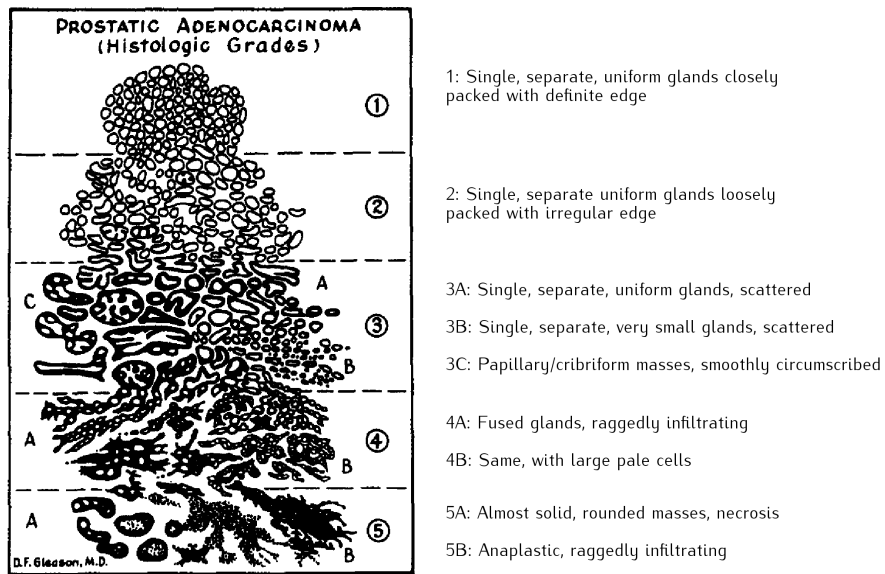


Figure 2.11: Gleason grades. (original Gleason's draw)

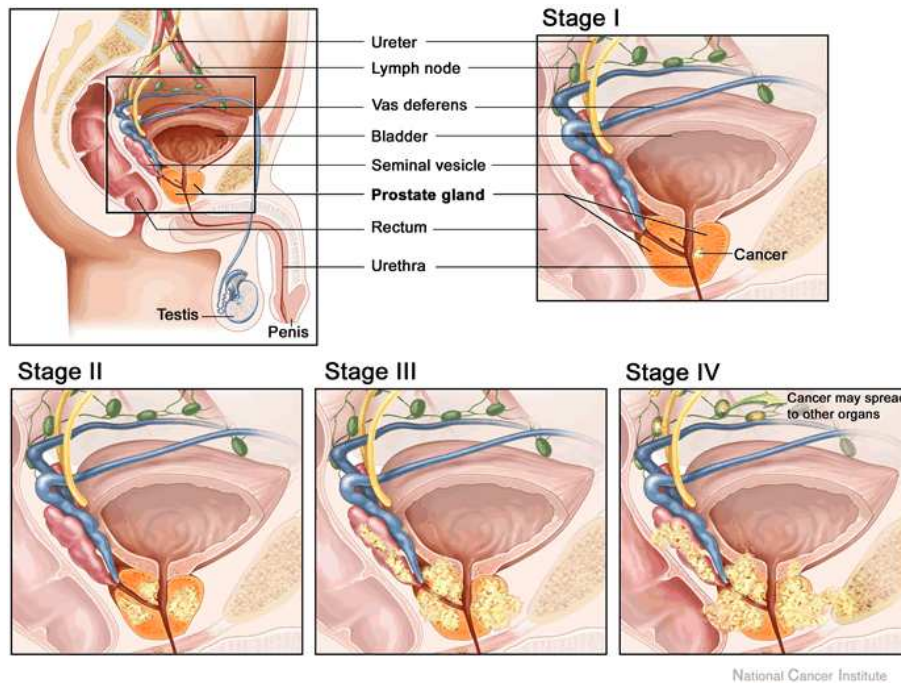


Figure 2.12: Prostate cancer stages. (picture taken from <http://www.cancer.gov/>)

Stage III prostate cancer may also be called stage C prostate cancer.

In stage IV, cancer has metastasized to lymph nodes near or far from the prostate or to other parts of the body, such as the bladder, rectum, bones, liver, or lungs. Metastatic prostate cancer often spreads to the bones. The Gleason score can range from 2-10. Stage IV prostate cancer may also be called stage D1 or stage D2 prostate cancer.

### 2.3 Future trends in US aided prostate cancer diagnosis

The early detection of prostate cancer is crucial for the success of treatments. Unfortunately, early prostate cancer usually has no symptoms. Moreover, as shown in this chapter, prostate cancer screening, diagnosis and staging is among the most controversial issues in modern public health, and the procedures involved have been a topic of continual debate since the early 1990s [20]. Besides, diagnostic conclusions can vary largely between individual urologists. This inter-observer variability may result in totally different decisions from the same set of diagnostic information [35]. Due to the lack of accuracy of imaging tests, the diagnosis procedure often unavoidably end with a histological confirmation by means of a biopsy.

Unfortunately, very often many biopsy are needed in order to obtain reliable results and in some cases, even when all the diagnostic tests have been carried out about 10% of incipient cancers go undetected because none of the biopsy needles insertion reached the lesion position [18].

One possible way of improving the accuracy of prostate cancer diagnosis procedure is to use computer-aided analysis (CAD) of the ultrasound image. The ultimate goal of these methods is to provide additional tools to the radiologists for improving the early detec-

tion rate of prostate cancer, reducing the inter-observer variability of diagnosis accuracy and avoiding unnecessary biopsies, guiding the biopsy needles into the suspicious regions. Among these methods 2D and 3D image segmentation, volume estimation, cancer detection and staging are the main task invoked in developing tools for aiding prostate cancer diagnosis,

Many works concerning CAD of prostate cancer have been published in literature. Although encouraging, the results published so far are often not proven to be clinically significant, or sometimes they cannot be considered representative, due to the limited number of patients used. Moreover, the performance published are not always comparable due to the different equipments employed, different way of selecting the region of interests to be classified (manual, automated), different type (regular, irregular) and size of the region of interests. For a complete review of the different methods published in literature see [27][35][18][20].

Although computerized analysis of ultrasound images is not likely to replace radiologists, it is expected that further development and improvement of this technology will continue to be an important area of research, and ongoing development of such algorithms will improve the diagnosis and treatment of prostate diseases in the near future.



## Chapter 3

---

# Neural signals analysis and modeling

---

The task of understanding the principles of information processing in the brain poses, apart from numerous experimental questions, challenging theoretical problems on all levels of modelling, from molecules to behaviour. The mammalian cortex is a complex system, characterized by its dynamics and architecture, which underlie many functions such as action, perception, learning, language, and cognition. Its structural architecture has been studied for more than a hundred years; however, its dynamics have been addressed much less thoroughly. The mammalian cortex appears to adhere to two fundamental principles of functional organization, functional integration and functional specialization, where the integration within and among specialized areas is mediated by connections among them.

Computational models at different space-time scales can help to understand the fundamental mechanisms that undergo neural processes and relate these processes to neuroscience data. Modelling at the single neuron level is necessary because this is the level at which information is exchanged between the computing elements of the brain. Mesoscopic models tell us how neural elements interact to yield emergent behaviour at the level of microcolumns and cortical columns. Macroscopic models can inform us about whole brain dynamics and interactions between large-scale neural systems such as cortical regions, the thalamus, and brain stem.

Each level of description is strongly related to neuroscience data, from single-unit recordings, through local field potentials to functional magnetic resonance imaging (fMRI), electroencephalogram (EEG), and magnetoencephalogram (MEG). Models of the cortex can establish which types of large-scale neuronal networks can perform computations and characterize their emergent properties.

In this chapter, a brief overview of mammalian neocortex architecture and information processing mechanisms is presented. A more detailed literature overview of the posterior parietal cortex, a portion of the parietal lobe which manipulates mental images, integrates sensory and motor portions of the brain and which is involved in formation of plans, is then given. Such area of the brain is particularly important for the development of brain computer interfaces (BCI) for the control of artificial motor prosthesis. Behavioural experiments performed by trained monkeys and the data analysis procedure applied on neural activity recorded through the experiment are described in detail.

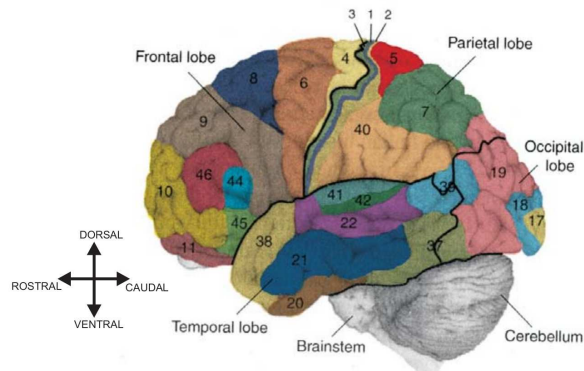


Figure 3.1: Lateral view of the left hemisphere of the human brain: the four lobes with the cerebellum and brainstem.

### 3.1 Brain structure and neurophysiology

Primate neocortex can be roughly divided in six, anatomically and functionally distinct, regions: frontal, temporal, occipital, parietal, cingulate and insular cortex as shown in fig.3.1. Frontal, temporal, occipital and parietal lobes are located on the lateral surface of the neocortex, while cingulate cortex occupies the medial surface surrounding the corpus callosum, the set of fibers that connects right and left cerebral hemispheres. Finally, the insular cortex occupies the region that separates the temporal, from the parietal and frontal cortex, and is ejectionally hidden by the overgrowth of these three lobes.

An important feature of the primate cortex is its specific shape, composed of alternating elevated convex and depressed concave regions, called gyri and sulci, respectively. Three particularly pronounced sulci are used to define the borders between the cortex regions the lateral sulcus (the sylvian fissure) separates the temporal from the parietal and frontal regions, the central sulcus separates the frontal from the parietal lobe, and the parieto-occipital sulcus separates the parietal from the occipital lobe [15].

The thickness of the cortex is 2-4mm for most of the species, and it can be divided into six layers according to the typical cell types present. In general, the same structure is observed in most of the cortex regions, but the variations in thickness of certain layers, and in intensity of fibres enables their identification. Thus, according to the widely accepted anatomy-based definition proposed by K. Brodmann in 1909, the cortex areas can be further divided in 47 sub-areas according to their neural cells organization. For further details see [15].

Alternative cortex study is based on identification of functional regions, for example, according to their role in sensory information processing and generation of motor commands. Information processing in brain is highly hierarchical: the information received through periphery sensory cells is transmitted to the primary sensory regions, then further to the unimodal association areas that integrate information related to one single type of sensations, e.g. vision, auditory sensations etc. In the multimodal associative areas, sensations of different modalities are then integrated, in order to extract more complex information and generate output signals. These signals are further conveyed to the primary motor association areas responsible for initial planning of motor commands. Finally the premotor and primary motor cortex directly control movements, following the received inputs.

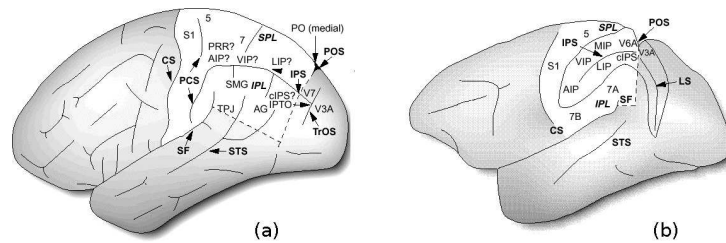


Figure 3.2: Posterior parietal cortex areas in human (a) and mokey (b) brain.

### Posterior parietal cortex

The parietal cortex (PC), shown in fig.3.1, is anatomically defined by the positions of the three pronounced sulci: the lateral sulcus, the central sulcus and the parieto-occipital sulcus. Brodmann areas 1,2, and 3, placed on the postcentral gyrus, are the most anterior part of the parietal cortex, and represent the primary somatosensory region. The posterior parietal cortex (PPC) in humans extends to the supramarginal and angular gyrus, the regions classified as Brodmann area 40 and 39, respectively. The latter occupies the junction of the parietal, temporal and occipital lobes. These two areas are involved in language processing, spatial orientation and semantic representation. They are described only in the context of studies in humans, since no evidence of the equivalent regions is found in monkeys [21].

The regions of interest for this work are the Brodmann areas 5 and 7, the surface inside the intraparietal sulcus (IPS), and the related regions on the medial wall of the hemisphere. In humans, both regions 5 and 7 belong to the superior parietal lobe (SPL), while the inferior parietal lobe (IPL) refers to the Brodmann areas 39 and 40. The anatomical organization of the monkey cortex is somewhat different and SPL contains the area 5, while the area 7 belongs to the IPL. Since most of the presented conclusions come from the studies on monkeys, the terms PPC, SPL and IPL will be mostly used in the context of the monkey cortex. Their anatomy and functional roles will be described in more details in the following sections.

Different informations about the PPC functions have been collected through clinical examination of patients with parietal lesions. Equivalent studies are carried on monkeys after chirurgical removal of certain regions in PPC, in order to monitor the consequences [7][21]. Typically, the patients had no significant visual, somatosensory or motor disorders, but they demonstrated deficits in reaching and grasping objects and in visually guiding reaching and grasping. In fig. 3.2, an overview of the PCC regions and their positions on the neocortex in human and monkey brain is given.

An brief overview of the main properties of the main regions of monkey PCC in now given. For a complete review see [21]. Most of these properties were obtained by recording activity in the brain of monkeys, trained to follow visual or auditory commands. In a typical setup a monkey is placed in front of a screen and instruction for controlling the experiment are given. Several electrodes are inserted into the area of interest tissue to record the extracellular potential of singular cells. Finally spike trains are extracted form these signals and used to analyze cells behaviour dynamic during the experiments and deduce it functionality.

**Medial intraparietal region (MPI)** . It is usually related to planning of reaching movements and it is considered the part of the area 5, and therefore, the part of the superior parietal lobe. This region is believed to take part in spatial representation for control of arm movements and providing signals for visually guided reaching for the motor-related regions.

**Lateral intraparietal region (LIP).** It is a part of the inferior parietal lobe (IPL) in the monkey cortex and it receives inputs from the extrastriate cortex and it is connected to other visually related PCC regions. This region is often related to planning eyes movements toward both, the visual and auditory stimuli.

**Ventral intraparietal region (VIP).** It receives several visually and motion related areas, together with inputs from somatosensory regions, and projects to the area F4 of the pre-motor cortex, responsible for head and mouth movements. This region integrates visual and somatosensory information and initiates corresponding motor activities.

**Anterior intraparietal region (AIP).** It is believed to contribute to the hand shaping and grasping of 3D objects. The populations of visually and motor responsive cells were found in this regions indicating that it contributes to control of visually guided movements.

**Broadmann area 5.** As a part of the superior parietal lobe (SPL), is a motor-related region, playing role in the planning and coordination of hand reaching movements. It represents the source of most of the inputs to the motor and premotor regions of the frontal lobe, supplying the information necessary for initiation of the reaching movements. Some studies highlighted the presence in this area of spatial representation of hand and target positions, and of the appearance of intention and attention before a movement.

**Brodmann area 7.** It is a part of the inferior parietal lobe (IPL) in the monkey cortex, and is usually anatomically divided into the regions 7a and 7b. The first of them is of particular interest for the presented work, and some of its properties are examined in the following sections. The area 7a receives multiple visual inputs, mainly from the areas V2, PO, the superior temporal sulcus and the dorsal prelunate gyrus.

**Brodmann area 7m.** As part of the medial parietal cortex is considered to be the early stage in the control of a visually guided reaching. It receives inputs from the visual areas of the occipitoparietal cortex, and projects to the dorsal premotor cortex and it is believed to contribute in planning of motor commands for hand movements or visual monitoring of hand trajectories.

The studies on patients with parietal lesions indicate that PPC act as an interface between sensory processing and motor and premotor regions. The PPC receives sensory inputs of different modalities like visual and auditory signals, somatosensory inputs and information about the positions of limbs, hands and eyes, and plays a crucial role in integrating such information in the early stages in planning motor activities, generating commands for movements of hands, limbs and eyes on a more abstract level. In particular, in [8] and [9] a study on the mechanisms that coordinate eyes and hand movements in parietal area 7a (inferior parietal lobule of the posterior parietal cortex) of trained monkeys performing several eye-hand directional motor tasks, is presented.

### 3.2 Experimental data and data analysis procedures

In [3], the signal recorded in n [8] and [9] were studied through data analysis and machine learning techniques for the identification of motor intention, the early motor plan, in the PPC and on the directional tuning of cells activity . In the neurophysiological literature, the (motor) intention is defined as an early plan for movement that specify the goal and the type of the movement but does not, necessarily, contain the explicit commands for the motor neurons, necessary for executing that movement [4]. Therefore, motor intention is an important high level and abstract representation of a movement that can be used as input for computer or for controlling mechanical devices in brain computer interfaces. Such studies aim to provide sophisticated prosthesis for patients with movement disorders, and help them to improve the quality of their life.

The set of behavioural tasks performed by monkeys were designed in order to assess the questions of interest. Two rhesus monkeys were seated in front of a touch-sensitive screen, and trained to follow the instruction signals, presented on the screen. Simultaneously, the neural activity in the 7a area of the parietal lobe was monitored through a 7-channel multielectrode recording system. This allowed the recording of up to 14 cells simultaneously in each recording. All the details on animals, experiments and the recording system are presented in [8] and [9].

**Behavioural tasks description.** At the beginning of all the trial, a red light is turned on the center of the screen. The animal is required to gaze and touch this target for a variable period, indicated as CHT (Control Holding Time). At the end of the CHT, the red light is turned off, and the monkey is required to follow a given, task specific, instruction. Such instruction is contained in a visual target signal that appears in one of eight peripheral positions fig. 3.3. According on the task, the animal is supposed to either reach for the target, or wait for the go signal first, and than reach for it. Typically, each task is executed for variable target positions, and several repetitions. One complete block of data consists of four trial replications, for each of the 8 target positions, in each of the six behavioural tasks, plus three repetitions for sixteen target positions in the last task given on fig. 3.3.

In the reach task (RT), as soon as the target appears, the monkey reacts first moving the eyes toward the target, then the hand follows in coordination with the eyes. The reach fixation task (RFT) requires a fixed position of the eyes at the center of the screen, from the beginning till the end of the trial. After its presentation, the monkey locates the target position by the peripheral vision, and moves the hand only toward it. Coordination between the eyes movement and the hand movement is not required by this task.

Three memory tasks (MT) start with the presentation of an instruction signal in one of the 8 positions. After 300 milliseconds, this signal goes off, and the monkey must remain firm for a variable memory-delay time, until the go-signal appears on the screen. After the go-signal, the monkey is required to move both the eyes and the hand (memory reach, MR) toward the memorized target location; or just the hand (memory reach-fixation, MRFT), while keeping the eyes fixed on the center; or just eyes (memory eye, ME), with the hand firm on the center of the workspace.

Finally, in the no-go task (NGT), the monkey keeps the eyes and the hand immobile during the entire trial. This task was used for monitoring the neural activity in a behavioural condition where the instruction signal, presented as in the other memory tasks, did not call for any future eye and/or hand movement, but rather for not to move the eye and/or the

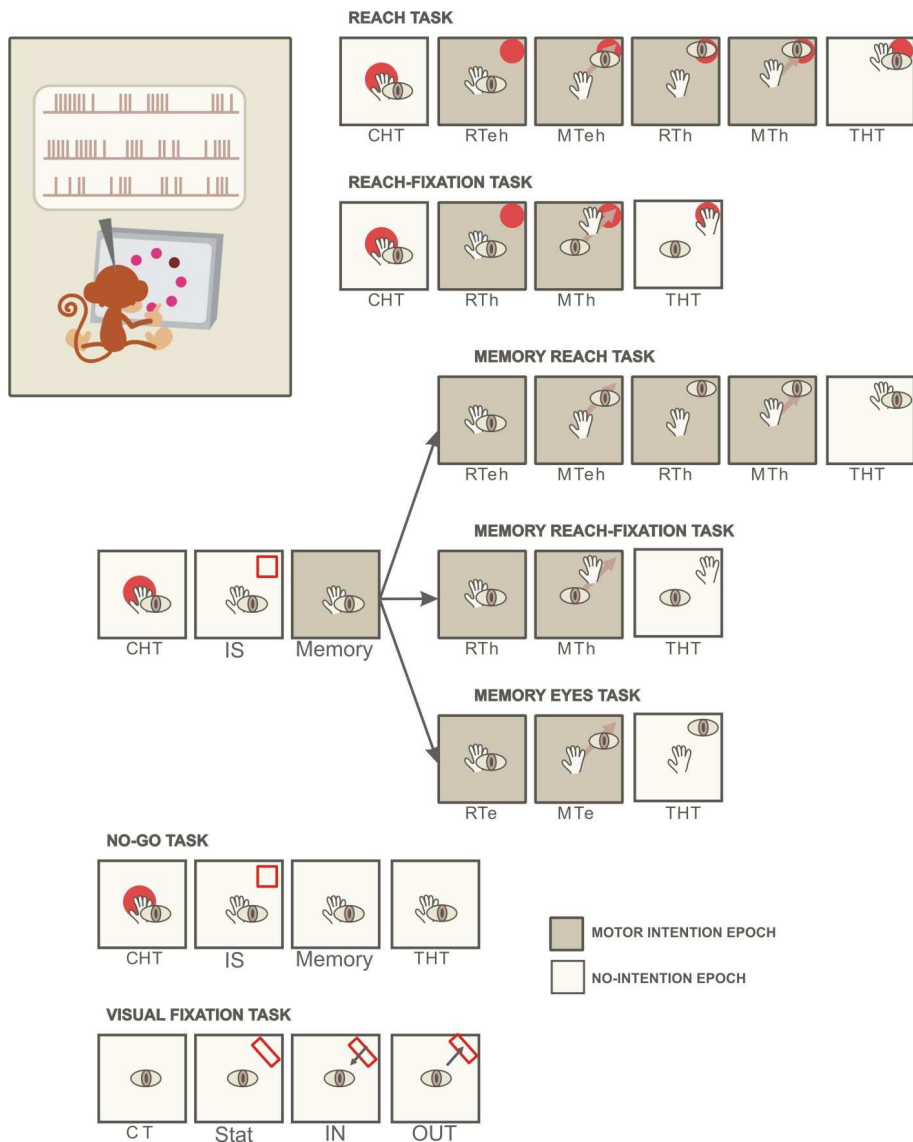


**Figure 3.3:** Schematic representation of the experiments. (Picture kindly provided by J. Acimovic)

hand. The epochs corresponding to each of the tasks are presented in fig. 3.3.

**Neural activity and data analysis.** Two data bases of spike rates were available as the outcome of the described experiments. The schematic representation of one of them is given in fig. 3.4. The presented example consists of forty five 'files', while the second data base has fifty seven files. The 'file' stands for spike trains from individual cells, each recorded from a fixed array of electrodes (up to 7), including signals for the six tasks, eight target positions, and four trials for each combination (Task, Target). Also, each 'file' includes the recordings for the seventh task, from sixteen target positions and three repetitions. Each data set within a 'file' contains of at most fourteen recorded spike trains, since from each electrode recording, neural activity from up to two different cells was collected, together

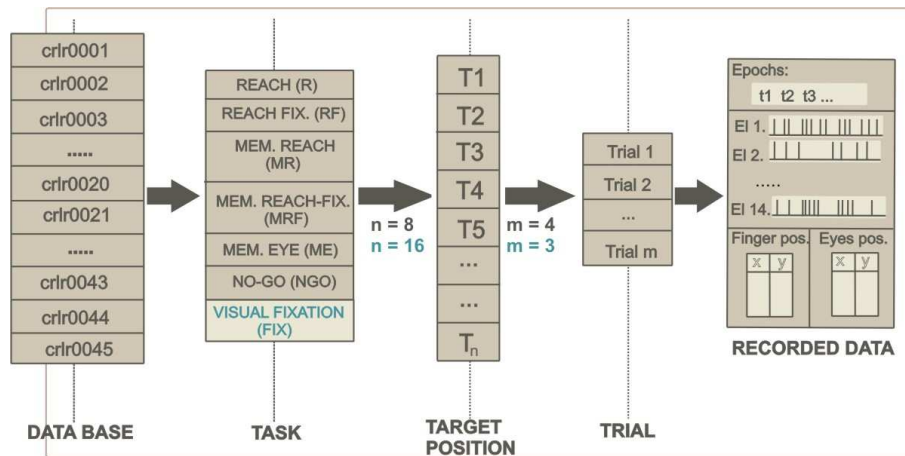


**Figure 3.4:** Schematic representation of the data base. The example corresponds to the recording of one monkey collected for 45 electrode positions. (Picture kindly provided by J. Acimovic)

with corresponding epoch marks, i.e. markers denoting the beginning and the end of each behavioural epoch within a trial. The markers were determined by continuous recording of eyes and hand position in each trial.

The two described data bases are analyzed separately and within one data base all files are considered separately since different files correspond to different electrode positions and therefore, it was not possible to combine them in the common decoding task. Moreover all the recording set not resulted in a complete data set of data for the specific task were discarded.

Finally, since different files correspond to different recording regions, a separate classifier was constructed for each file. The problem of interest is to distinguish between spike train recordings which encode the intention for making a movement, from those corresponding to absence of movement planning. With the term 'movement' we mean any movement involving the eyes or the hand. The underlying hypothesis is that the presence of intention for moving is encoded in the modulation of the firing rate of the recorded neurons. This is a plausible assumption for the particular recorded set of neurons, the brain region named posterior parietal cortex, which is believed to participate in eye-hand coordination in primates [8][9]. Therefore, it is realistic to expect that neurons in this region become more active, as a way to increase their information transfer, during the epochs generally believed as corresponding to 'planning and making a movement', which we call 'motor intention' in this work.

To investigate the hypothesis that motor intention is encoded in the neural activity and to support the possibility of extracting it through the analysis of the neural activity at fire rate level, two different machine learning based algorithms were developed. In the first method only the epochs directly involved in the eye-hand coordination task are considered. Knowing the key processes related to each of the epochs, we can straightforwardly assign presence or absence of 'motor intention' to some of them. Since the behaviour of the monkeys is not so well determined, especially in certain experimental phases, some ambiguity about the classifier output is always present. The goal of this method was to test the aptitude of

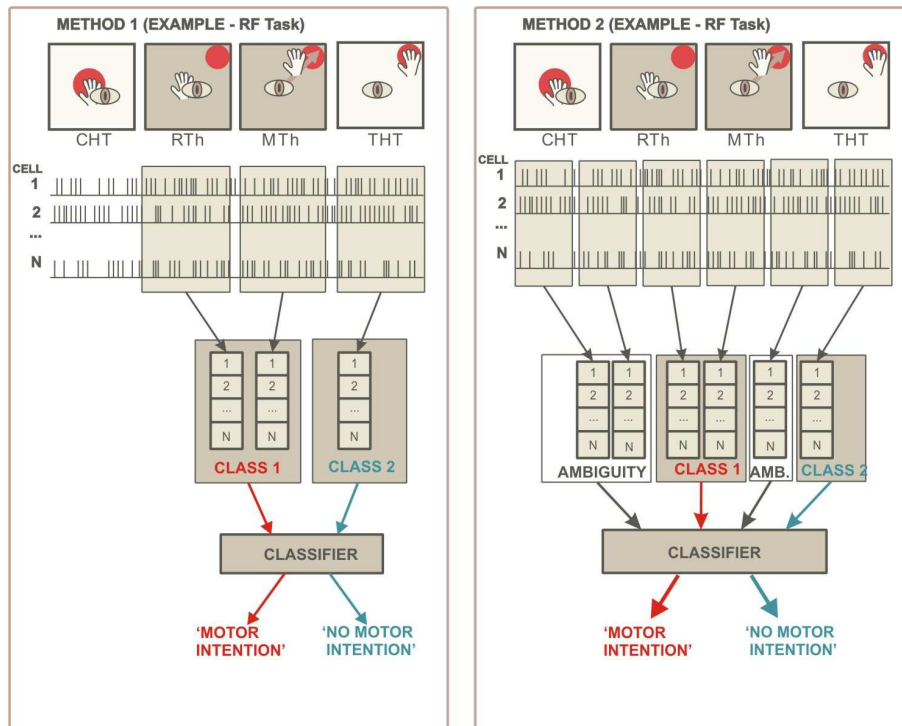


Figure 3.5: Schematic representation of the classification procedure. (Picture kindly provided by J. Acimovic)

a sophisticated algorithm to read the presence/absence of 'motor intention' from the cortex area under study, allowing us to test the limitations imposed by the experiments design, and analyzing the expected results when those limitations are removed. An overall scheme of the whole procedure is shown in fig. 3.5.

The second approach doesn't take into account the notion of experiment epochs, and focuses 'motor intention' detection in time. Continuous recordings, from the beginning to the end of a trial, were considered rather than just a set of selected epochs. The number of data examples, as well as the temporal resolution, is defined by introducing a time window. The window is moving along the spike train in discrete time steps, with the predefined time shift. For each distinct window position, spike rates are calculated in the standard way, as the number of spikes within the window divided by the window size. A set of recordings obtained simultaneously provides one vector of spike rates. Several choices for the window length were tested, from 100 ms to 1sec. These values correspond to the dynamics of the experimental epochs, the smallest among them are several hundreds of milliseconds long, the longest ones last for a couple of seconds. The window shift is fixed to the half of its length, for every choice of the window. The definition of experiment epochs is therefore considered only in the training phase and discarded in the classification phase. This procedure represents a more complex problem, since different and sometimes unknown information that are encoded in the neural activity get mixed even more than in the first method. However, it allows estimating the probability of detecting the presence/absence of motor intention in a set of simultaneously recorded spike trains not a priori segmented into epochs, giving additional information regarding the considered processes. An overall

scheme of the whole procedure is shown in fig. 3.5.

**Results and critical parameters** The results obtained with both the first and the second procedure and presented in [3]. The first procedure show very good performance, confirming the hypothesis of motor intention encoding in the neural activity. The classification error never exceeds 30% of wrongly classified data instances. The average performance, calculated over the complete set of available files for one data base, reveals the desired behaviour: the average error amounts to 4.33% and 6.58% error for the two considered data bases. However, the obtained result shows a big variance with respect to the different files, highlighting the effect of choosing different cells.

The precision obtained with the second procedure strongly depends on the window size. A very small window enables the analysis of small recording segments and better precision, but, at the same time, it deteriorates the classification procedure. Therefore, the chosen window size should be as small as possible, but sufficiently big to ensure enough variability in obtained spike rate values. The classification error obtained with this procedure does not exceed 40%, while the average error stays below 30%.

Such limitation, gave the motivations for developing an abstract model which behaviour resembles that of the biological system and can be used to test some relevant parameters of the machine learning procedure presented in [3]. The model is presented in detail in chapter 6.



---

## Bibliography

---

- [1] Dictionary of cancer terms. U.S. National Cancer Institute website. <http://www.cancer.gov/dictionary/>. [cited at p. 25]
- [2] C. Abate-Shen and M.M. Shen. Molecular genetics of prostate cancer. *Genes & Development*, 14(19):2410–2434, 2000. [cited at p. 24, 25]
- [3] J. Acimovic, A. Battaglia-Meyer, R. Caminiti, and M. Hasler. Automatic methods for motor intention recognition from spike rates. In *International Symposium on Nonlinear Theory and its Applications*, pages 361–364. NOLTA, September 2007. [cited at p. 41, 45]
- [4] R. A. Andersen and C. A. Buneo. Intentional maps in posterior parietal cortex. *Annu. Rev. Neurosci.*, 25:189–220, 2002. [cited at p. 41]
- [5] J.C. Applewhite, B.R. Matlaga, D.L. McCullough, and M.C. Hall. Transrectal Ultrasound and Biopsy in the Early Diagnosis of Prostate Cancer. *CANCER CONTROL*, 8(2):141–150, 2001. [cited at p. 28, 29]
- [6] Various Authors. Cancer facts and figures, 2007. [Online; accessed 01–December–2008]. [cited at p. 26]
- [7] A. Battaglia-Mayer, P.S. Archambault, and R. Caminiti. The cortical network for eye–hand coordination and its relevance to understanding motor disorders of parietal patients. *Neuropsychologia*, 44(13):2607–2620, 2006. [cited at p. 39]
- [8] A. Battaglia-Meyer, M. Mascaro, M. Brunamonti, and R. Caminiti. The over-representation of contralateral space in parietal-cortex: a positive image of directional motor compensation of neglect? *Cerebral Cortex*, 15:514–525, 2005. [cited at p. 40, 41, 43]
- [9] A. Battaglia-Meyer, M. Mascaro, and R. Caminiti. Temporal evolution and strength of neural activity in parietal cortex during eye and hand movement. *Cerebral Cortex*, 17:1350–1363, 2007. [cited at p. 40, 41, 43]
- [10] E. Brunner. How Ultrasound System Considerations Influence Front-End Component Choice. *Analog Dialogue*, 36(3), 2002. [cited at p. 16]
- [11] J. DE LA ROSETTE, RJB GIESEN, AL HUYNEN, RG AARNINK, MP VAN IERSEL, FMJ DEBRUYNE, and H. WIJKSTRA. Automated analysis and interpretation of transrectal ultrasonography images in patients with prostatitis. *European urology*, 27(1):47–53, 1995. [cited at p. 30]

- [12] CR Hill. *Physical Principles of Medical Ultrasonics*. Jhon Wyley & Sons, 1986. [cited at p. 7, 11]
- [13] P.A. Humphrey. Gleason grading and prognostic factors in carcinoma of the prostate. *Modern Pathology*, 17(3):292–306, 2004. [cited at p. 32]
- [14] A. Jemal, R. Siegel, E. Ward, T. Murray, J. Xu, and M.J. Thun. Cancer Statistics, 2007. *CA: A Cancer Journal for Clinicians*, 57(1):43–66, 2007. [cited at p. 26]
- [15] E.R. Kandel, J.H. Schwartz, and T.M. Jessell. *Principles of Neural Science*. Appleton & Lange, 2000. [cited at p. 38]
- [16] V. Kundra, P.M. Silverman, S.F. Matin, and H. Choi. Imaging in Oncology from The University of Texas MD Anderson Cancer Center: Diagnosis, Staging, and Surveillance of Prostate Cancer. *American Journal of Roentgenology*, 189(4):830–844, 2007. [cited at p. 26, 28, 32]
- [17] P.A. Lewin. Quo vadis medical ultrasound? *Ultrasonics*, 42(1-9):1–7, 2004. [cited at p. 21]
- [18] R. Llobet, J.C. Pérez-Cortés, A.H. Toselli, and A. Juan. Computer-aided detection of prostate cancer. *International Journal of Medical Informatics*, 76(7):547–556, 2007. [cited at p. 30, 34, 35]
- [19] J.E. McNeal. Origin and development of carcinoma in the prostate. *Cancer*, 23(1):24–34, 1969. [cited at p. 24]
- [20] M. Moradi, P. Mousavi, and P. Abolmaesumi. Computer-Aided Diagnosis of Prostate Cancer With Emphasis on Ultrasound-Based Approaches: A Review. *Ultrasound in Medicine & Biology*, 33(7):1010–1028, 2007. [cited at p. 30, 34, 35]
- [21] VB Mountcastle, JC Lynch, A. Georgopoulos, H. Sakata, and C. Acuna. Posterior parietal association cortex of the monkey: command functions for operations within extrapersonal space. *Journal of Neurophysiology*, 38(4):871–908, 1975. [cited at p. 39]
- [22] J. Raja, N. Ramachandran, G. Munneke, and U. Patel. Current status of transrectal ultrasound-guided prostate biopsy in the diagnosis of prostate cancer. *Clinical Radiology*, 61(2):142–153, 2006. [cited at p. 29, 30, 32]
- [23] G. Ravizzini, B. Turkbey, K. Kurdziel, and P.L. Choyke. New horizons in prostate cancer imaging. *European Journal of Radiology*, 2008. [cited at p. 28, 30]
- [24] MD Rifkin, ET McGlynn, and H. Choi. Echogenicity of prostate cancer correlated with histologic grade and stromal fibrosis: endorectal US studies. *Radiology*, 170(2):549–52, 1989. [cited at p. 29]
- [25] U. Scheipers, H. Ermert, HJ Sommerfeld, M. Garcia-Schurmann, T. Senge, and S. Philippou. Ultrasonic multifeature tissue characterization for prostate diagnostics. *Ultrasound Med Biol*, 29(8):1137–49, 2003. [cited at p. 17]
- [26] G. Schmitz, H. Ermert, and T. Senge. Tissue-characterization of the prostate using radio frequencyultrasonic signals. *Ultrasonics, Ferroelectrics and Frequency Control, IEEE Transactions on*, 46(1):126–138, 1999. [cited at p. 17]

- [27] JPM Sedelaar, J. de la Rosette, HP Beerlage, H. Wijkstra, FM Debruyne, and RG Aarnink. Transrectal ultrasound imaging of the prostate: review and perspectives of recent developments. *Prostate Cancer and Prostatic Diseases*, 2(5-6):241–252, 1999. [cited at p. 35]
- [28] S. Shetty. Transrectal ultrasonography (TRUS) of the prostate. *available on <http://emedicine.medscape.com/article/457757-overview>*, may 2008. [cited at p. 28]
- [29] T.L Szabo. *Diagnostic ultrasound imaging*. Elsevier, 2004. [cited at p. 17, 19]
- [30] Wikipedia. Cancer — Wikipedia, the free encyclopedia, 2008. [Online; accessed 01-December-2008]. [cited at p. 25]
- [31] Wikipedia. Prostatitis — Wikipedia, the free encyclopedia, 2008. [Online; accessed 01-December-2008]. [cited at p. 25]
- [32] Wikipedia. Seminal vesicles — Wikipedia, the free encyclopedia, 2008. [Online; accessed 01-December-2008]. [cited at p. 23]
- [33] Wikipedia. Tumor — Wikipedia, the free encyclopedia, 2008. [Online; accessed 01-December-2008]. [cited at p. 23, 25]
- [34] Wikipedia. Tumor — Wikipedia, the free encyclopedia, 2008. [Online; accessed 01-December-2008]. [cited at p. 25]
- [35] Y. Zhu, S. Williams, and R. Zwiggelaar. Computer technology in detection and staging of prostate carcinoma: A review. *Medical Image Analysis*, 10(2):178–199, 2006. [cited at p. 34, 35]



# Part II

## APPLICATIONS



## Chapter 4

---

# Ultrasound signal deconvolution

---

Ultrasounds scanners are a cost effective, mobile, noninvasive, harmless, and suitably accurate imaging equipments and are widely used in medical imaging applications. The main drawback of ultrasound imaging is that signal resolution is low if compared to the other imaging technique. Ultrasound images often suffer of characteristic artefact's like attenuation, speckle, shadows and signal dropouts, missing boundaries due to the orientation dependence of acquisition, which make the diagnosis hard.

One of the main limitation in signal resolution is upper bound on signal frequency imposed by tissues attenuation. As reviewed in chapter 1, the attenuation of soft tissues increases linearly with the frequency, limiting in deep scanning the maximum frequency to 10 MHz. This relatively low frequency causes the presence of a non-negligible diffused component in the echo field, which appear as a signal dependent noise often called speckle.

Another cause of signal quality degradation is the finite bandwidth of the piezo-electric transducer of the system probe which, together with their small size imposed by medical applications and limitations of beamforming system, causes a non-negligible dimension of the transmitted acoustic beam and therefore an imperfect focusing. Ultrasound images are thus affected by a spatial dependent blurring which causes distortion and smoothing of tissues details, as well as a degradation of image contrast.

Many signal and image processing techniques like de-speckling [23] and deconvolution have been used with the purpose of enhancing ultrasound image quality. Although theoretically denoising and deconvolution of signals are two aspects of the same problem, i.e. signal restoration, and they should be treated jointly, in many works presented in literature they are often tackled with different and independent procedures. Both of the problems are in fact challenging tasks that require complex signal processing techniques to be solved. Moreover, although speckle noise degrades image quality, it contains valuable information about the tissue microstructure and many authors claim that such information is fundamental for tissue characterization and therefore it should be preserved [34][29].

**Author contributes.** In this chapter, we will focus our attention on deconvolution techniques for ultrasound signals and, after an original review of the approaches existing in literature, a stochastic signal model and a statistical framework for ultrasound signal deconvolution is presented.

## 4.1 Literature overview

Image restoration techniques, such as deconvolution, can be employed to improve the resolution of ultrasound images reducing the spatial dependent blurring introduced by the beamforming system, with the goal of improving their diagnostic significance. In deconvolution techniques, the blurring affecting the image is modelled as linear and in general three-dimensional function  $h(\vec{r})$ , called point spread function (PSF), which filters the real tissue response  $x(\vec{r})$

$$y(\vec{r}) = x(\vec{r}) * h(\vec{r}) \quad (4.1)$$

as reviewed with a different notation in chapter 1. Such model is valid until Born and weak scattering approximation are valid.

Theoretically speaking, as the system PSF is a band-limited function and due to the presence of noise, signal deconvolution is an ill-posed problem. To obtain a stable algorithm delivering a unique solution, additional constraints must be imposed. Therefore, designing a method which exhibits the most suitable compromise among computational complexity, reliability and portability for biomedical real-time imaging applications is still an open challenge. Good reviews of the existing approaches for image deconvolution are in [17] [6] [11].

In literature, two main approaches are most common when dealing with image deconvolution. The first incorporates the Point Spread Function (PSF) estimation procedure within the deconvolution algorithm. This approach often leads to the development of computationally heavy algorithms, usually far from satisfying the real-time signal processing constraints distinctive of the US biomedical investigation environment. In the second approach, PSF and true image estimation are two disjoint tasks. Within this approach, these procedures can be implemented by relatively simple algorithms, possibly suitable for real-time implementation.

Since a recent review on the existing techniques for ultrasound image deconvolution is missing, a brief comparison the main paper published so far will follow. Such comparison will focus on:

- data type (simulated, phantom object, biological tissue, materials);
- transducer central frequency;
- sampling frequency;
- signal resolution;
- signal model (1D, 2D or 3D);
- PSF type (minimum or mixed phase);
- PSF estimation technique;
- deconvolution method.

The main works concerning deconvolution methods for ultrasound signals published so far are summarized in table 4.1.

Unlike in the context of image processing, where procedure for joint estimation of system PSF and deconvolution were applied with success, practically all the methods for ultrasound signal deconvolution are based on two disjoint procedures for PSF estimation and

WORK	DATA			
	Type	Probe	Sampling	Resolution
Jirik 2008 [14]	in vivo tissues	2.5-3.5 MHz	3-4 Mhz*	14 bits
Michailovich 2007 [21]	in vivo tissues	3.5 MHz	25 Mhz	14 bits
Ng 2007 [27]	simulated and in vivo phantoms	5-10 MHz	66.6 MHz	-
Michailovich 2005 [22]	in vivo tissues	3.5 MHz	25 Mhz	14 bits
Neelamani 2005 [25]	images	-	-	-
Michailovich 2004 [20]	simulated and in vivo	3.5 MHz	25 Mhz	14 bits
Michailovich 2003 [19]	simulated and in vivo	3.5 MHz	25 Mhz	14 bits
Wan 2003 [36]	in vivo tissues	33-44 Mhz	200 MHz	-
Adam 2002 [3]	in vivo tissues	3.5 MHz	25 Mhz	14 bits
Taxt 2001 [32]	in vivo phantom	8 MHz	20 MHz	-
Karensen 1999 [15]	in vivo material	10 MHz	-	-
Taxt 1999 [33]	in vivo tissues	3 MHz	10 Mhz	8 bits
Arbeytrane 1995 [2]	in vivo phantoms	3.5 MHz	12 MHz	-
Jensen 1994 [13]	in vivo tissues	3 MHz	20 MHz	-

\* sampling rate after quadrature demodulation.

(a)

WORK	METHOD		
	Type	PSF estimation	Reflectivity estimation
Jirik 2008 [14]	2D	MP - iterative bayesian	Iterative bayesian
Michailovich 2007 [21]	2D	MP, see [22]	Parametric inverse filter
Ng 2007 [27]	3D	MP - known, time varying	EM procedure
Michailovich 2005 [22]	2D	MP - cepstrum denoising, phase unwrap	MAP Gaussian and Laplacian
Neelamani 2005 [25]	2D	MP - known	Fourier-Wavlet reg. inversion
Michailovich 2004 [20]	2D	MP - phase unwrap	-
Michailovich 2003 [19]	1D	mP - cepstrum wavelet denoising	-
Wan 2003 [36]	1D	mP - higher order cep.	Fourier-Wavlet reg. inversion
Adam 2002 [3]	1D	mP - wavelet reg cepstrum	Approximated inversion
Taxt 2001 [32]	3D	MP - complex cepstrum	Wiener filter
Karensen 1999 [15]	1D	MP - time varying	MAP bernoulli gaussian
Taxt 1999 [33]	1D	MP - noise robust	Wiener filter
Arbeytrane 1995 [2]	1D	MP - higher order cep.	Wiener filter
Jensen 1994 [13]	1D	mP - cepstrum	Wiener filter

Legend:

mP = minimum phase - MP = mixed phase

(b)

**Table 4.1:** Comparison of the published methods for ultrasound signal deconvolution.

tissue reflectivity recovery. The only exception is constituted by the work presented in [14] where the system PSF and tissue reflectivity are iteratively estimated through a Bayesian procedure which uses a cepstrum based method as initial estimation of the system PSF. The main reason behind the difficulties in applying blind deconvolution procedures on us images is that while in classical deconvolution context like astronomy all algorithms are applied in image domain, in ultrasound images deconvolution is performed on the radio frequency signal obtained by the ultrasonic transducer (see chapter 1 for further details). In this signal domain, many regularization priors that are usually exploited can't be used.

Most of the published procedures are applied to relatively low frequency imaging system (3-3.5 Mhz) where the benefits of deconvolution are more evident, although some works on higher frequency (5-10 MHz) [15][32][27] and on high frequency systems (33-44 MHz)[36] were presented.

Although the physical nature of ultrasound image formation suggests a three-dimensional model for the observed signal, except [32] and [27], all the method reported in literature are based on 1D or 2D signal models. Such simplification is due to the fact that all the commercial ultrasound image equipments provides 2D images and real three-dimensional scanners

have been introduced only recently. Moreover, since 1D deconvolution methods doesn't require the memorization of the whole image, the processing can be ideally performed during the signal acquisition.

Estimation of imaging system PSF with good accuracy has appeared to be a difficult and challenging problem [21][14]. The most successful techniques are all based on homomorphic blind deconvolution methods [28]. In particular cepstrum-based techniques and their generalization [13] [19] have been demonstrated to provide a good estimation of PSF power spectrum. While power spectrum can be easily estimated with good precision, phase estimation is not so straightforward, mainly due to the requirement of phase unwrapping, which is an ill-posed problem [21]. Since the assumption of minimum-phase seems to be not applicable in most of US imaging systems, either robust phase estimation procedure or deconvolution methods that can estimate true tissue reflectivity relying only on partial information about system PSF are required [21][14].

Once the PSF is estimated, tissue reflectivity can be estimated applying to the observed signal the regularized inverse operator of the PSF. Regularization is mandatory due to the presence of noise in the observed signal and in general non-perfect knowledge of system PSF. While many approach for PSF estimation have been proposed, less interest have been dedicated to reflectivity estimation. The first and simplest method employed for reflectivity estimation is the Wiener's filter, which can be considered as a  $L^2$ -norm regularization of the solution. Wiener filter, together with  $L^1$ -norm regularization, is a standard reference deconvolution technique. Most of the published works employ these two procedures for signal de-blurring. However, recently new approaches based on Expectation Maximization [27], Bayesian estimation [14] and parametric inverse filter [21] have been proposed. All of these approaches try to overcome to the main limitations of Wiener and Laplacian filter, that tends to produces oversmoothed and too sparsified solutions respectively, due to unrealistic signal models.

All the techniques proposed in literature can be set in a statistical framework which allows highlighting their main features and limitations. Thus, in the following section a statistical model of the US radio frequency signal will be introduced. Such model will be then used as starting point for the development of a novel reflectivity estimation procedure that will be explained in this chapter.

## 4.2 Proposed approach

As reviewed in chapter 1 and in [26], if the propagation is linear, each A-lines of an ultrasound imaging system can be mathematically modelled as the convolution between tissue reflectivity and system point spread function. Without loss of generality, we can adopt a discrete space-time and consequently introduce a vector matrix notation and writing the observed signal as:

$$\mathbf{y} = \mathbf{H}\mathbf{x} + \mathbf{n} \quad (4.2)$$

where  $\mathbf{x}$  is the original data vector,  $\mathbf{H}$  the known blurring operator matrix and  $\mathbf{n}$  the measurement noise. If  $\mathbf{h}$  is the impulse response of the imaging acquisition system then  $\mathbf{H}$  is the block circular convolutional matrix built with  $\mathbf{h}$ . The measurement noise  $\mathbf{n}$  is here considered white gaussian.

Since in general  $\mathbf{h}$  is a band-limited function and due to presence of observation noise  $\mathbf{n}$ , deconvolution, i.e. the estimation of  $\mathbf{x}$  from the observation of  $\mathbf{y}$ , is an ill-posed problem and its solution is not unique. A stable and unique inverse solution can be obtained by

imposing additional regularization constraints on the inverse solution. The basic ideas of regularization consist of considering a family of approximate solution depending on one or more positive parameters, called regularization parameters, which results in the minimization of a suitable functional  $\phi$

$$\hat{\mathbf{x}} = \min_{\mathbf{x}} \phi(\mathbf{x}, \mathbf{y}, \bar{\lambda}) \quad (4.3)$$

where  $\bar{\lambda}$  is the regularization parameters vector.

The main property of this approach is that, in the case of noise-free observation, the family of solutions converge to the exact solution, even for a non-zero value of the regularization parameters.

#### 4.2.1 Estimation of system PSF

Different techniques are available to perform the PSF estimation: a common method for measuring  $\mathbf{h}$  is the insonification of a metal wire sank in a water filled tank. However, since in general the system PSF is a shift-variant function, this technique gives only a good estimation of the PSF in the focal zone. Moreover, due to aberration and phase distortion caused by the propagation inside the tissue, the real PSF is different and should be estimated from the observed signal.

Minimum phase PSF can be easily estimated from the observed signal by means of homomorphic blind deconvolution techniques [13][22], which employ denoising method in signal cepstrum domain for pulse recovery.

Non-minimum phase PSFs can be theoretically recovered estimating the phase from the observed signal by means of phase unwrapping algorithms [20][22]. However, these technique have been proved to be an ill-posed, and their performance are very sensitive to noise and therefore, unreliable.

Therefore, in order to have a controllable setup, in this investigation in all the simulations on synthetic signals the system PSF is assumed to be a known non-minimum phase pulse, while on real in vivo ultrasound images only the minimum phase version of the PSF estimated with the method presented in [22] is used, leaving as future development the characterization of deconvolution algorithm to not perfect knowledge of system PSF.

#### 4.2.2 Statistical approach to regularized inversion

In a statistical framework regularization is imposed by seeking the solution  $\hat{\mathbf{x}}$  which maximize functional based on a stochastic model of the acquired signal and of the observation noise. Such approach is related to statistical estimation theory [16]. Two main approaches are here considered: the Maximum Likelihood (ML) estimation and the Maximum a Posteriori (MAP).

##### Maximum Likelihood

In the maximum likelihood (ML) approach, the solution is found minimizing

$$\hat{\mathbf{x}}_{\text{ML}} = \max_{\mathbf{x}} \{\log p(\mathbf{y}|\mathbf{x})\} = \min_{\mathbf{x}} \{-\log p(\mathbf{y}|\mathbf{x})\} \quad (4.4)$$

being  $p(\mathbf{y}|\mathbf{x})$  the probability of the observation given the data, i.e. the likelihood.

Since we assumed an additive noise model we can write:

$$p(\mathbf{y}|\mathbf{x}) = p_n(\mathbf{y} - \mathbf{H}\mathbf{x}) \quad (4.5)$$

and since the noise is assumed white gaussian

$$p_n(\mathbf{n}) = \frac{1}{(2\pi\sigma_n^2)^{N/2}} e^{-\frac{1}{2\sigma_n^2}\mathbf{n}^T\mathbf{n}} \quad (4.6)$$

where  $\sigma_n$  is the noise standard deviation and  $N$  is the number of samples, the likelihood function can be written as

$$p(\mathbf{y}|\mathbf{x}) = \frac{1}{(2\pi\sigma_n^2)^{N/2}} e^{-\frac{1}{2\sigma_n^2}(\mathbf{y}-\mathbf{H}\mathbf{x})^T(\mathbf{y}-\mathbf{H}\mathbf{x})} \quad (4.7)$$

and substituting in eq. (4.4) becomes:

$$\hat{\mathbf{x}} = \min_{\mathbf{x}} (\mathbf{y} - \mathbf{H}\mathbf{x})^T (\mathbf{y} - \mathbf{H}\mathbf{x}) = \min_{\mathbf{x}} \|\mathbf{y} - \mathbf{H}\mathbf{x}\|^2. \quad (4.8)$$

where  $\|\cdot\|$  is the  $L^2$ -norm. From eq.(4.8) it clear that ML solution equals the minimum  $L^2$ -norm solution of the problem (4.2). Since:

$$(\mathbf{y} - \mathbf{H}\mathbf{x})^T (\mathbf{y} - \mathbf{H}\mathbf{x}) = \mathbf{y}^T \mathbf{y} - 2\mathbf{x}^T \mathbf{H}^T \mathbf{y} + \mathbf{x}^T \mathbf{H}^T \mathbf{H} \mathbf{x} \quad (4.9)$$

and the term  $\mathbf{y}^T \mathbf{y}$  does not depend on  $\mathbf{x}$ , we can rewrite eq.(4.8) as:

$$\hat{\mathbf{x}} = \min_{\mathbf{x}} \{-2\mathbf{x}^T \mathbf{H}^T \mathbf{y} + \mathbf{x}^T \mathbf{H}^T \mathbf{H} \mathbf{x}\} \quad (4.10)$$

differentiating with respect to  $\mathbf{x}$ , and reminding that

$$\frac{\partial}{\partial \mathbf{x}} \mathbf{x}^T \mathbf{a} = \mathbf{a} \quad (4.11)$$

$$\frac{\partial}{\partial \mathbf{x}} \mathbf{x}^T \mathbf{W} \mathbf{x} = (\mathbf{W} + \mathbf{W}^T) \mathbf{x} \quad (4.12)$$

we find

$$\mathbf{H}^T \mathbf{H} \hat{\mathbf{x}} = \mathbf{H}^T \mathbf{y} \quad (4.13)$$

i.e.

$$\hat{\mathbf{x}}_{\text{ML}} = (\mathbf{H}^T \mathbf{H})^{-1} \mathbf{H}^T \mathbf{y} \quad (4.14)$$

where  $\mathbf{A} = (\mathbf{H}^T \mathbf{H})^{-1} \mathbf{H}^T$  is the pseudo-inverse of  $\mathbf{H}$ , which coincides with  $\mathbf{H}^{-1}$  when  $\mathbf{H}$  is square and full rank.

### Maximum a Posteriori

When no assumptions can be made on the true signal, the ML estimate assures the best results. Otherwise, it is a fundamental rule of estimation theory that the use of prior knowledge on the data will lead to a more accurate estimator [16].

We define the MAP estimate as:

$$\hat{\mathbf{x}}_{\text{MAP}} = \arg \max_{\mathbf{x}} \{\log(p(\mathbf{x}|\mathbf{y}))\} \quad (4.15)$$

where  $p(\mathbf{x}|\mathbf{y})$  is the probability of the true data given the observation. Keeping in mind the Bayes rule:

$$p(\mathbf{y}, \mathbf{x}) = p(\mathbf{x}|\mathbf{y})p(\mathbf{y}) = p(\mathbf{y}|\mathbf{x})p(\mathbf{x}) \quad (4.16)$$

and noting that  $p(\mathbf{y})$  does not depend on  $\mathbf{x}$ , we can rewrite (4.15) as

$$\hat{\mathbf{x}} = \arg \max_{\mathbf{x}} \{\log(p(\mathbf{y}, \mathbf{x}))\} = \max_{\mathbf{x}} \{\log(p(\mathbf{y}|\mathbf{x})) + \log(p(\mathbf{x}))\} \quad (4.17)$$

Reminding (4.5) we can rewrite the MAP solution as

$$\hat{\mathbf{x}}_{\text{MAP}} = \arg \min_{\mathbf{x}} \{ \|\mathbf{y} - \mathbf{H}\mathbf{x}\|^2 - 2\sigma_n^2 \log p(\mathbf{x}) \} \quad (4.18)$$

Equation (4.18) is the starting point of many image restoration problems, which differ from each other in the choice of the penalty  $p(\mathbf{x})$ . At this point it worth saying that if MAP is better performing than ML, minimizing (4.18) could be a non trivial task for two main reasons: first of all the functional to be minimized, a part from few cases, does not have a closed form solution, and sometimes can be non-convex; second, since the matrix  $\mathbf{H}^T\mathbf{H}$  in (4.9) is non diagonal, the problem is not separable, that is on the contrary the case of denoising problems.

Now, the MAP estimator for some notable cases will be derived. Suppose  $x$  is an i.i.d. process, i.e. we can write

$$p(\mathbf{x}) = \prod_{i=1}^N p(x_i) \quad (4.19)$$

and substituting in (4.18) the MAP estimator becomes

$$\hat{\mathbf{x}}_{\text{MAP}} = \arg \min_{\mathbf{x}} \{ \|\mathbf{y} - \mathbf{H}\mathbf{x}\|^2 - 2\sigma_n^2 \sum_{i=1}^N \ln p(x_i) \} \quad (4.20)$$

**Gaussian Distribution.** Suppose that  $x$  follows a Gaussian distribution

$$p(x|\mu, \sigma_x^2) = \frac{1}{\sqrt{2\pi}\sigma_x} \cdot e^{-\frac{(x-\mu)^2}{\sigma_x^2}}. \quad (4.21)$$

Thanks to the i.i.d hypothesis the LL function becomes

$$\hat{\mathbf{x}}_{\text{MAP}} = \arg \min_{\mathbf{x}} \{ \|\mathbf{y} - \mathbf{H}\mathbf{x}\|^2 + \frac{2\sigma_n^2}{\sigma_x^2} \sum_{i=1}^N (x_i - \mu)^2 \} \quad (4.22)$$

which is the well-known Wiener filter. For Gaussian distributed data, the MAP estimator is therefore equivalent to the Tikhonov regularization. Although this estimator is simple and generally succeed to enhance the visual quality of US images, in presence of edges and coherent scatters the estimation often produces ringing effects or over-smooths the reflectivity function.

**Laplacian Distribution** Suppose now that  $x$  follows a Laplacian distribution

$$p(x|\mu, \lambda) = \frac{1}{\lambda} \cdot e^{-\frac{|x-\mu|}{\lambda}} \quad (4.23)$$

where the variance is  $\sigma^2 = 2 * \lambda^2$ . Then the MAP estimator becomes

$$\hat{\mathbf{x}}_{\text{MAP}} = \arg \min_{\mathbf{x}} \{ \|\mathbf{y} - \mathbf{H}\mathbf{x}\|^2 + \frac{2\sigma_n^2}{\lambda} \sum_{i=1}^N |x_i - \mu| \} \quad (4.24)$$

which corresponds to the  $L^1$ -norm regularization of the solution. Such model, proposed for modelling the tissue reflectivity in [22], permits a better recovery of the stronger reflectors at structural boundaries. The main drawback of this model is that it provides sparse solutions even where the real tissue reflectivity it is not sparse [27].

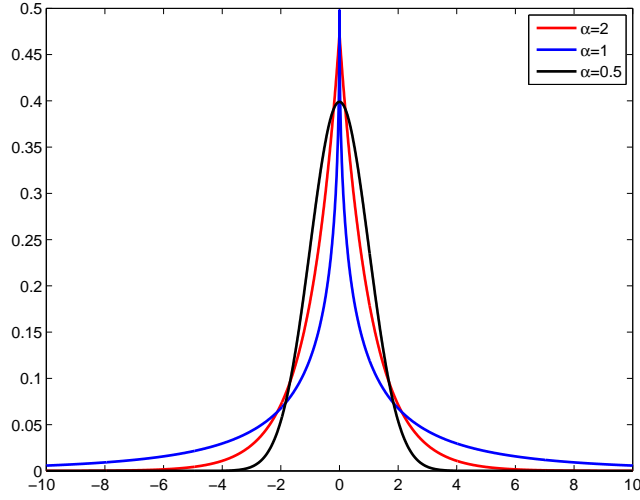


Figure 4.1: Generalized gaussian distribution

**Generalized Gaussian Distribution** Suppose now that  $x$  follows a Generalized Gaussian distribution

$$p(x|\mu, \sigma, \alpha) = a \cdot e^{-\frac{|x-\mu|}{b}^\alpha} \quad (4.25)$$

where  $\mu$  is the mean value,  $\sigma$  is the standard deviation and  $\alpha$  is the shape parameter. The parameters are defined as

$$a = \frac{1}{2\Gamma(1 + \frac{1}{\alpha})b} \quad b = \sigma \sqrt{\frac{\Gamma(\frac{1}{\alpha})}{\Gamma(\frac{3}{\alpha})}}. \quad (4.26)$$

Generalized Gaussian distribution can easily fit the statistics of a wide set of signal observed in real contexts. Changing the value of the shape parameter  $\alpha$  a family of heavy-tailed distribution can be defined (see fig.4.1). Moreover, for  $\alpha = 1$  the GGD becomes a Laplacian distribution, while for  $\alpha = 2$  becomes a Gaussian.

For a GGD distribution the MAP estimator becomes

$$\hat{x}_{\text{MAP}} = \arg \min_x \|\mathbf{y} - \mathbf{H}\mathbf{x}\|^2 + 2\sigma_n^2 \sum_{i=1}^N \left| \frac{x_i - \mu}{b} \right|^\alpha. \quad (4.27)$$

The main drawback of GGD modeling is that the estimator (4.27) has no closed form solution, due to the non quadratic expression of the regularization, and for some values of  $\alpha$  it constitutes a non-convex optimization problem. Therefore, iterative minimization algorithms must be used. In the following section a stochastic model for the observed signal  $\mathbf{y}$  and an approach for the minimization of the MAP estimator will be presented.

### 4.2.3 US radio frequency signal model

Although the GGD can fit a wide class of signals, a simple stationary model is not suitable for the high non stationary statistic exhibited by biological tissues. As proposed in [27],

the impedance of soft tissues varies macroscopically in a piecewise-smooth way, but locally the reflectivity exhibit a pseudo-random fast variation. These assumptions can be justified by considering the physical interaction between the ultrasonic field and the propagation medium. As reviewed in chapter 1, all the structure characterized by spatial variation of the acoustical parameters that are big if compared to the ultrasonic field wavelength generates coherent reflections. The intensity of this component of the reflected field is typically piecewise smooth and can be assumed as an estimation of the macroscopic profile of tissues reflectivity. On the contrary, all the spatial variation that are smaller than the wavelength of the incident radiation give raise to scattering phenomena and therefore to non-coherent reflections. The intensity of this component of the reflected field is typically rapidly varying and is not directly related to the microscopic profile of tissue reflectivity.

Such consideration can be translated modeling the tissue reflectivity  $\mathbf{x}$  as

$$\mathbf{x} = \mathbf{\Sigma}\mathbf{s} \quad (4.28)$$

where  $\mathbf{s}$  is a  $N \times 1$  vector of generalized Gaussian distributed samples with unitary variance and  $\mathbf{\Sigma}$  is a  $N \times N$  diagonal matrix containing the echogenicity profile  $\bar{\sigma} = \{\sigma_0, \dots, \sigma_N\}$  which is a piecewise smooth sequence. Although the model is formulated as 1D, it can be easily extend to 2D or 3D without loss of generality rearranging multi-dimensional signals into 1D equivalents by lexicographical orders, as explained in [5].

Substituting 4.28, the observed signal model becomes:

$$\mathbf{z} = \mathbf{H}\mathbf{\Sigma}\mathbf{s} + \mathbf{n} = \mathbf{u} + \mathbf{n} \quad (4.29)$$

The proposed model has two parameters: the echogenicity (or variance) profile and the shape parameter. While echogenicity profile  $\bar{\sigma}$  can be used for modelling signal dynamic, the shape parameter can be used for adjusting signal sparseness, i.e. for modelling different scatters densities. As shown in fig. 4.3, starting from the same echogenicity profile, different levels of reflectivity sparseness can be obtained varying the shape parameters. Such feature can be exploited in two different way: as a fixed a priori value, for obtaining a desired level of solutions sparseness; as an unknown parameter to be estimated, for characterizing the tissue properties in terms of first order statistic.

The two possible interpretations of the proposed model leads to two different type of algorithms with different complexity: while the first require the minimization of the functional (4.27) with respect to  $\mathbf{x}$ , the latter theoretically require a joint maximization with respect to  $\mathbf{x}$  and  $\alpha$ . While for pure image processing purposes the first approach can lead to satisfactory results, in the context of ultrasonic tissue characterization preserving and enhancing the information contained in signal statistic is fundamental. However, although the tissue characterization point of view as adaptive approach should lead in general to better results, if low computational complexity is demanded the first solution can be preferable.

In the following sections, the application of the proposed model for image quality enhancement will be presented, leaving the development of tissue characterization techniques as future development.

### 4.3 Viterbi algorithm based deconvolution

As reviewed in chapter 1, one of the main advantages of ultrasound imaging versus the other imaging techniques is its real-time nature. Thus, all signal processing techniques

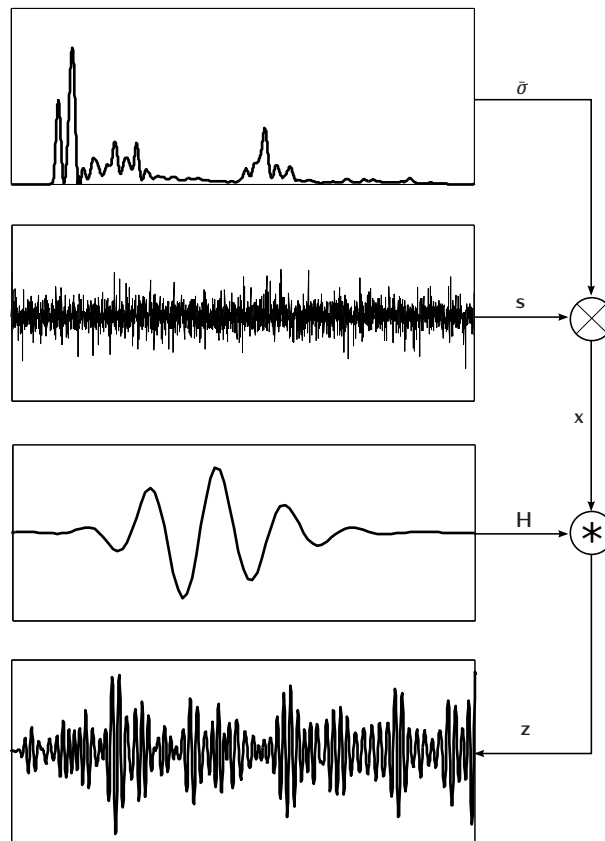


Figure 4.2: Schematic representation of the proposed signal model. From top to bottom: tissue echogenicity, diffused component, system PSf and RF signal. (pictures not in scale)

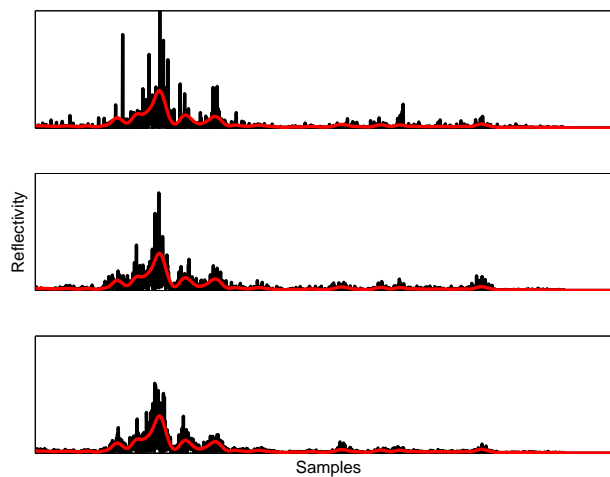


Figure 4.3: Example of piecewise smooth tissue echogenicity (red curve) and magnitude of tissue reflectivity generated with the proposed model (4.28), for different values of the shape parameter:  $\alpha=0.5$  (top),  $\alpha=1$  (center)  $\alpha=2$  (bottom).

that aim to improve image quality, and therefore also deconvolution algorithms, should in general preserve this important feature. Unfortunately, deconvolution of ultrasound signals is in general an hard task that require computationally expensive techniques often far from real-time applications. Therefore, in this section we will develop a novel deconvolution technique aiming to an affordable computational cost.

In modern digital ultrasound imaging systems the measured RF signal is quantized, usually with a 12-14 bit resolution for RF signal. Such high resolution is necessary because of the high dynamical range of ultrasound signals, due to tissue attenuation (see chapter 1 for further details), for performing with high accuracy the bearing and finally for preserving the information contained in the signal. However, for imaging purposes the required resolution is lower: after the envelope detection and log compression the signal envelope is usually quantized with a resolution of 8-bit, which corresponds to 256 levels of gray, i.e. the maximum contrast that human eyes can detect [10].

This operative condition can be exploited for modeling the tissue reflectivity sample  $x_l$  as a discrete value random process distributed on a finite alphabet of size  $\mathcal{X} = \{x^1, \dots, x^K\}$ , where  $K$  is the size of the alphabet. Thus, the blurred tissue reflectivity sequence  $\mathbf{u} = \mathbf{H}\mathbf{x}$  can be thought as the output of a finite-state discrete-time Markov random process, with finite state space of dimension  $J$ . For a shift-invariant system PSF of length  $L$  and a tissue reflectivity alphabet  $\mathcal{X}$  of size  $K$ , the Markov random process associated to the blurred reflectivity sample has therefore  $J = K^{L-1}$  possible states defined by

$$u_i = \sum_{j=1}^L h_j x_{i-j}. \quad (4.30)$$

The problem of recovering tissue reflectivity is therefore equivalent to the problem of detecting symbols affect by noise and intersymbol interference [8]. Similar approaches were proposed in literature in the context of image restoration [30][24] and deconvolution of Bernoulli Gaussian processes [7].

Since eq.(4.30) creates a one by one correspondence between the reflectivity samples sequences and the states of the Markov process we can write

$$u_i \equiv (x_{i-1}, \dots, x_{i-L}). \quad (4.31)$$

The MAP estimation of the tissue reflectivity  $\mathbf{x}$  is therefore equivalent to the MAP estimation of the process states sequence  $\mathbf{u}$ . For finite-state discrete-time Markov random process in memoryless noise the density  $p(\mathbf{y}, \mathbf{u})$  can be written as:

$$p(\mathbf{y}, \mathbf{u}) = p(\mathbf{y}|\mathbf{u})p(\mathbf{u}) = \prod_{i=1}^N p(y_i|u_{i+1}, u_i)p(u_{i+1}|u_i) \quad (4.32)$$

and defining the transition metric

$$\gamma(u_{i+1}, u_i) \triangleq -\ln p(y_i|u_{i+1}, u_i) - \ln p(u_{i+1}|u_i) \quad (4.33)$$

we can write

$$-\ln p(\mathbf{y}, \mathbf{u}) = \sum_{i=1}^N \gamma(u_{i+1}, u_i). \quad (4.34)$$

Eq. (4.34) shows that the probability of having a states sequence  $\mathbf{u}$  given the observed sequence  $\mathbf{y}$  is equivalent to the probability length of a path inside a random graph. Thus,

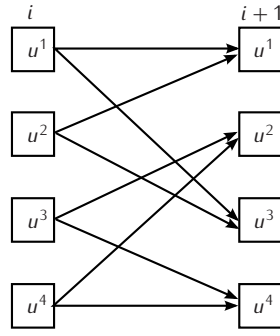


**Figure 4.4:** Example of trellis diagram of a Markov process with four states  $u^1 = \{x^1, x^1\}$ ,  $u^2 = \{x^1, x^2\}$ ,  $u^3 = \{x^2, x^1\}$ ,  $u^4 = \{x^2, x^2\}$ . Such diagram correspond to a blurring operator of length 2 applied on sequences of symbols with cardinality 2.

the MAP estimation of the states sequence  $\mathbf{u}$  corresponds to find the shortest path in a graph with branches weighted by the metric (4.33). This problem is known to be optimally solved with a low computational cost by Viterbi algorithm (VA) [8].

For the proposed signal model, eq. (4.33) can be rewritten as:

$$\gamma(u_{i+1}, u_i) \triangleq \left[ y_i - \sum_{j=1}^L h_j x_{i-j} \right]^2 + 2\sigma_n^2 \left| \frac{x_i}{\sigma_i} \right|^\alpha \quad (4.35)$$

### 4.3.1 Viterbi algorithm

Viterbi algorithm was proposed in 1967 as a method of decoding convolutional codes. Since that time, it has been recognized as an attractive solution to a variety of discrete estimation problems, somewhat as the Kalman filter has been adapted to a variety of continuous estimation problems. In its most general form the VA can be viewed as a solution to the problem of MAP estimation of the finite-state discrete-time Markov process observed in memoryless noise.

Through VA, the shortest path that minimize (4.34) is computed in a recursive manner over the trellis-diagram [8] associated to the process. The trellis-diagram is a graphic way to represent a finite-state process in a redundant form: states, transitions and sequences are represented by means of nodes, branches and paths. Such diagram shows all the possible transitions from and to each state  $u^j$  at step  $i$  and can recursively generate all the possible state-sequences of a certain length  $N$ . Since each states sequence is in fact associated to a unique path inside the trellis, VA will then estimate the MAP state-sequence  $\hat{\mathbf{u}}$  by recursively generating all the possible paths of length  $N$ , discarding the concurrent ones by considering their distances from the observed sequence  $\mathbf{y}$ , computed by means of the eq.(4.33). Finally, the minimum distance path will be chosen as the estimated sequence. An example of trellis diagram associated to a finite-state Markov process is shown in figure 4.4: at step  $i$ , each state  $u^j$  is connected with only  $K$  states at step  $i + 1$ .

The drawback of this procedure is that even for not so large values of  $K$  and  $L$ , the VA becomes already impractical, since its computational and memory demands is proportional to  $N \cdot K^{L-1}$ . Thus, for real-time biomedical image processing application, a computational cost reduction is mandatory.

### 4.3.2 Computational cost reduction

Several modifications have been proposed to reduce VA memory-requirement, such as purging unnecessary states [35], truncation of memory length [9], and merging of states [12]. Most of these methods exploit the systematic structure of information coding or prior information about noise level for reducing the number states necessary for optimal decoding.

While in digital communication data is assumed to be uncorrelated, in the context of tissue reflectivity signal correlation can be exploited for reducing the number of algorithm states. In the proposed model, signal correlation is due to the piecewise smooth trend of the echogenicity map  $\bar{\sigma}$ . Since  $\bar{\sigma}$  is a piecewise smooth function, adjacent samples are highly correlated and therefore a reduced number of states is demanded for estimating the true tissue reflectivity.

Thus, it is reasonable to assume that not all the states are important and that the unpromising survivors possessing small weights can be omitted with small probability of discarding the best path. For these motivations, in this work we adopted a reduced states VA based on the M-algorithm [4]. In M-algorithm only  $M$  survivor paths inside the trellis are kept at each algorithm step  $i$ . These path are selected among all the possible candidates by means of their distance from the observed partial sequence  $\mathbf{y}_i = \{y_1, \dots, y_n\}$ . M-algorithm can be summarized with the following steps:

1. Forward from the root state, repeat the loop 2) - 4).
2. Extend all the paths form level  $i - 1$  to level  $i$ .
3. Keep the  $M$  paths closest to  $\mathbf{y}_i = \{y_1, \dots, y_n\}$  and discard the others;
4. Stop criteria: if all the paths are in the same subset go to 5) else go to 2;
5. Release as output the first branch, delete all paths in storage, and set a new root node equal to the end node of the released path.

While Viterbi algorithm can be considered as multiple-list single-survivor algorithm, M-algorithm is a single list multiple survivor algorithm. The number of survivor  $M$  is related to power of the noise  $\mathbf{n}$  that affect the observed signal  $\mathbf{a}_n$  to the length  $L$  of the system PSF : the stronger the noise power and the longer the PSF, the larger the number of required survivors must be in order to obtain satisfactory results.

**Adaptive codebook.** Signal correlation can be also exploited for adapting the alphabet  $\mathcal{X}$  to signal dynamic and reduce the distortion introduced by signal quantization. Ultrasound signals are in fact characterized by a big amplitude dynamic. However the statistical distribution of signal amplitude is highly non uniform, due to the amplitude variations in time introduced by the echogenicity component. In the proposed model, such variation is modelled through the echogenicity map  $\bar{\sigma}$ .

At each time step  $i$ , the signal distribution is therefore generalized Gaussian with variance  $\sigma_i^2$ . From source coding theory is noted that, if signal statistic is known, the minimum mean square error quantization is obtained by using an non uniform quantization alphabet

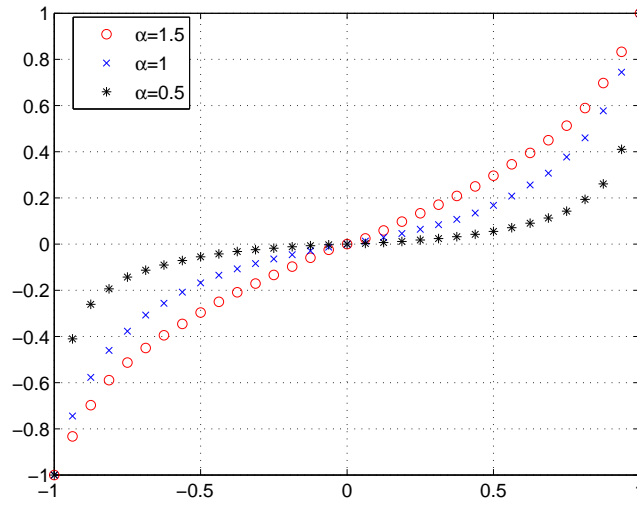


Figure 4.5: Example of codebooks with 33 level of quantization obtained with Lloyd-Max rules for different values of shape parameters.

computed with Loyd Max rules [1]:

$$t^j = \frac{x^j + x^{j-1}}{2}$$

$$\int_{t^j}^{t^{j+1}} (x - x^j) p(x) dx = 0 \quad (4.36)$$

$$j = 1, \dots, M$$

where  $x^j$  are the codebook symbols and  $t^j$  the quantization thresholds. Once the number of desired quantization level has been fixed, the shape parameter  $\alpha$  of the GGD is the only factor that determines the codebook structure, and in particular it is directly related to its non-uniformity, as shown in fig. 4.5.

Thus, the minimum distortion codebook can be pre-computed for a generalized Gaussian source with variance  $\sigma = 1$  and at each time step  $i$  it is shrunk or expanded in order to keep the probability that the true tissue reflectivity can be greater than the maximum codebook value smaller than the 0.1%. This procedure can be intuitively interpreted as an adaptive selection of the quantization levels, with respect to the finest quantization grid defined by the system A/D converter, as shown in fig. 4.6, or more theoretically speaking as an adaptive scalar quantization. Thanks to the codebook adaptivity, if the number of adopted symbols is big enough, the distortion introduced is visually negligible, even when the signal reach the maximum amplitude.

A correct estimation of the echogenicity is therefore fundamental for distortion minimization and algorithm stability. However, a smoothed estimation of the echogenicity map  $\bar{\sigma}$  can be obtained by low pass filtering the envelope of the observed signal  $z$  or it wiener filtered version.

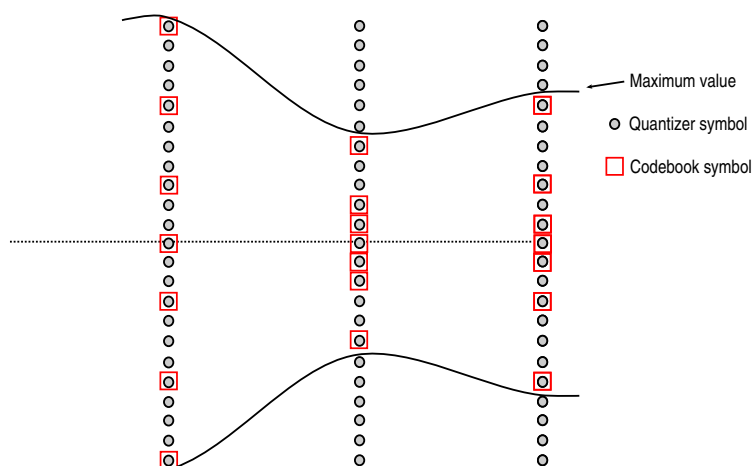


**Figure 4.6:** Interpretation of the adaptive codebook as adaptive subset of the quantizer levels.

#### 4.4 Algorithm performance

In order to assess the effect of the different parameters on algorithm performance, we performed several tests on synthetic signals generated according to the proposed model, and on real signals recorded with a commercial ultrasound imaging equipment. The parameters of the proposed procedure to be tuned are:

- the number of survived states  $M$ ;
- the codebook size  $K$ ;
- the codebook shape parameter  $\alpha$ .

The number of survived states  $M$  is a critical parameter that determines the stability of the algorithm against noise: if  $M$  is too small, the algorithm becomes unstable. As shown in fig. 4.7, increasing  $M$  the algorithm becomes stable and its performance, evaluated in terms of improvement in signal to noise ratio in decibels:

$$ISNR = 20 \log_{10} \left( \frac{\|\mathbf{y} - \mathbf{x}\|}{\|\hat{\mathbf{x}} - \mathbf{x}\|} \right). \quad (4.37)$$

increase. From the results obtained on synthetic signals we verified that a minimum number of  $K = 200$  survivors is sufficient to have stability for signal with an average SNR  $> 20$  dB, while no significant ISNR improvement can be obtained for  $K > 2000$ .

Similar considerations can be drawn for the alphabet size  $K$ : if only few symbols are used, especially when the signal dynamic is big the distortion introduced by the quantization becomes unacceptable. A good balance between distortion and computational cost can be obtained with codebook size that ranges from 33 to 129 symbols.

While the number of survivors  $M$  and the codebook size  $K$  are tuned in order to have algorithm stability, limit the distortion introduced by the quantization and achieve an affordable computational cost, the shape parameter plays a fundamental role in governing solution regularization and in particular its sparseness and robustness against noise. As shown in fig. 4.8, decreasing the shape parameter, the solution becomes sparser and while

where the signal is smaller and highly corrupted by noise, a noise suppression effect is noted, where the signal to noise ratio is higher the solution is closer to the original signal.

Finally, a comparison between inverse filter, Wiener filter and reduced complexity Viterbi deconvolution has been performed. As shown in fig. 5.11, while the solution provided by inverse filter is unstable and Wiener filter provides a stable solution but the estimated tissue reflectivity is over-smoothed, reduced complexity Viterbi deconvolution provide a stable solution that preserve the sparse nature of the tissue reflectivity. A further proof of the superior performance of the proposed method with respect to the Wiener filter can be evaluated comparing the power and phase spectrum of the tissue reflective estimated by the two methods, shown in fig. 4.10 and 4.11. While Wiener filter is able to recover the signal spectrum only in where the signal to noise ratio is higher than the regularization parameter and phase spectrum is wrongly estimated, the proposed method is able to equalize signal power spectrum also in the frequency band where the signal to noise ratio is low and a good recovery of phase spectrum is obtained.

To verify the effectiveness of the proposed algorithm as a de-blurring method for ultrasound images we tested it on an US signals database which comprises synthetic phantom (CIRS Model 047) acquisitions and *in-vivo* TRUS acquisitions of prostate glands (264 frames), both obtained with a commercial ultrasound equipment (MYLAB90 Esaote S.p.a.). The minimum phase version of PSF  $h$  was obtained with the homomorphic based deconvolution procedure mentioned in section 4.2.1.

All signals were processed column-wise with the settings obtained on synthetic signals. Figures 4.12 compare to the original B-Mode images (figure 4.12(a)) the visual quality of images processed with Wiener filter (figure 4.12(b)) and with MAP estimation (figure 4.12(c)); as it can be seen, resolution and contrast in the images processed with the proposed method are much better than in the original ones and Wiener filtered one.

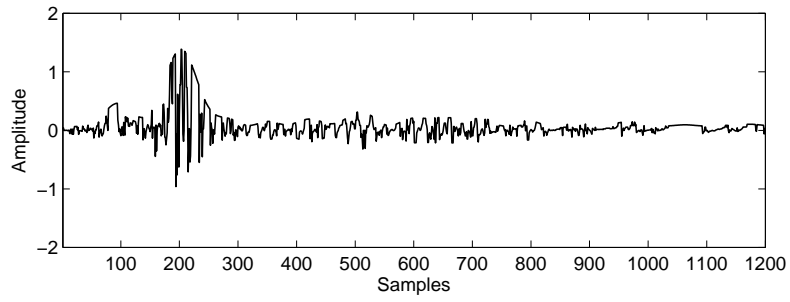
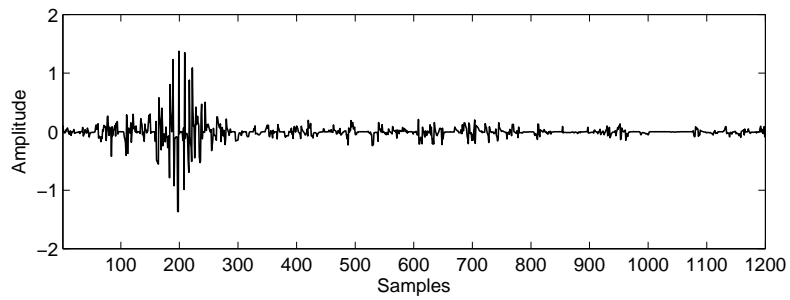
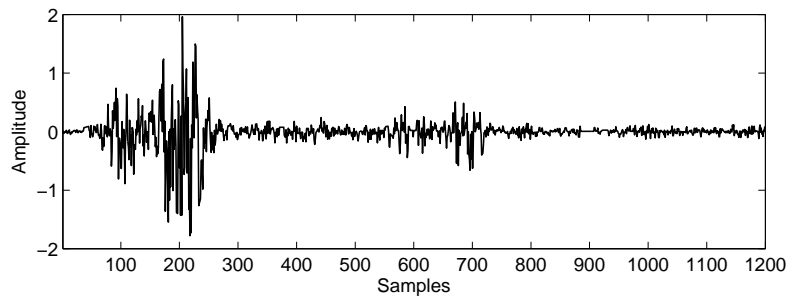
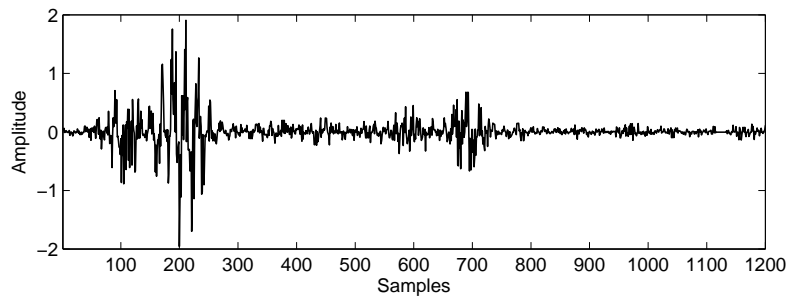
Algorithm performance was also qualitatively evaluated in terms of signal resolution improvement and image quality enhancement. To quantify the resolution improvement we measured the resolution gain at -6dB (RG-L/A) along the deconvolution direction [2]; the Peak Signal to Noise Ratio (PSNR) and the Structural Similarity Index (SSIN) were used to compute the dissimilarity between the original and processed image, in terms of loss of correlation, luminance distortion and contrast distortion [18]; finally we measured the image contrast enhancement on phantoms by means of the Contrast Gain (CG) [31].

For *in-vivo* and phantom RF signals processing, the average results over the whole datasets obtained with the estimated system response are shown in table 4.1(a) and table 4.1(b), respectively. As it can be clearly seen, the proposed algorithm provides a good resolution increase for both *in-vivo* and phantom acquisitions, with better performance on the *in-vivo* frames. The images SSIN is quite close to the maximum value of 1, with better performance on *in-vivo* frames.

Finally, we compared algorithm performance to Wiener filter and an publicly available deconvolution algorithms in literature presented in [25]. As shown by the results in Table 4.1(a) and 4.1(b), the proposed algorithm outperforms both of them with respect to the proposed metric.

## 4.5 Discussion

The goal of the research presented in this chapter was the development of deconvolution algorithm for resolution rapprochement of ultrasound imaging system signals. The function

(a)  $M = 50$  - unstable(b)  $M = 100$  - unstable(c)  $M = 1000$  -  $\text{ISNR} = 1.5$  dB(d)  $M = 2000$   $\text{ISNR} = 2.1$  dB

**Figure 4.7:** Comparison of the deconvolution of a synthetic signal for different numbers of survived paths.

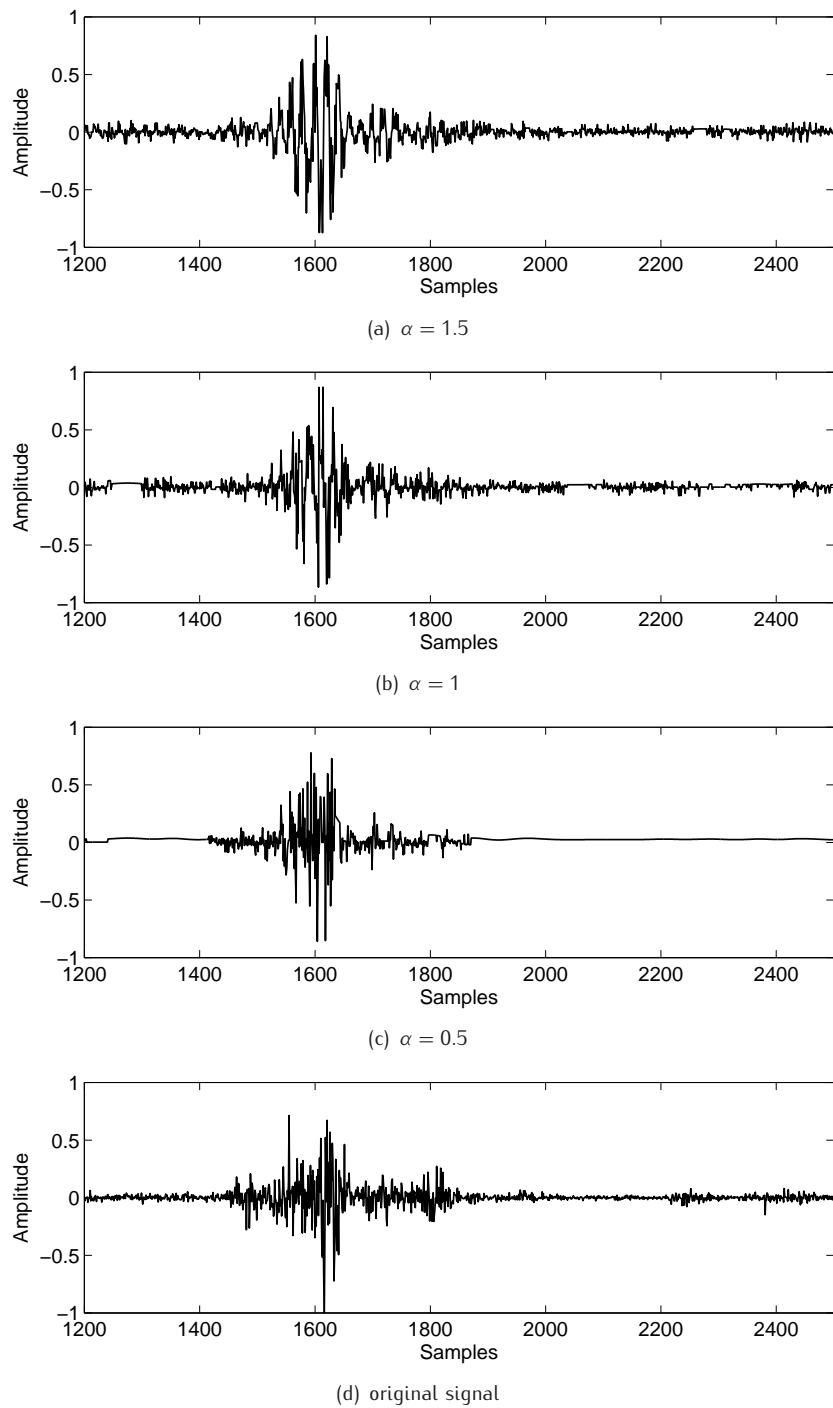
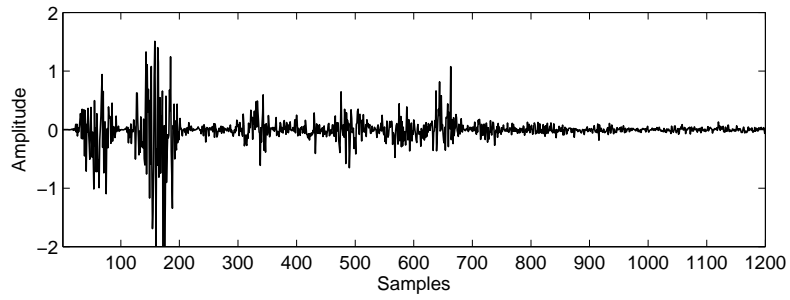
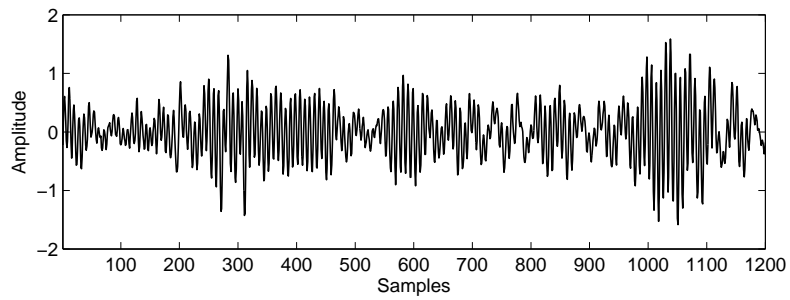


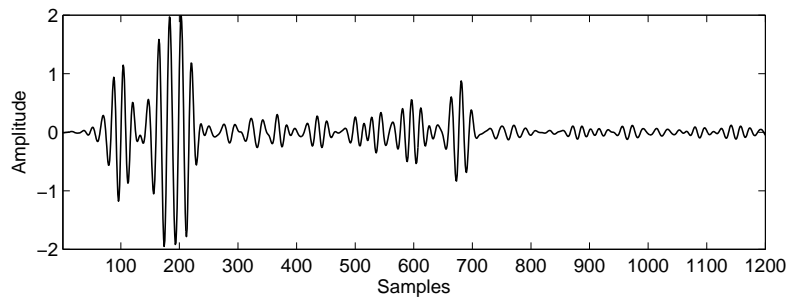
**Figure 4.8:** Comparison of the deconvolution of a synthetic signal for different level of sparsity  $\alpha$ .



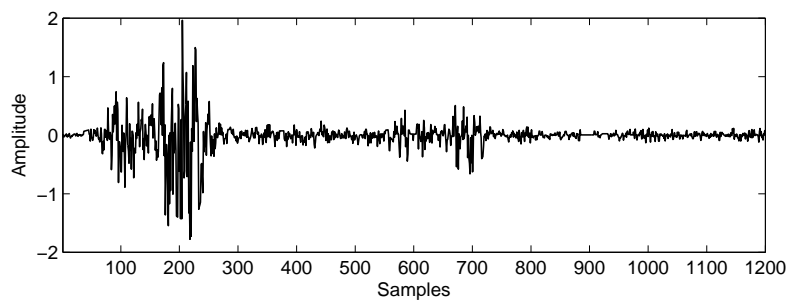
(a) original tissue reflectivity



(b) inverse filter

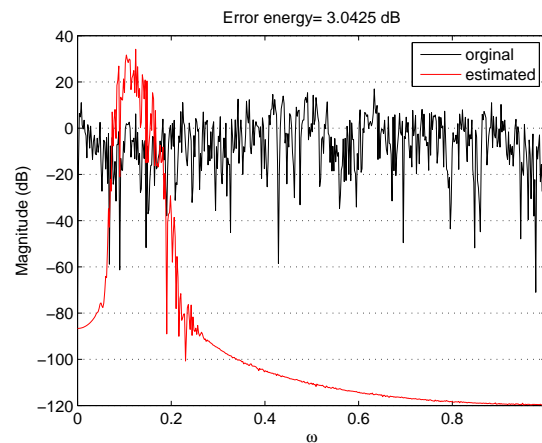


(c) wiener estimation

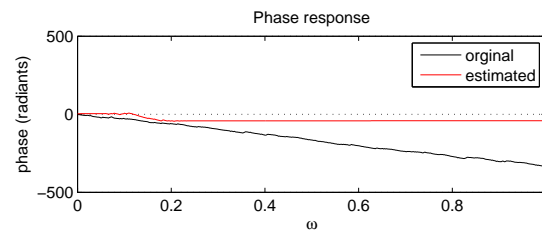


(d) reduced complexity viterbi estimation

**Figure 4.9:** Comparison of the deconvolution of a synthetic signal generated according to the proposed model with inverse filter (a), wiener filter and reduced complexity Viterbi algorithm (c).



(a) power spectrum



(b) phase spectrum

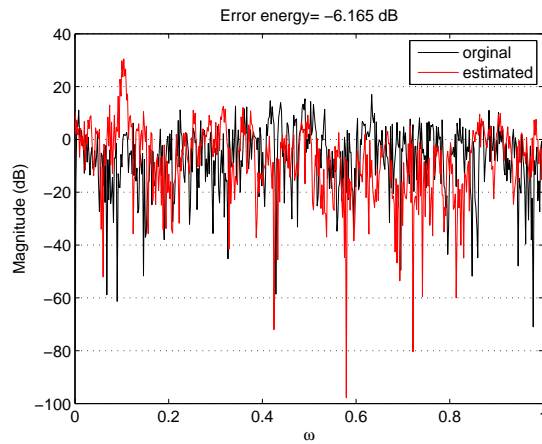
**Figure 4.10:** Comparison between power and phase spectrum of the original tissue reflectivity and Wiener filter estimation.

of the proposed method is increasing the resolution of echo graphic imaging system which is limited by the finite bandwidth of the piezoelectric elements of the imaging probe. Signal deconvolution is a challenging problem: due to the observation noise and the band-limited nature of system PSF, the estimation of the true tissue reflectivity is an ill-posed problem and regularized inversion techniques are therefore necessary.

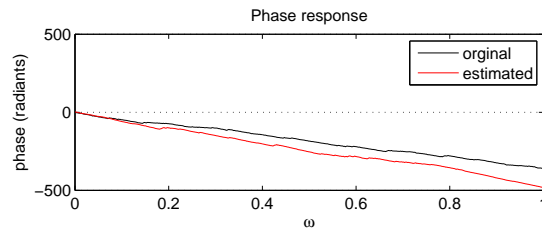
After a complete review of the ultrasound signal deconvolution techniques presented in literature, a statistical framework and a novel stochastic signal model is proposed. The deconvolution procedure is based on two steps: system point spread function estimation and tissue reflectivity deconvolution.

System PSF is estimated through blind homomorphic deconvolution techniques presented in literature. In order to avoid instability caused by phase unwrapping algorithm for phase estimation, only the minimum phase version of system PSF is taken into account.

The proposed tissue reflectivity deconvolution is developed in a statistical framework and it is formulated as a MAP estimation problem. A prior model of the observed signal is



(a) power spectrum



(b) phase spectrum

**Figure 4.11:** Comparison between power (a) and phase 4.11(b) spectrum of the original tissue reflectivity and reduced complexity Viterbi estimation.

used for imposing solution regularization: the unknown tissue reflectivity is modelled as the product between a piecewise-smooth function, i.e. tissue echogenicity, and a generalized Gaussian random process. The shape parameter of the generalized Gaussian distribution can be used for controlling the sparsity of the solution and thus its regularization. This model leads to two possible type of application: image enhancement or tissue characterization.

The MAP estimator for the proposed model requires the minimization of a non convex function and thus, iterative methods are required. Although these methods can provide satisfactory performance in terms accuracy, their computational cost is very high and therefore signal can't be processed in real time. In order to develop a fast image rapprochement technique, tissue estimation is reformulated in a quantized domain, where Viterbi algorithm and adaptive quantization techniques can be used for reducing the computational cost of the estimation, allowing a real time implementation.

A reduced states Viterbi algorithm based on adaptive quantization codebook is proposed

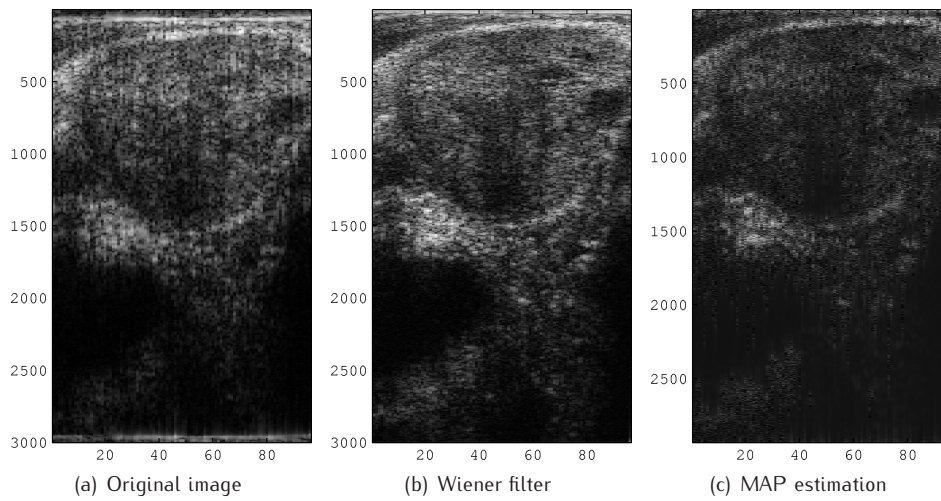


**Figure 4.12:** Comparison between B-mode image before (a) processing, Wiener filter deconvolution (b) and MAP estimation with the proposed method (c).

(a) Prostate results					(b) Phantom results				
	RG	CG	PSNR	SSIN		RG	CG	PSNR	SSIN
Map estim.	4.88	3.38	23.04	0.94	Map estim.	3.85	5.06	2.50	0.96
Wiener filter	1.92	1.62	21.20	0.91	Wiener filter	1.5	1.20	22.00	0.87
FWD [25]	1.72	1.17	17.54	0.77	FWD [25]	1.20	1.70	18.24	0.87

**Table 4.2:** Image enhancement evaluation metrics computed for the in vivo prostate gland frames (a) and for the in vivo phantom frames (b).

for MAP tissue reflectivity estimation. The method has been tested on synthetic signal in order to tune the different parameters of the algorithm and obtain an affordable compromise between computational cost and estimation accuracy. The obtained results show that while Wiener filter produces smoothed version of the true tissue reflectivity, the proposed method is able to recover its sparse nature with interesting noise suppression properties, providing better performance also in terms of power and phase spectrum enhancement.

Finally, to verify the effectiveness of the proposed algorithm as a de-blurring method for ultrasound images the method has been applied on real in-vivo signals of biological tissues and phantom object and compared with Wiener filter and a publicly available deconvolution method, obtaining better performance in terms of visual quality, resolution and contrast enhancement.

Future development of this project can include:

- extension of the proposed model for two-dimension signal deconvolution;
- assessment of the sensitivity of the proposed method to imperfect knowledge of system PSF;
- development of method for regularized estimation of tissue echogenicity;

- development of tissue characterization procedure based on the proposed signal model and MAP estimation.

### Publications

1. A. Palladini, N. Testoni, L. De Marchi, N. Speciale: **ML Estimation for acoustical image de-blurring**. Proceeding of the 29th International Symposium on Acoustical Imaging (AI29).
2. A. Palladini, N. Testoni, L. De Marchi, N. Speciale: **A reduced complexity estimation algorithm for ultrasound images de-blurring**. Proceeding of IEEE International Symposium on Computer Based Medical Systems 2007 (CBMS 2007).
3. A. Palladini, N. Testoni, L. De Marchi, N. Speciale: **A reduced complexity estimation algorithm for ultrasound images de-blurring**. To be published on Journal of Computer Methods and Programs in Biomedicine - special issue of CBMS 2007, Elsevier .
4. L. De Marchi, A. Palladini, N. Testoni, N. Speciale: **Blurred Ultrasonic Images as ISI-Affected Signals: Joint Tissue Response Estimation and Channel Tracking in the Proposed Paradigm** Proceeding of IEEE International Ultrasonic Symposium 2007 (US 2007)
5. M. Alessandrini, A. Palladini, L. De Marchi, N. Speciale: **EM for joint deconvolution and statistics estimation**. Proceedings of 30th International Symposium on Acoustical Imaging (AI30).



---

# Bibliography

---

- [1] *Elements of Information Theory*. John Wiley and Sons, Inc., 1991. [cited at p. 66]
- [2] UR Abeyratne, AP Petropulu, and JM Reid. Higher order spectra based deconvolution of ultrasound images. *Ultrasonics, Ferroelectrics and Frequency Control, IEEE Transactions on*, 42(6):1064–1075, 1995. [cited at p. 55, 68]
- [3] D. Adam and O. Michailovich. Blind deconvolution of ultrasound sequences using nonparametric local polynomial estimates of the pulse. *IEEE Transactions on Biomedical Engineering*, 49(2):118–131, 2002. [cited at p. 55, 57]
- [4] JB Anderson. Limited search trellis decoding of convolutional codes. *Information Theory, IEEE Transactions on*, 35(5):944–955, 1989. [cited at p. 65]
- [5] H.C. Andrews and BR Hunt. Digital image restoration. *Prentice-Hall Signal Processing Series, Englewood Cliffs: Prentice-Hall, 1977, 1977*. [cited at p. 61]
- [6] T.E. et. al. Bishop. *Blind image deconvolution: problem formulation and existing approaches*. CRC Press, 2007. [cited at p. 54]
- [7] C.Y. Chi and J. Mendel. Viterbi algorithm detector for Bernoulli-Gaussian processes. *Acoustics, Speech, and Signal Processing [see also IEEE Transactions on Signal Processing], IEEE Transactions on*, 33(3):511–519, 1985. [cited at p. 63]
- [8] Jr. Forney, G.D. The viterbi algorithm. *Proceedings of the IEEE*, 61(3):268–278, 1973. [cited at p. 63, 64]
- [9] G. Foschini. A reduced state variant of maximum likelihood sequence detection attaining optimum performance for high signal-to-noise ratios. *Information Theory, IEEE Transactions on*, 23(5):605–609, 1977. [cited at p. 65]
- [10] R.C. Gonzalez and R.E.Woods. *Digital image processing*. Prentice Hall, 2nd edition, 1992. [cited at p. 63]
- [11] S.S. Haykin. *Blind deconvolution*. Prentice-Hall. [cited at p. 54]
- [12] F. Jelinek and J. Anderson. Instrumentable tree encoding of information sources (Corresp.). *Information Theory, IEEE Transactions on*, 17(1):118–119, 1971. [cited at p. 65]
- [13] J.A. Jensen and S. Leeman. Nonparametric estimation of ultrasound pulses. *IEEE Transactions on Biomedical Engineering*, 41(10):929–936, 1994. [cited at p. 55, 56, 57]
- [14] R. Jirik and T. Taxt. Two-dimensional blind bayesian deconvolution of medical ultrasound images. *Ultrasonics, Ferroelectrics and Frequency Control, IEEE Transactions on*, 55(10):2140–2153, October 2008. [cited at p. 55, 56]

- [15] KF Kaareesen and E. Bolviken. Blind deconvolution of ultrasonic traces accounting for pulsevariance. *Ultrasonics, Ferroelectrics and Frequency Control, IEEE Transactions on*, 46(3):564–573, 1999. [cited at p. 55]
- [16] S.M. Kay. *Fundamentals of statistical signal processing: estimation theory*. 1993. [cited at p. 57, 58]
- [17] D. Kundur and D. Hatzinakos. Blind image deconvolution. *IEEE Signal Processing Magazine*, 13(3):43–64, 1996. [cited at p. 54]
- [18] C.P. Loizou, C.S. Pattichis, C.I. Christodoulou, R.S.H. Istepanian, M. Pantziaris, and A. Nicolaidis. Comparative evaluation of despeckle filtering in ultrasound imaging of the carotid artery. *IEEE Transactions on Ultrasonics, Ferroelectrics, and Frequency Control*, 52(10):1653–1669, 2005. [cited at p. 68]
- [19] O. Michailovich and D. Adam. Robust estimation of ultrasound pulses using outlier-resistant de-noising. *Medical Imaging, IEEE Transactions on*, 22(3):368–381, 2003. [cited at p. 55, 56]
- [20] O. Michailovich and D. Adam. Phase unwrapping for 2-d blind deconvolution of ultrasound images. *Medical Imaging, IEEE Transactions on*, 23(1):7–25, 2004. [cited at p. 55, 57]
- [21] O. Michailovich and A. Tannenbaum. Blind deconvolution of medical ultrasound images: A parametric inverse filtering approach. *Image Processing, IEEE Transactions on*, 16(12):3005–3019, Dec. 2007. [cited at p. 55, 56]
- [22] O.V. Michailovich and D. Adam. A novel approach to the 2-d blind deconvolution problem in medical ultrasound. *IEEE Transaction on Medical Imaging*, 24(1):86–104, 2005. [cited at p. 55, 57, 59]
- [23] O.V. Michailovich and A. Tannenbaum. Despeckling of medical ultrasound images. *Ultrasonics, Ferroelectrics and Frequency Control, IEEE Transactions on*, 53(1):64–78, Jan. 2006. [cited at p. 53]
- [24] C. Miller, BR Hunt, MA Neifeld, and MW Marcellin. Binary image reconstruction via 2-D Viterbi search. In *Image Processing, 1997. Proceedings., International Conference on*, volume 1, 1997. [cited at p. 63]
- [25] R. Neelamani, C. Hyeokho, and R. Baraniuk. Forward: Fourier-wavelet regularized deconvolution for ill-conditioned systems. *IEEE Transaction on Signal Processing*, 52(2):418–433, 2004. [cited at p. 55, 68, 74]
- [26] J. Ng, R. Prager, N. Kingsbury, G. Treece, and A. Gee. Modeling ultrasound imaging as a linear, shift-variant system. *Ultrasonics, Ferroelectrics and Frequency Control, IEEE Transactions on*, 53(3):549–563, March 2006. [cited at p. 56]
- [27] J. Ng, R. Prager, N. Kingsbury, G. Treece, and A. Gee. Wavelet restoration of medical pulse-echo ultrasound images in an em framework. *Ultrasonics, Ferroelectrics and Frequency Control, IEEE Transactions on*, 54(3):550–568, March 2007. [cited at p. 55, 56, 59, 60]
- [28] AV Oppenheim. *Digital Signal Processing*. DTIC Research Report ADA110902, 1981. [cited at p. 56]
- [29] PM Shankar, VA Dumane, CW Piccoli, JM Reid, F. Forsberg, and BB Goldberg. Classification of breast masses in ultrasonic B-mode images using a compounding technique in the Nakagami distribution domain. *Ultrasound Med Biol*, 28(10):1295–300, 2002. [cited at p. 53]
- [30] DG Sheppard, A. Bilgin, MS Nadar, BR Hunt, and MW Marcellin. A vector quantizer for image restoration. *Image Processing, IEEE Transactions on*, 7(1):119–124, 1998. [cited at p. 63]
- [31] Jinshan Tang, E. Peli, and S. Acton. Image enhancement using a contrast measure in the compressed domain. *IEEE Transaction on Signal Processing*, 10(10):289–292, 2003. [cited at p. 68]
- [32] T. Taxt. Three-dimensional blind deconvolution of ultrasound images. *IEEE Transactions on Ultrasonics, Ferroelectrics, and Frequency Control*, 48(4):867–871, 2001. [cited at p. 55]

- [33] T. Taxt and GV Frolova. Noise robust one-dimensional blind deconvolution of medicalultrasound images. *Ultrasonics, Ferroelectrics and Frequency Control, IEEE Transactions on*, 46(2):291–299, 1999. [cited at p. 55]
- [34] J.M. Thijssen. Ultrasonic speckle formation, analysis and processing applied to tissue characterization. *Pattern Recognition Letters*, 24(4–5):659–675, 2003. [cited at p. 53]
- [35] FL VERMEULEN and ME HELLMAN. Reduced state Viterbi decoders for channels with intersymbol interference. In *International Conference on Communications, 10 th, Minneapolis, Minn*, page 37, 1974. [cited at p. 65]
- [36] S. Wan, BI Raju, and MA Srinivasan. Robust deconvolution of high-frequency ultrasound images using higher-order spectral analysis and wavelets. *Ultrasonics, Ferroelectrics and Frequency Control, IEEE Transactions on*, 50(10):1286–1295, 2003. [cited at p. 55]



## Chapter 5

---

# Ultrasound signal segmentation and classification

---

Accurate segmentation, or simply boundary detection, of prostate in ultrasound images plays a key role in clinical procedures for prostate cancer diagnosis, such as region of interest selection, accurate placement of needles in biopsy protocols and the measurement of the prostate gland volume (see chapter 2). So far, all this tasks have been performed manually by expert radiologist personnel. Since manual delineation of the boundaries is irreproducible, slow and heavily user dependent, automatic segmentation has a significant advantage over manual annotation. However, compared to the other imaging techniques, ultrasound images have lower resolution, lower intensity contrast and inherent speckle noise. All this issues make the automatic segmentation of images difficult and an important area of research.

Another class of algorithms of interest is automatic methods for prostate cancer detection and staging based on machine learning techniques. The shortcomings of the current clinical methods have in fact induced a great number of studies aimed in improving the detection rate of prostate cancer by computer aided techniques, providing assistance to radiologists in the diagnosis of prostate carcinoma and in the guidance of biopsy. However, as mentioned by many authors, since in the learning process only the pixels in the biopsied area can be considered, classification of prostate tissues is an imperfect supervision problem. Moreover, since it is difficult to transform the physical labels in the extracted tissue into pixel labels, even the labels of pixels in the limited area are imperfect. Therefore, although encouraging, the results published so far are often not proven to be clinically significant and not always comparable, mainly because of the lack of standard learning procedures and a publicly available images database.

**Author contributes.** In this chapter, after a review of the existing approach for ultrasound image segmentation and tissue classification, a novel procedure for computer aided diagnosis of prostate cancer based on an automatic method for region of interest selection is presented. The proposed procedure is then tested on an experimental database composed of transrectal scans of prostate glands affected by malignant and benign pathologies.

## 5.1 Ultrasound image segmentation

Ultrasound image segmentation is strongly influenced by signal quality as well as by the tissue imaged. The characteristic artefacts of ultrasound images like attenuation, speckle, shadows and signal dropouts, missing boundaries due to the orientation dependence of acquisition, make the segmentation task complicated. While in other areas of medical imaging (CAT, MRI) application of general image processing methods is sufficient, in the case of ultrasound signals more complex and specialized methods are needed in order to obtain satisfactory results.

In literature, there are a large number of papers describing segmentation procedures applied to ultrasound images. For a complete review of the state of the art of medical and ultrasound image segmentation methods see [32] and [28]. Basically, the techniques proposed so far for medical image segmentation can be summarized in eight main classes:

- thresholding methods;
- region growing methods;
- classification methods;
- clustering methods;
- Markov random field methods;
- artificial neural networks;
- deformable models methods;
- atlas-guided methods;

Since most of the new segmentation techniques reported in literature are often developed for a specific clinical application, in this section we will give a brief review of the main methods employed for medical image segmentation, focusing on their application in the context of prostate ultrasound images segmentation.

Prostate segmentation problem can be meant as two different, and in general independent, segmentation problems: prostate boundary detection and segmentation of prostate gland in regions of interest. While many algorithms for prostate boundary detection have been proposed in literature (see [28] and [2]) only few works concerning region of interests segmentation have been proposed [23][2]. The motivations behind this predominance of work concerning prostate boundary segmentation are basically two. First, prostate boundary segmentation for volume assessment is an important and primary task in current clinical procedure for cancer diagnosis (see chapter 2). Second, since it is not clear in literature which effectiveness measures should be used for evaluating the performance of segmentation methods [12], evaluating the performance of region of interests segmentation algorithms is a complex task that require a large database of manual selections performed by expert personnel .

**Thresholding methods.** The thresholding techniques are the simplest image segmentation methods. They are based on the assumption that the image intensities of the objects to be segmented and the of background follows a multimodal distribution. The breakpoint for

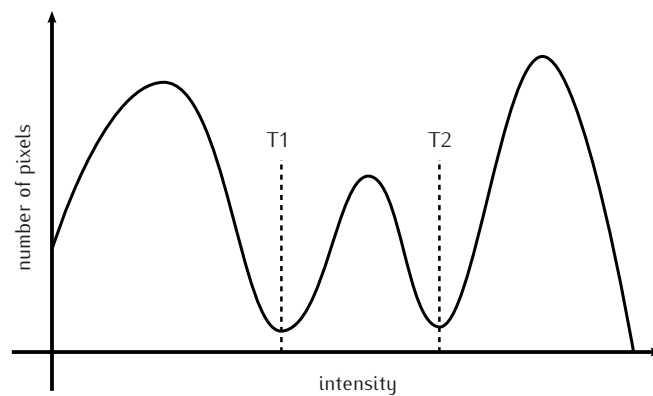


**Figure 5.1:** Example of image histogram showing three apparent classes and correspondent thresholds for image segmentation.

segmenting the image is therefore finding the thresholds for separating the desired classes (see fig.5.1).

Two main classes of thresholding technique can be distinguished: global thresholding and local thresholding. Global thresholding is the simplest and fastest method, since only one set of thresholds is used for the entire image. In local thresholding the image is divided in sub-images that are processed independently with different sets of thresholds. These methods are often more complex and give more accurate segmentations. Thresholding methods can be further classified according to the methods used for computing the thresholds from the image histogram: histogram shape based, clustering based, entropy based, object attributes based, spatial techniques, local techniques. For a complete review see [37].

Thresholding method was applied with success for detecting pubic arch in TRUS during prostate brachytherapy [30]. However, thresholding techniques are not powerful enough for more complex problems like prostate boundaries detection and region of interest segmentation.

**Region growing methods.** The goal of region growing techniques is to divide the image into its regions, according to image properties such as pixel intensity or other statistical information. These techniques require first a seed point to begin from. Then, the pixels connected to that seed point that have the same predefined characteristic are found and added to the region. Region growing methods can be categorized in three classes: merging, splitting and merge and split [25].

Region growing was applied for computing prostate volume from a manually placed seed point in the center of the gland [8]. The critical point in region growing methods is the choice of the properties according to segment the image.

**Classification methods.** Classification methods, described in [41], are pattern recognition techniques where a feature space is partitioned by learning the partitioning function through examples of labelled data points. Such techniques can be easily applied to images associating to each image pixel a feature vector. The disadvantage of this approach is that performance can be biased by the dataset used in learning the partitioning function. Such methods are also very often computationally demanding. Moreover, in medical field training data is not always available or it can't be easily defined. In particular, defining training

set for image segmentation is usually very time demanding and complex and therefore not feasible.

However, some works, about prostate image segmentation using a classification approach, like neural networks, have been reported in literature [33].

**Clustering methods.** Clustering methods lay in the class of unsupervised learning methods. The accuracy of clustering techniques is usually lower than the one obtained with supervised methods. The main advantage of unsupervised methods is that they don't need a training data. The most three common clustering algorithms used so far in medical image segmentation are: the K-means, the fuzzy C-means and the expectation maximization (see [41]). The main limitation of these techniques is that no spatial information is included in the segmentation process.

Recently, also spectral clustering techniques were applied with good results in ultrasound images segmentation, including prostate boundary and regions of interest segmentation [43][1][23] and to my knowledge, together with the method presented in [24], they are the only methods for prostate region of interest segmentation presented in literature. The main limitations of these procedures are two: first regions of interest segmentation is limited only to hypoechoic regions and although hypoechoic regions are the more likely to be cancerous, as reviewed in chapter 2, prostate cancer appearance in ultrasound images can be also hyperechoic and isoechoic. Second, only grey levels and dominant contours features are used for regions of interest segmentation.

**Markov random field methods.** Markov random fields (MRFs) are statistical models that can be used for modelling the spatial interaction between neighbouring or nearby pixels. In medical imaging, they are typically used because most pixels belong to the same class as their neighbouring pixels, since any anatomical structure that consists of only one pixel has a very low probability of occurring.

MRFs are often used for regularizing segmentations obtained with clustering algorithms such as the K-means algorithm, under a Bayesian prior model [4][29]. The regularization is obtained by maximizing the a posteriori probability of the segmentation, given the image data. This maximization is usually achieved by iterative methods such as iterated conditional modes, simulated annealing. The main issue associated with MRF models is proper selection of the parameters controlling the strength of spatial interactions. In addition, MRF methods usually require computationally intensive algorithms.

Despite their disadvantages, MRFs are widely used in many image processing and computer vision problems (image segmentation, image restoration, texture modelling, stereo matching), and they were successfully used for segmenting MRI brain images, and breast lesions in mammography and US scans [6] [5].

**Artificial neural networks methods.** Artificial neural networks (ANNs) are supervised learning models in which the learning function is synthesized by the combination of a large number of simple elementary processing units called neurons.

One of the attractive features of ANNs is their capability to adapt to different tasks. The main limitation of this techniques is that, as all the supervised techniques, their performance depends on the training set which must be big enough. Moreover, although ANNs are intrinsically parallel, their processing is usually simulated on serial computers, thus reducing this potential computational advantage.

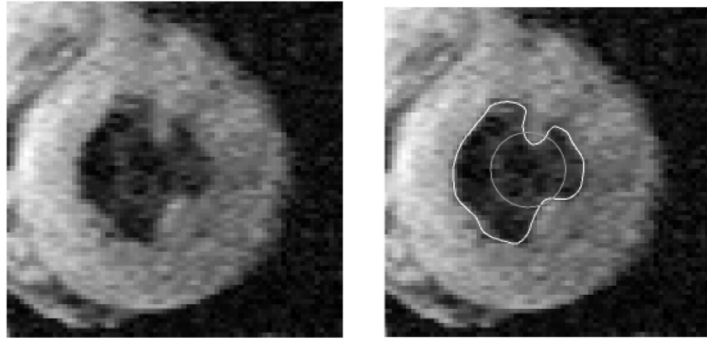


**Figure 5.2:** Example of boundaries segmentation with deformable contours in a MRI image. Left: original image. Right: segmented image with initial (gray) and final (white) boundaries (picture taken from [32]).

ANNs are widely used in medical imaging as a classifiers, for image segmentation [46] and also for prostate segmentation [33].

**Deformable models methods.** Deformable models (or active contours) are model-based techniques for delineating region boundaries by using closed parametric curves, or surfaces, that can be deformed under the influence of force fields. Objects boundaries are therefore delineated placing a closed starting curve (or surface) near the desired boundaries and then deforming it through an iterative relaxation process. Internal forces are computed from within the curve (or surface) to keep it smooth throughout the deformation. External forces are then derived from the image to drive the curve toward the desired boundaries. In fig. 5.2 an example of active contours segmentation is shown.

The main advantages of deformable models are their ability to directly generate closed parametric curves or surfaces from images and their incorporation of smoothness and shape constraint that provides robustness to noise and spurious edges. The main drawback is the requirement of an initialization, often done manually, and a big sensitivity to such initialization. Such problem is critical in case the number and the location of the objects to be segmented are unknown. In this case, a large number of initial curves is required, resulting in computational demanding procedures.

However, deformable models are widely applied in medical image analysis, including prostate boundaries segmentation. For a general review see [21] [2].

**Atlas-guided methods.** Atlas-guided methods are a powerful tool for medical-image segmentation when a standard atlas or template is available. Conceptually, atlas-guided approaches are similar to classifiers except that they are implemented in the spatial domain of the image rather than in a feature space. The atlas is generated by gathering information on the anatomy to be segmented. This atlas is then used as a reference frame for segmenting new images. The main drawback of these techniques is, of course, the need of a database for constructing the atlas. An example of atlas-guide method for computer guided prostate biopsy can be found in [45].

**Summary.** Many research papers concerning prostate ultrasound images segmentation have been published. Most of the techniques presented concern prostate boundary seg-

mentation, while only few works about region of interest segmentation have been published. Most of the methods for prostate boundary segmentation depend on human interaction and their performances are therefore user dependent.

Based on the literature overview of the existing methods it can be concluded that:

- most of the procedures for prostate segmentation are focused on boundary detection;
- most of the algorithms are semiautomatic and require user interaction, which implies more effort, more time, low repeatability and user dependent results;
- most of the algorithms use 2D ultrasound images rather than 3D images, since the segmentation of 3D images can be obtained through the segmentation of the correspondent 2D slices;
- most of the algorithms are based on deformable models;
- most of the algorithms require manual segmented images for training and are therefore highly biased by the training set due to the high variability of prostate shapes;
- the methods for prostate region of interest segmentation presented in literature are limited to hypoechoic regions.

Therefore, to overcome the limitations of the existing procedures, new procedures should ideally be:

- user independent;
- independent on training images;
- focused on regions of interest segmentation.

## 5.2 Ultrasound aided tissue characterization

So far, the most used imaging modality in ultrasound system has been the B mode. With this technique, an estimation of the sonified tissue reflectivity is obtained by extracting the amplitude modulation of the radio frequency echo signal, obtained with an ultrasound probe (see chapter 1.1). In general, B mode images quality is limited by many factors (attenuation, resolution limits, speckle noise, etc.) and therefore radiologists can only obtain a qualitative characterization of the sonified tissues.

The frequency of the ultrasound beam generated by medical commercial equipment ranges from 2 to 10 MHz. During its propagation the ultrasound field undergoes different interactions with the structural elements of the imaged tissues, like scattering and absorption, which are function of the ultrasound frequency, temperature and acoustical characteristic of the tissues. Therefore, the ultrasound echo signal contains valuable information about the physical properties of the tissue.

In general, such information can be estimated analyzing both the radio frequency signal before the envelope detection and the B mode image, and used in combination with machine learning techniques, it can provide a quantitative tissue characterization. The results of this characterization can be displayed to radiologists, together with the conventional B mode image, to be used as additional guidance in biopsy protocols. All the methods presented in literature are based on a common scheme which comprises:

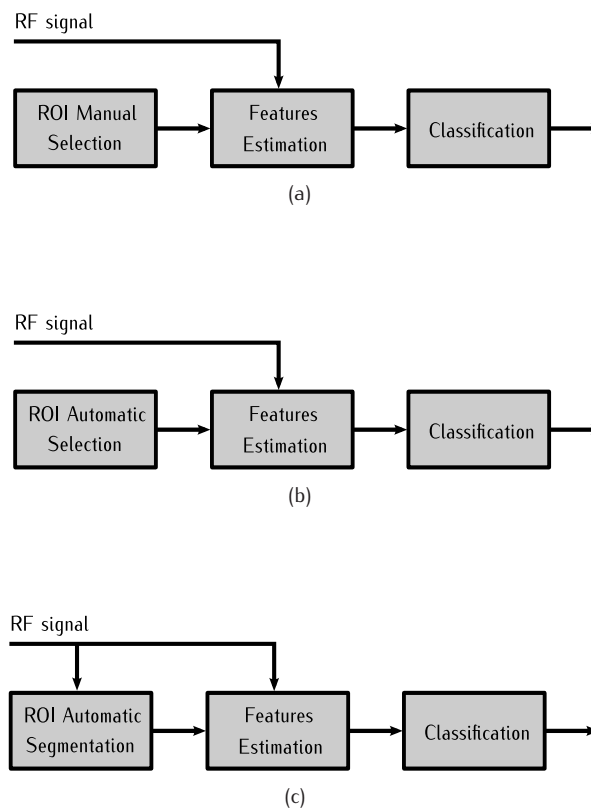


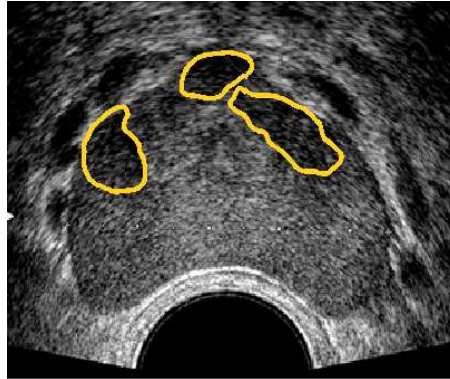
**Figure 5.3:** Schematic representation of different methods for ROI in ultrasound tissue characterization: manual selection (a), automatic selection with rectangular equal-sized regions (b) and automatic adaptive selection with irregular regions (c)

- selection of regions of interests (ROI) to be characterized;
- estimation from Rf signal or/and B mode image of features within the selected ROI;
- classification of the ROI.

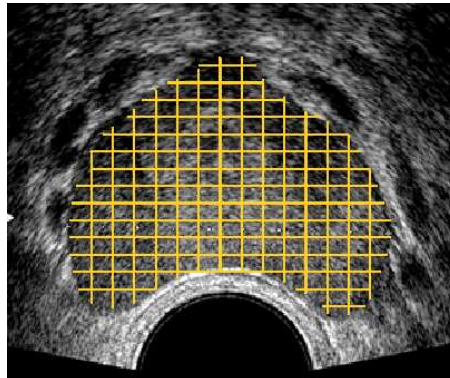
Therefore, the different methods can be classified according to the implementation of each step of this scheme. At first, the different tissue characterization methods can be classified according to the possible ROI selection methods, summarized in fig. 5.3.

The first, and simpler method, is manual selection of the region of interests (fig. 5.3(a) and 5.4(a)). Such procedure, although it is simple and it allows the inclusion of experts knowledge, it's not real time and easily reproducible, it is time consuming and user dependent.

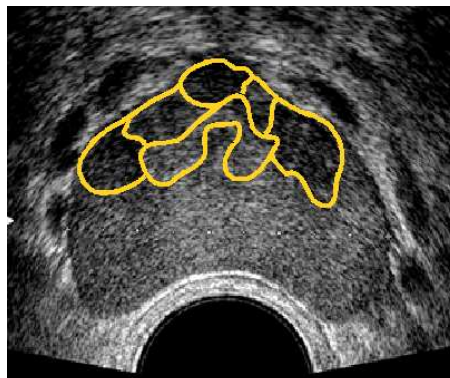
The second method is automatic segmentation of the whole prostate gland in rectangular ROI of equal size (fig. 5.3(b) and 5.4(b)). This procedure is currently the most common used in tissue characterization and once the prostate boundaries are detected is completely automatic and provides good performance. However it is often highly redundant and time consuming (big homogeneous regions are systematically divided in smaller regions) and it



(a) manual selection



(b) automatic selection or rectangular roi



(c) automatic segmentation of irregular roi

**Figure 5.4:** Examples of regions of interest segmentation methods: manual selection (a), automatic selection of regular region (b) and automatic selection of irregular regions(c).

doesn't allow the inclusion of morphological info in the feature estimation step. Moreover, since the ROI are blindly positioned inside the prostate gland, their size is limited by a compromise between classification accuracy and feature estimation reliability: big ROI tend to produce inaccurate characterization while with small ROI size the estimation of many features becomes noisy.

The third method is automatic and adaptive segmentation of the whole prostate gland in ROI of irregular size (fig. 5.3(c) and 5.4(c)). The main difference of this method with respect to the other two is that the segmentation is based on the analysis of the acquired signal, and therefore adaptive. This procedure is theoretically the best one for tissue characterization: it is completely automatic, repeatable, user independent, adapted to the image features and allows the inclusion of morphological information. Feature estimation is usually less computationally demanding, since the number of ROI is noticeably smaller, and its results are less noisy. However, the computational burden of the segmentation must be low in order to keep the advantage due to the reduction of the region of interests. Finally, the performances of the feature estimation and classification steps are strongly dependent to the goodness of the ROI segmentation.

Tissue characterization methods can be further classified according to the type of data required (RF signal, B mode image), employed features, classifier type. Although most of the initial applications of ultrasound-based tissue characterization are related to breast and liver tissues, recently such methods have been extended with success to other type of tissues like bones, myocardium, retina. For a survey on the existing ultrasound-based tissue characterization procedures see [39] and [34].

**Prostate tissue characterization.** A review of the published methods for prostate cancer detection can be found in [26]. In this chapter, that review is integrated with some works published after its compilation and with some works already existing that were not included. The review of the published methods was focused on the system of acquisition and data used (type, probe central frequency, sampling frequency, number of cases available), region of interests available (type, size and number), classification technique (features and classifier) and on the obtained performance (sensitivity, specificity and accuracy). The results of the review are shown in tab.5.1. Based on the results of the review it can be concluded that:

- the number of available cases is often low with respect to the high variability of prostate cancer;
- although in the past B mode was the only data available, the accessibility RF signal is now available in commercial equipment and its use for tissue characterization is increasing;
- in most of the works published ROI are rectangular and equal-sized;
- the size of the ROI is different and ranges from 0.1 cm<sup>2</sup> up to 1.45 cm<sup>2</sup>;
- the standard features used are: first order, textural parameters, fractal parameters, spectral parameters when RF signal is available;
- the optimal features employed don't match across the publication, which suggests a data-set dependency of optimal features;
- combining features from B mode and RF signal results in more effective classification;

WORK	DATA			
	Type	Probe	Sampling	Cases
Basset [3]	B mode	-	-	-
Houston [15]	B mode	7 MHz	33 MHz	25 (11)
Loch[27]	B mode	7.5 MHz	33 MHz	61
Mohamed [22]	B mode	-	-	-
Llobet [19]	B mode	-	-	289
Schmitz [36]	RF	7.5 MHz	33 MHz	33
Scheipers[35]	RF	7.5 MHz	33 MHz	100
Feleppa [10]	RF	7.5 MHz	50 MHz	67 (26)
Mohamed [24]	RF	7 MHz	-	20

(a)

WORK	ROI		TECHINQUE		RESULTS		
	Size	Number	Features	Classifier	SE	SP	ACC
Basset [3]	64 x 64	-	Textural	-	71	83	-
Houston [15]	121 x 10	25	Textural	-	73	86	80
Loch[27]	-	553	Textural	Neural N.	-	-	84
Mohamed [22]	Irregular	-	Textural	SVM	83	90	83
Llobet [19]	Irregular	1531	Textural	SVM	68	53	61.6
Schmitz [36]	128 x 16	170484	Multi.	Neuro-Fuzzy	-	-	86
Scheipers[35]	128 x 16	3405	Multi.	Kohonen Map	82	88	83
Feleppa [10]	64 x 1	705	Spectral	Neural N.	-	-	80
Mohamed [24]	Irregular	3405	Multi.	SVM	83	100	94.4

(b)

**Table 5.1:** Comparison of the the published methods for prostate tissue characterization with ultrasounds.

- because the features used have highly nonlinear interdependence, only nonlinear models like support vector machines and neural networks seems to be suitable for classification;
- with an average accuracy bigger than 80 %, the published ultrasound tissue characterization methods outperform visual interpretation of images;
- a critical comparison of the different methods is missing, mainly due to the lack of large publicly available image dataset;
- clinical evaluation of the methods is fundamental for assessing their real performance;
- no information about computational cost and implementation of the methods is available.

Therefore, to overcome the limitations of the existing procedures, new procedures should ideally be:

- based on features that are less depended by the acquisition system;
- focused on automatic segmentation of irregular regions of interest;
- tested on a large database with several examples of the different cancer stages and variants;
- tested in a clinical environment to asses the real diagnostic accuracy;

### 5.3 Proposed system for ultrasound-aided prostate cancer diagnosis

According to the review on the published methods for prostate segmentation and tissue characterization, relying on the paradigm of fig. 5.4(a) a new procedure for ultrasound aided prostate cancer diagnosis with the following characteristics is proposed:

- the segmentation is performed with a multi feature approach, i.e. different classes of features are estimated;
- all the features are estimated starting from the radio frequency signal before time gain compensation and envelope detection;
- B mode features are estimated after envelope detection and log compression of the radio frequency signal;
- since many boundary estimation algorithms are available in literature, a rough estimation of prostate boundary is considered as given and therefore as input to the system;
- prostate boundary estimation is assumed to be inaccurate as performed by automatic algorithm or done manually by non trained personnel;
- ROI selection is performed inside the given prostate border with an automatic and adaptive procedure, in order to produce ROI of different size;
- since prostate boundary is assumed to be unreliable, ROI selection algorithm must be robust against it;
- among the methods for ultrasound signal segmentation, procedure based on unsupervised learning and Markov random field are used because of their ability in classify heterogeneous data and simple inclusion of a priori information;
- the performance of ROI selection algorithm on *in-vivo* images are evaluated in the context of the overall tissue characterization system, and therefore by means of the accuracy in detecting and classifying lesions;
- supervised and nonlinear learning methods are used for ROI classification;

The proposed procedure is therefore based on three steps: automatic segmentation of prostate in ROIs, features estimation on the segmented ROIs, characterization of ROIs through a classifier. Each step on the method, and its performance on real *in-vivo* images, are explained in details in the following sections.

#### 5.3.1 Regions of interest segmentation algorithm

A schematic representation of the proposed algorithm for ROI segmentation is shown in fig. 5.5. The algorithm is composed of four sequential steps:

- features estimation with a moving window for each signal sample inside the prostate;
- segmentation of each sample in  $K$  different classes with a clustering procedure;
- regularization of the segmentation through a Markov random field based algorithm;
- identification of regions boundary and elimination of regions smaller than a fixed area;

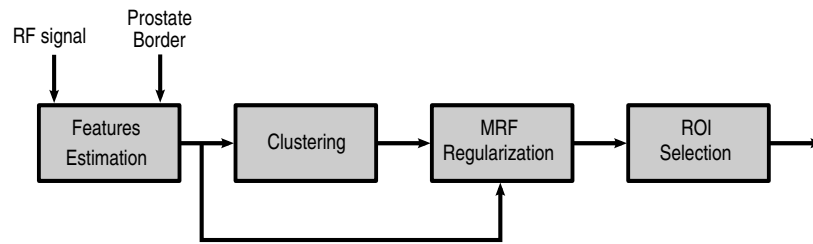


Figure 5.5: Schematic representation of the ROI segmentation algorithm.

### Features estimation

The goal of ROI segmentation algorithm is to divide the prostate gland in regions of interest according to the characteristics of the imaged tissues. Such segmentation is realized by means of features that are extracted from the observed signal in order to capture the different characteristics of the imaged tissue that can be estimated.

As reviewed in chapter 2, normal and cancerous prostate tissues have an heterogeneous set of appearance patterns, which makes identification of the different regions extremely difficult. As claimed by many authors [36][35][26], a multi feature approach is fundamental for prostate tissue characterization.

First of all, homogeneous regions that can be clearly seen in the B mode images must be identified. Therefore, textural features as well as statistical parameters extracted from the signal envelope should be employed. Furthermore, some kind of lesions appears as isoechoic to the surrounding tissues. In order to detect such lesions, features related to physical characteristics, like spectral features and statistical models of backscattering, must be included.

Among the features proposed in literature and developed in this work, the following were tested:

- **texture parameters:** Haralick's and Unser's features [44];
- **spectral parameters:** central frequency, midband, slope [18];
- **B mode statistical modeling:** Nakagami [38], Nakagami fitting of the image diffused component extracted with the method preseted in [];
- **RF signal statistical modeling:** generalized gaussian [42].

Since a complete set of all parameters tested has a big dimensionality and most of the features are correlated, in order to keep the computational cost of the segmentation procedure low, a selection of the most significative ones is necessary.

### Clustering

Although, as emerged from the literature review, methods based on deformable models are used in most of the published papers, all of them are focused on prostate boundary segmentation rather than ROI selection. Deformable models are proved to be efficient when the number of desired regions of interest is either well defined or easily deducible from the image to be segmented. Due to the heterogeneous appearance in ultrasound images of the prostate tissues, the number of regions of interest can vary noticeably from image to image.

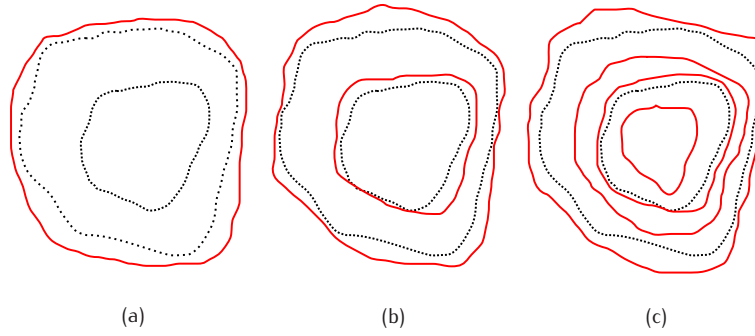


**Figure 5.6:** Three examples possible segmentation results (continuous line) respect to a ground truth reference (dotted line): (a) wrong estimation of clusters number, (b) correct estimation, (c) cluster overfitting.

Moreover, most of the segmentation procedure that are based on deformable models use only the grey level image for guiding the segmentation, which is not suitable for prostate tissue characterization. Thus, among the techniques for ultrasound signal segmentation, reviewed in section 5.1, methods based on unsupervised learning are adopted in this work. As shown in fig. 5.5, the segmentation procedure is based on a clustering algorithm followed by a MRFs regularization.

Clustering techniques easily allows the combination of multiple description parameters and data mining in an high dimension space, with a feasible computational cost. All the clustering methods aim to group data points into clusters, basing only on the information found in the data that describes the points and their relationships. For an extensive review of clustering techniques see [40]. In this work, three different clustering algorithm were evaluated: K-means[40], G-Means [14] and PG-Means [11].

K-means is one of the most popular iterative descent clustering algorithms. It is a distance based clustering algorithms, i.e. similarity between points is evaluated by means of their distance in the feature space. More precisely, points partitioning is obtained by minimizing the following energy function:

$$W(C) = \frac{1}{2} \sum_{k=1}^K \sum_{C(i)=k} d(x_i, \bar{c}_k) \quad (5.1)$$

where  $C$  represent the clustering of all the data points  $i$  in  $K$  predetermined number of clusters,  $C(i) = k$  stands for the assignment of the  $i$ th data point to the  $k$ th cluster with center  $c_k$ , and  $d(\cdot, \cdot)$  is the distance measure which can be either euclidean, cosine, Minkowski or Mahalanobis. Minimization of the functional (5.1) require the joint minimization with respect to clusters centers  $c_k$  and assignment of data points to clusters, and it is not feasible in closed form. However, it can be minimized by an iterative procedure, the K means algorithm, which consists of two steps:

1. for a given clustering  $C$  eq.(5.1) is minimized with respect to cluster centers  $\{c_1, \dots, c_K\}$  yielding the mean of the point currently assigned to each clusters;
2. given a current set of means  $\{c_1, \dots, c_K\}$ , eq.(5.1) is minimized assigning each data point to the nearest cluster center  $c_k$ , with respect to distance  $d(\cdot, \cdot)$ ;
3. step 1 and 2 are iterated until the assignment does not change.

An important point in K-Means is the choice of settings: distance measure, number of clustering classes and initial values for the centroids. The most critical parameter is the number of clustering classes, which is usually a priori unknown in ultrasound images. In the context of medical images, a clustering algorithm should be able to isolate the different homogeneous regions, detecting with good precision their boundaries and possibly avoiding their splitting in unnecessary smaller regions, i.e. clusters overfitting, as shown in fig.5.6.

In literature, different methods for estimating the number of clusters in data have been proposed [41] [14] [11]. Although these methods provides in general good performance they are very computational intensive. Moreover, especially when data clusters are slightly superimposed in features space, very often the number of cluster estimated is bigger than the real number of cluster required, resulting in data overfitting. Therefore, in this work we adopted a fixed number of clusters testing different values between 4 and 8 in order to obtain a good isolation of the pathological regions from the healthy regions. No high accuracy in boundary detection is required in this phase, since this requirement will be fulfilled by the MRF regularization algorithm.

### MRF regularization

The main drawback of clustering techniques is the lack of spatial information, which in the case of ultrasound images causes noisy segmentations, with irregular jagged-edges, wrong classified pixels and small isolated ROIs. Such issue can be mitigated applying a regularization algorithm, based on a MRFs [4], on the segmentation obtained with the clustering procedure, as proposed in [29]. This paradigm was applied with success for the first time to ultrasound images in [7], for breast lesion segmentation.

Image segmentation problem is now formulated as a MAP estimation problem: the observed features vectors  $Y_i = \{Y_{i,1}, \dots, Y_{i,N}\}$  for each image pixel  $i$  are modelled as a Markov random field on a 2D rectangular grid and the data to be estimated is the assignment of each pixel  $i$  to a class  $k \in \{1, \dots, K\}$ , indicated as  $X_i = k$ . The segmentation of the whole image  $X$  is therefore given by

$$\begin{aligned} X_{MAP} &= \arg \max_X p(Y|X)p(X) \\ &= \arg \min_X -\ln p(Y|X) - \ln p(X). \end{aligned} \quad (5.2)$$

The conditional distribution  $p(Y_{i,j}|X_i = k)$  of the observed feature  $j$  is assumed to be Gaussian with conditional mean  $\mu_{i,j}^k$  and conditional variance  $\sigma_{i,j}^k$ . The class  $X_i$  is modeled as a MRF and therefore, thanks to the Hammersly-Clifford theorem, the prior density  $p(X)$  can be written as a Gibbs density:

$$p(X) = \frac{1}{Z} \exp \left\{ - \sum_{c \in I} V_c(X) \right\} \quad (5.3)$$

where  $c$  are the cliques, i.e. a subset of the whole image  $I$ , that are neighbours of each other. The function and  $V_c(X)$  is the clique potential function, which in this work is a defined on second order neighbourhood system defined as follows

$$V_c(X) \begin{cases} -\beta, & \text{if } X_i = X_q \\ +\beta, & \text{if } X_i \neq X_q \end{cases}, \beta > 0 \quad (5.4)$$

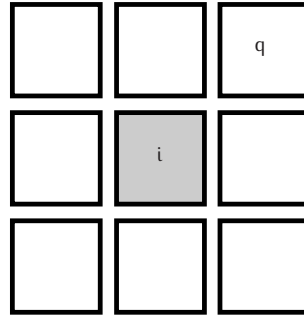


Figure 5.7: Second order neighborhood system

where  $\beta$  is the Gibbs parameter,  $i$  is the center of the clique center and  $q$  is a point inside the clique, as shown in fig 5.7.

Under these assumptions and under the assumption of independent features and of conditional independence of all the image pixels the minimization of (5.2) is equivalent to the minimization of the following energy function

$$U(X|Y) = \sum_j \sum_i [\ln(\sigma_{i,j}^k) + \frac{(Y_{i,j} - \mu_{i,j}^k)^2}{2(\sigma_{i,j}^k)^2}] + \sum_{c \in C} V_c(X) \quad (5.5)$$

Since this would result in unacceptable computational requirements, all the algorithms renounce to achieve the global optimum and try to minimize a different function. One of the most used energy minimization algorithm is the *Iterated Conditional Modes* (ICM), first proposed in [4] and applied in different medical image segmentation problems. The ICM minimizes the energy function no more on the entire grid, but pixel-by-pixel. In other words, we have to minimize in every pixel:

$$U(x_i|Y) = \sum_j [\ln(\sigma_{i,j}^k) + \frac{(Y_{i,j} - \mu_{i,j}^k)^2}{2(\sigma_{i,j}^k)^2}] + \sum_{c \in \delta_i} V_c(X) \quad (5.6)$$

where  $\delta_i$  is the neighbourhood system centered on the pixel  $i$ . This results in an iterative algorithm which drastically reduces computational requirements, and it provides a local optimum very close to the global one, if initialized with K-means segmentation. The algorithm was implemented following the adaptive methodology proposed in [29]: conditional mean  $\mu_{i,j}^k$  and conditional variance  $\sigma_{i,j}^k$  are estimated over windows whose size is reduced after a certain number of iteration until algorithm convergence is reached, i.e. either the number of modified pixels is lower than a fixed threshold or the maximum number of iteration has been reached.

After The parameters to be tuned are therefore:

- the number of iterations with fixed window;
- the maximum number of total iteration;
- the minimum number of modified pixels;
- the Gibbs constant.

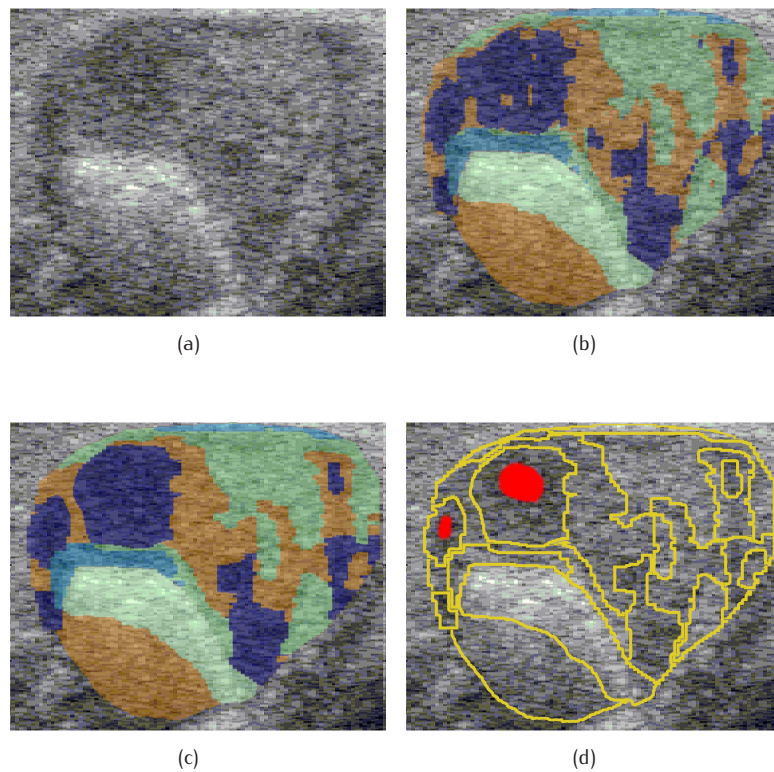


**Figure 5.8:** Example of ultrasound image segmentation: prostate B mode image (a), K-means segmentation with 5 classes (b), ICM regularized segmentation (c) and selected ROI with cancerous zones marked in red (d).

As shown in pic.5.8, the segmentation provided by the ICM is much better than K-Means one: clusters are now more regular and the effect of speckle noise is completely removed. Recently, new clustering algorithms based on MRF and capable of achieving a almost-global optimum have been developed. However, the ICM is far more efficient, and it is now the algorithm that best combines computational demands and effectiveness. For details, refer to [9].

#### ROI selection and performance evaluation

If the regularization performed by the ICM was successful, we expect that all the image pixels are clustered groups of homogeneous image intensity and well defined shape. The different clusters are then examined and further divided according their spatial distribution: all the pixels that forms a connected and closed area are identified as a single region of interest. If ROI of a minimum size are required, all the regions smaller than a fixed number of pixels are reassigned to the adjacent regions applying a morphological erosion operator on them [13]. An example of a B mode image segmentation with the intermediate steps output is shown in fig.5.8.

Since segmentation is performed with an unsupervised learning procedure and a complete a ground truth is not available, evaluating segmentation accuracy in a quantitative manner is not easy. While in prostate boundary segmentation an high precision is demanded, in ROI segmentation the main requirement is to divide prostate gland in regions

smaller enough in order to isolate the regions marked as pathological with good accuracy and divide the remaining part of the gland avoiding overfitting. Such condition can be easily verified and therefore used for selecting the most relevant features and tuning the number of clustering classes, in order to avoid clusters overfitting and inclusion of pathological regions in healthy regions.

As reported by some authors [19], unless radical prostatectomy is performed, due to the biopsy protocol employed in prostate cancer assessment, only partial information about the extension of pathological region is available (see chapter 2 for details). Therefore, in most of the cases, classification of prostate tissues is a semi-supervised learning problem.

As explained in detail in the next sections, the images database used in this work is constituted of images where biopsy confirmed pathological regions are marked above the B mode scans. Since such regions represent a smaller part of the whole unknown pathological areas, they can be considered as an high specificity (almost 100%) and low sensitivity pixels labelling. Thus, the segmentation parameters were set in order to obtain ROI small enough to isolate the marked regions, avoid cluster overfitting and minimize segmentation time as:

- 4 clustering classes;
- 2 iterations with fixed window;
- 8 the maximum number of total iteration;
- 1% of image pixels as minimum number of modified pixels;
- Gibbsian constant  $\beta = 4$ ;

while Euclidean distance and Unser's textural features, Nakagami envelope fitting and RF spectrum central frequency seems to provide the best compromise between segmentation accuracy and computation time.

### 5.3.2 Feature estimation and selection for ROI characterization

Once the ROI are selected, a new set of features is computed for each of them. Besides the feature estimated for image segmentation, also the following feature were tested:

- **texture parameters:** fractal parameters [44];
- **spectral parameters:** polynomial fitting of wavelet spectrum [20];

The main difference with the feature estimation performed in the segmentation step is that now the features are no more computed on a sliding window: each ROI is examined as a unique set of data points. Besides to provide a more robust estimation of all the features, this approach allows the estimation of morphological features, when they could be relevant for ROI characterization, and reduces noticeably the number of parameters to be extracted with a consequent reduction of the computational cost.

A complete feature set of all parameters mentioned before would have a huge dimensionality of about 140 attributes. For this reason a first selection step is performed keeping for each group of features only those highly correlated to the ground truth class, and so to the pathology, discarding the other ones. This way dimensionality is reduced but synergies between different features are saved.

In this application a hybrid feature selection algorithm is used to rank and prune the initial feature set [17]. Hybrid feature selection algorithms take advantage both of filter and wrapper models, i.e. they make use of both an independent measure and performances of a mining algorithm to evaluate feature subsets. Independent measure is used to decide the best subset for a given cardinality while mining algorithm are used to select the final best subset among the best subsets across different cardinalities.

The chosen independent measure is the min-Redundant Max-Relevance (mRMR) criterion proposed in [31]. The mRMR measure is based on mutual information between the current feature set and class corrected with the averaged mutual information between features in the feature set. Maximizing this measure yields to define a feature set  $S$  with maximum relevance with respect to a class  $c$

$$D(S, c) = \frac{1}{|S|} \sum_{Y_i \in S} I(Y_i, c) \quad (5.7)$$

and minimum redundancy

$$R(S) = \frac{1}{|S|^2} \sum_{Y_i, Y_j \in S} I(Y_i, Y_j) \quad (5.8)$$

where  $Y_i$  is a feature and  $I$  is the mutual information. In practice, the first step of hybrid feature selection algorithm consists on maximizing mRMR measure defined as

$$\Phi(D, R) = D - R \quad (5.9)$$

The chosen mining algorithm is a Fisher Linear Discriminant (FLD) and the implemented search technique is a sequential forward selection. For increasing cardinality subset maximizing mRMR measure is selected and performances of FLD trained on this subset are computed. The feature selection outputs are both a ranked list and a minimum subset, dependent on the mining algorithm. The best cardinality and consequently the best subset are chosen as that performing the minimum FLD misclassification error. Typically the best cardinality is smaller than the maximum number of features because not all of them have the same relevance. The selected and ranked feature for the available dataset is constituted of 54 attributes and is shown in table 5.2, where the first 20 features are meant to be the most relevant.

### 5.3.3 Classification

The last stage of the proposed method is a supervised classifier. In this phase, the selected ROI are classified by means of the set of features extracted in the feature selection procedure. The result of the classification will be displayed over the standard B mode image: position and extension of all cancerous ROIs are marked with false colors. Such information can be used by radiologist in guiding biopsy protocols.

Among the possible supervised machine learning techniques a Support Vector Machine (SVM) classifier was adopted[41]. As reported in the literature review at the beginning of this chapter, nonlinear classifier seems to be preferable for prostate tissue characterization and SVM have been proved to be a good choose.

SVMs are a set of related supervised learning methods used for classification and regression. Viewing input data as two sets of vectors in an  $n$ -dimensional space, an SVM will construct a separating hyperplane in that space, one which maximizes the margin between

Index	Feature name	Index	Feature name
01	Fractal(2) Alfa1	28	Fractal(2) Alfa4
02	WDES Diff. Proj. n.8	29	homogeneity135
03	Intercept AR(2)burg	30	Bmode
04	correlation135	31	mean90
05	Nakagami logm	32	Fractal(2) Beta4
06	Fractal(1) Beta10	33	Intercept2 AR(3)lmsd
07	Fractal(2) Beta10	34	Fractal(1) Beta8
08	Naka w Diff. Proj. n.8	35	Slope
09	Nakagami logOmega	36	Fractal(2) Beta8
10	homogeneity90	37	Geometric feature
11	mean0	38	Fractal(2) Beta3
12	Fractal(1) Alfa3	39	Fractal(1) Alfa5
13	Fractal(2) Beta6	40	Fractal(1) Beta6
14	Slope1 AR(3)burg	41	Intercept1 AR(3)lmsd
15	Fractal(1) Alfa1	42	ASM Estimated Fc
16	clusterprom135	43	Haralick Left Entropy
17	Geometric feature	44	Slope AR(2)lmsd
18	entropy135	45	WSP Band 3
19	Fractal(2) Beta2	46	Fractal(2) Alfa2
20	contrast90	47	correlation45
21	Intercept ZC	48	Intercept
22	Slope FFT	49	Fractal(1) Alfa9
23	Haralick Left Sum of Squares	50	Slope ZC
24	Slope1 AR(3)lmsd	51	Slope AR(2)burg
25	WSP Fit Coeff. 2	52	Haralick Left Correlation
26	Slope2 AR(3)burg	53	Haralick Left Sum Average
27	WSP Band 1	54	Naka w Coher. Proj. n.9

Table 5.2: Feature selection and ranking results.

the two data sets. To calculate the margin, two parallel hyperplanes are constructed, one on each side of the separating hyperplane. Intuitively, a good separation is achieved by the hyperplane that has the largest distance to the neighbouring datapoints of both classes, since in general the larger the margin the better the generalization error of the classifier.

The original optimal hyperplane algorithm proposed by Vladimir Vapnik in 1963 was a linear classifier. However, in 1992, Bernhard Boser, Isabelle Guyon and Vapnik suggested a way to create non-linear classifiers by applying the kernel trick to maximum-margin hyperplanes [41]. The resulting algorithm is formally similar, except that every dot product is replaced by a non-linear kernel function. This allows the algorithm to fit the maximum-margin hyperplane in the transformed feature space. The transformation may be non-linear and the transformed space high dimensional; thus though the classifier is a hyperplane in the high-dimensional feature space it may be non-linear in the original input space. Some common kernels include:

- polynomial functions (homogeneous or inhomogeneous);
- radial basis function;
- Gaussian radial basis function;
- sigmoidal functions;

For further details about SVMs see [41]. In this work a Gaussian radial basis function was adopted and the corresponding feature space is thus a Hilbert space of infinite dimension. All the simulations were performed using the publicly available software implementation of SVM classifiers called *svmlight* [16].

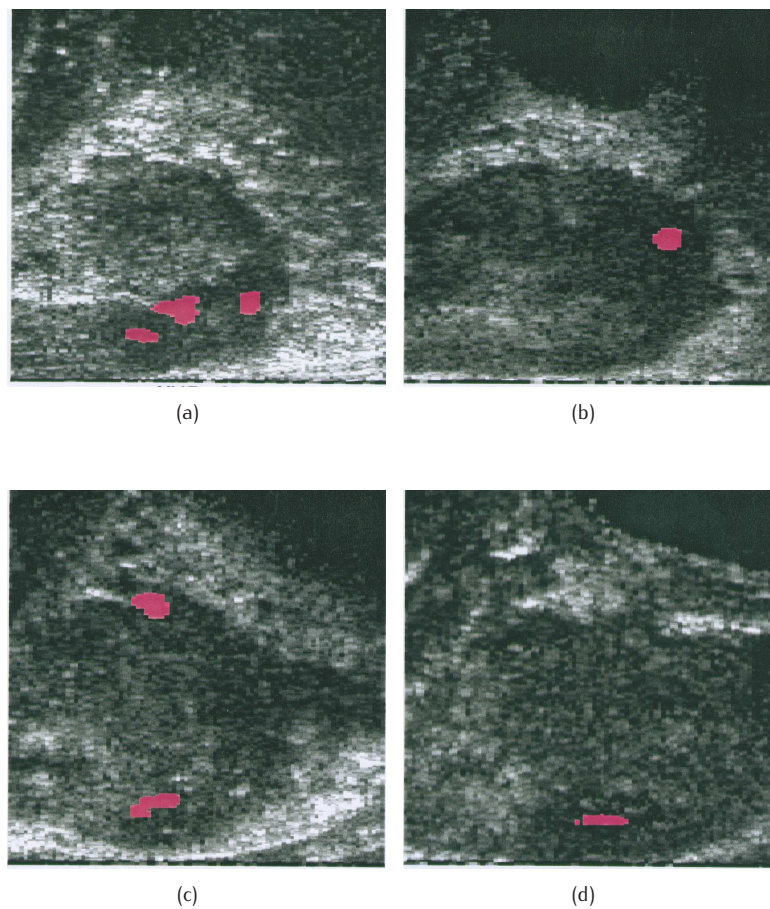


Figure 5.9: Example of database reference images for supervised learning representing different prostate sagittal sections, with histologically confirmed cancerous regions marked.

## 5.4 Experimental results

The proposed method for prostate tissue classification was applied to a database of in-vivo scans in order to assess its accuracy. The experimental database was provided by the University of Florence and is formed by TRUS images of prostate sagittal section. All the signals were acquired with a commercial ESAOTE ultrasound machine using a transrectal broadband probe, with central frequency of 7.5 MHz, sampling at 50 MHz the radio frequency signal before time gain compensation with a resolution of 12 bits. The dataset contains 37 different cases of prostate pathologies, 22 cases of prostate carcinoma and 15 cases of benign hyperplasia, acquired before biopsy. For each case, ten consecutive image frames were recorded.

All the malignant cases have cancerous regions marked on the B mode image by radiologist after histological verification. All the cancer foci were identified during the histological examination. These labels constitute the ground truth for both segmentation algorithm tuning and classifier training. In fig.5.9 some examples of the reference images are shown. Since, unless radical prostatectomy is performed, with high probability the portion of tissue sampled during biopsy is smaller than the true cancer extension, the available ground truth

must be considered as an incomplete labelling. The learning problem is not fully supervised and specificity of the classification can't be evaluated in a reliable way.

However, since the main goal of computer methods for prostate cancer diagnosis is the identification of all the cancer foci for guiding biopsy, possible overestimations of the size of cancerous region does not affect the clinical performance of the computer aided diagnosis procedure. Thus, the main goal is the development of an high sensitivity classification method which is able to identify all the cancer foci with an average level of specificity.

#### Learning procedure and performance test

For pursuing the mentioned goals the learning problem was formulated in the following way:

- the whole images database is segmented using the proposed segmentation method, obtain about 300 ROI;
- all the examples of normal ROI are taken only from the benign cases;
- only the ROI marked by radiologist as pathological are used as examples of cancerous regions in the learning phase;
- the whole set of features listed in table 5.2 are extracted above the selected ROI;
- the classifier is then trained above a random subset of the available data using stratified 10-fold cross validation;
- the remaining images are then segmented using the proposed segmentation method;
- in calculating classification performance, the ROI extracted are now considered as normal or cancerous according to the available ground truth: all the ROI that are superimposed for more than the 70% with the ground truth are entirely labelled as cancerous;

Since ROI have different sizes, the classification results must be normalized in order to take into account the size of each ROI. Therefore, classification performances are evaluated in terms of correctly classified pixels inside the prostate border.

Typical measures to assess classifier performances are sensitivity ( $SE$ ), specificity ( $SP$ ), accuracy ( $Acc$ ) defined as:

$$SE = \frac{TP}{TP+FN} \quad (5.10)$$

$$SP = \frac{TN}{TN+FP} \quad (5.11)$$

$$Acc = \frac{TP+TN}{TP+TN+FP+FN} \quad (5.12)$$

where  $TP$  are true positive pixels,  $TN$  are true negative pixels,  $FP$  are false positive pixels and  $FN$  are true negative pixels.

Since, in the segmentation phase and in other investigation performed on the same dataset, some malignant cases were proved to be source of errors, two different data set where created:

- Dataset 1, which comprises all the available cases;
- Dataset 2, where 4 malignant cases where excluded during the training phase.

Settings	<i>SE</i>	<i>SP</i>	<i>Acc</i>
Set 1 - 10 features	0.80	0.71	0.75
Set 1 - 20 features	0.93	0.73	0.87
Set 1 - 54 features	0.95	0.74	0.89
Set 2 - 54 features	0.90	0.84	0.87

**Table 5.3:** Classification performance of the proposed tissue characterization method.

The average classification performance obtained by the proposed procedure on the two dataset are resumed in table 5.3. The classification results confirm that the first 20 features are the most relevant: while increasing the number of features from 10 to 20 a significant performance improvement is noted, only slightly improvement are obtained when the complete set of feature is used. Among the most relevant features we found textural features (Unser's and fractal), statistical features (Nakagami and Nakagami fitting on the diffused component extracted from the B mode image) and spectral (slope, intercept), confirming that a multi-feature approach is fundamental.

Moreover, the results confirm that excluding the ambiguous case from the training set improve significantly the sensitivity of the method. The high value of sensitivity obtained (always  $> 90\%$ ) suggests that the proposed method is able to identify most of the known cancer locations. As said before, since only partial information about the real extension of cancerous areas is available and since classification were performed above the whole image, the specificity value obtained is not fully reliable and gives just quantitative information about method performance. However, analyzing the results obtained on the benign cases we observed that the number of false positive is extremely low and we can therefore conclude that the low specificity value is due to the over estimation of cancer size in malignant images. Since the classification results are meant to be used for guiding biopsy, an over estimation of the tumour size is less problematic than false positive on benign cases, which would causes unnecessary additional biopsies.

Finally, in figures 5.10 and 5.11 examples of the classification results displayed above the B mode scans as visual guidance for biopsy are given.

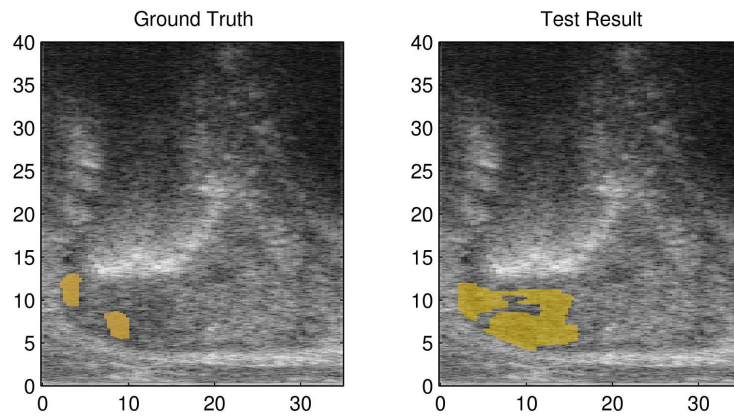
## 5.5 Discussion

The primary goal of the research presented in this chapter was the development of a computer aided detection procedure for prostate cancer assessment by means of TRUS scans. The function of the proposed tool is assisting radiologist to accurately identify the suspicious regions for biopsy.

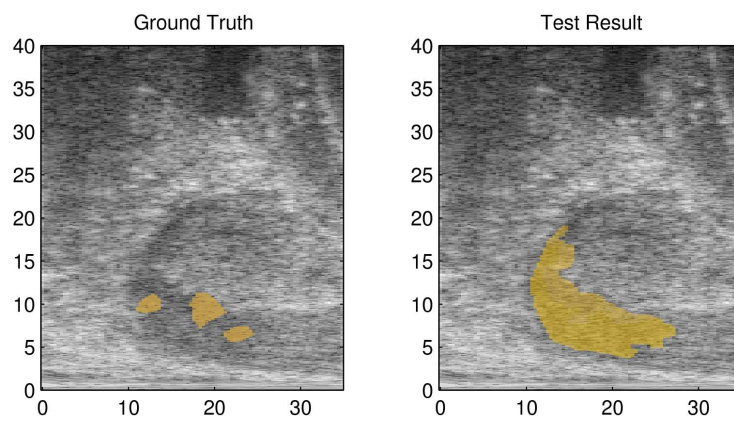
After a complete review of ultrasound image segmentation and tissue characterization techniques presented in literature, the main characteristics for the development of a novel computer aided tissue characterization were defined. The proposed method consists of two main parts: regions of interest segmentation and tissue characterization.

Regions of interest segmentation is based on an automatic selection of the region of interests inside the prostate gland performed by means of an unsupervised learning procedure. The prostate gland boundary is supposed to be known but, since its accuracy does not influence the accuracy of region of interest segmentation, it can be performed manually by non trained users or automatically, by one of the different algorithms proposed in literature.

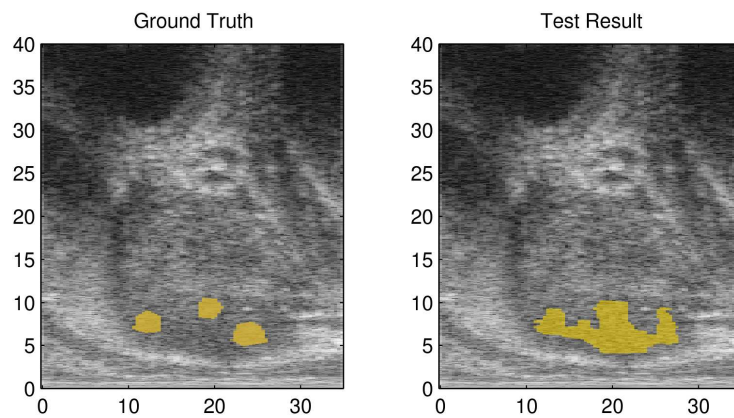
Tissue characterization step is based on a multi features approach where the features are extracted from both radio frequency signal and B mode image. Each region is then



(a)

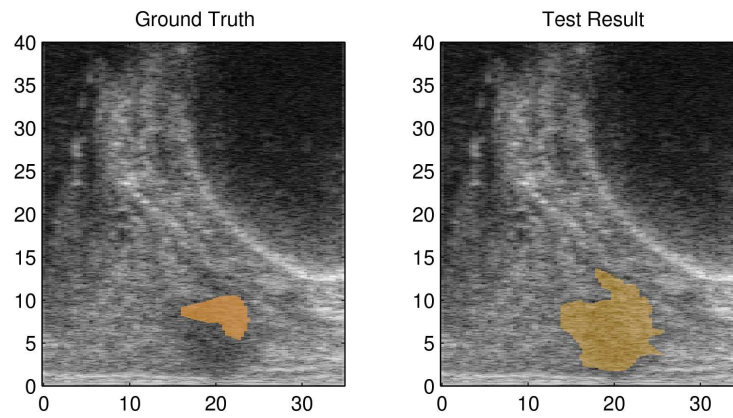


(b)

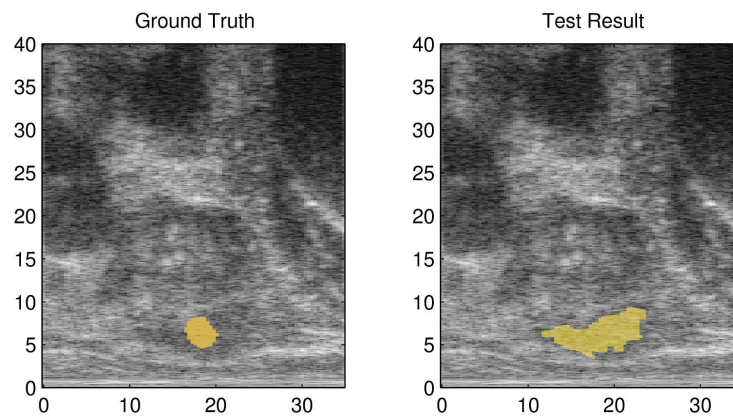


(c)

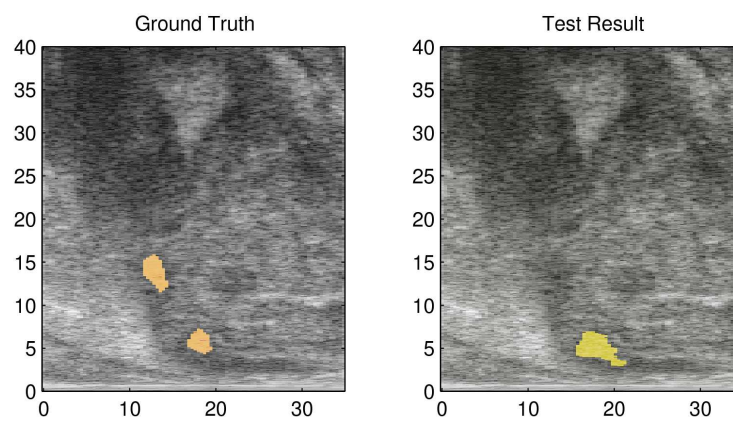
**Figure 5.10:** Example of the classification results displayed above the B mode prostate sagittal scans as visual guidance for biopsy (right panel) and ground truth for learning (left panel).



(a)



(b)



(c)

Figure 5.11: Example of the classification results displayed above the B mode prostate sagittal scans as visual guidance for biopsy (right panel) and ground truth for learning (left panel).

classified by a support vector machine classifier and the classification results are plotted on the B mode image as guidance information for biopsy.

The proposed method has been evaluated on a database of radio frequency signals recorded with commercial equipments which comprises 22 cases of prostate cancer and 15 cases of benign prostate pathologies. Since only partial information about the extension of cancerous areas in malignant cases were available, the main goal was to obtain a procedure able to identify most of the cancer sites and therefore, an high specificity.

The obtained results shows that the proposed method can identify most of the cancer foci with an high level of sensitivity ( $> 90\%$ ) and since most of the false positive are related to malignant cases, the lower value of specificity can be interpreted as an overestimation of cancers size.

Further development of this project can include:

- development of a procedure for automatic prostate boundary segmentation;
- employment of semi-supervised learning techniques in the training phase in order to compensate the partial information about pathological areas;
- evaluation of the proposed method on larger image databases in order to evaluate with higher accuracy its performance;
- evaluation of the proposed method for the computer aided detection of different pathologies;
- evaluation of the proposed method in a real clinical environment;

#### Publications

1. S. Caporale, A. Palladini, L. De Marchi, N. Speciale, G. Masetti: **Wavelet based algorithms for speckle removal form B-Mode images**. Proceeding of IASTED BIOMED 2004.
2. M. Scebran, A. Palladini, S. Maggio, L. De Marchi, N. Speciale: **Automatic regions of interests segmentation for computer aided classification of prostate TRUS images**. to be published in 30th International Symposium on Acoustical Imaging 2009.



---

# Bibliography

---

- [1] N. Archip, R. Rohling, P. Cooperberg, and H. Tahmasebpour. Ultrasound image segmentation using spectral clustering. *Ultrasound in Medicine & Biology*, 31(11):1485–1497, 2005. [cited at p. 84]
- [2] J. Awad. *Prostate Segmentation and Regions of Interest Detection in Transrectal Ultrasound Images*. PhD thesis, University of Waterloo, 2007. [cited at p. 82, 85]
- [3] O. Basset, Z. Sun, JL Mestas, and G. Gimnez. Texture analysis of ultrasonic images of the prostate by means of co-occurrence matrices. *Ultrasonic imaging(Print)*, 15(3):218–237, 1993. [cited at p. 90]
- [4] J. Besag. On the Statistical Analysis of Dirty Pictures. *JR Statist Soc. B*, 48(3):259–302, 1986. [cited at p. 84, 94, 95]
- [5] D. Boukerroui, A. Baskurt, J.A. Noble, and O. Basset. Segmentation of ultrasound images—multiresolution 2D and 3D algorithm based on global and local statistics. *Pattern Recognition Letters*, 24(4-5):779–790, 2003. [cited at p. 84]
- [6] D. Boukerroui, O. Basset, N. Guérin, and A. Baskurt. Multiresolution texture based adaptive clustering algorithm for breast lesion segmentation. *European Journal of Ultrasound*, 8(2):135–144, 1998. [cited at p. 84]
- [7] D. Boukerroui, O. Basset, N. Guerin, and A. Baskurt. Multiresolution texture based adaptive clustering algorithm for breast lesion segmentation. *European Journal of Ultrasound*, 8:135–144, 1998. [cited at p. 94]
- [8] D. Crivianu-Gaita, F. Miclea, A. Gaspar, D. Margineatu, and S. Holban. 3D reconstruction of prostate from ultrasound images. *International Journal of Medical Informatics*, 45(1-2):43–51, 1997. [cited at p. 83]
- [9] R. Szeliski et al. A comparative study of energy minimization methods for markov random fields. *In Proceedings of European Conference of Computer Vision (ECCV)*, pages 16–29, 2006. [cited at p. 96]
- [10] E.J. Feleppa, C.R. Porter, J. Ketterling, P. Lee, S. Dasgupta, S. Urban, and A. Kalisz. Recent Developments in Tissue-type Imaging (TTI) for Planning and Monitoring Treatment of Prostate Cancer. *Ultrasonic imaging*, 26(3):163, 2004. [cited at p. 90]
- [11] Y. Feng and G. Hamerly. Pg-means: learning the number of clusters in data. *In proceedings of the Twentieth Annual Conference on Neural Information Processing Systems (NIPS)*, pages 393–400, Dec. 2006. [cited at p. 93, 94]
- [12] A. Fenster and B. Chiu. Evaluation of segmentation algorithms for medical imaging. *Engineering in Medicine and Biology Society, 2005. IEEE-EMBS 2005. 27th Annual International Conference of the*, pages 7186–7189, 2005. [cited at p. 82]
- [13] R.C. Gonzalez and R.E.Woods. *Digital image processing*. Prentice Hall, 2nd edition, 1992. [cited at p. 63, 96]

- [14] G. Hamerly and C. Elkan. Learning the  $k$  in  $k$ -means. In *Proceedings of the Seventeenth Annual Conference on Neural Information Processing Systems*, pages 281–288, Dec. 2003. [cited at p. 93, 94]
- [15] AG Houston, SB Premkumar, DE Pitts, and RJ Babaian. Prostate ultrasound image analysis: localization of cancer lesionsto assist biopsy. In *Computer-Based Medical Systems, 1995., Proceedings of the Eighth IEEE Symposium on*, pages 94–101, 1995. [cited at p. 90]
- [16] T. Joachims. SVMLight: Support Vector Machine. *SVM-Light Support Vector Machine <http://svmlight.joachims.org/>*, University of Dortmund, 1999. [cited at p. 99]
- [17] H. Liu and L. Yu. Toward integrating feature selection algorithms for classification and clustering. *Transactions on Knowledge and Data Engineering*, 17(4):491–502, 2005. [cited at p. 98]
- [18] F.L. Lizzi, E.J. Feleppa, S. Kaiser Alam, and C.X. Deng. Ultrasonic spectrum analysis for tissue evaluation. *Pattern Recognition Letters*, 24(4-5):637–658, 2003. [cited at p. 92]
- [19] R. Llobet, J.C. Pérez-Cortés, A.H. Toselli, and A. Juan. Computer-aided detection of prostate cancer. *International Journal of Medical Informatics*, 76(7):547–556, 2007. [cited at p. 30, 34, 35, 30, 34, 35, 90, 97]
- [20] L. Masotti, E. Biagi, S. Granchi, L. Breschi, E. Magrini, and F. Di Lorenzo. Tissue differentiation based on radiofrequency echographic signal local spectral content. *Ultrasonics, 2003 IEEE Symposium on*, 1:1030–1033 Vol.1, Oct. 2003. [cited at p. 97]
- [21] T. McInerney and D. Terzopoulos. Deformable models in medical image analysis: a survey. *Medical Image Analysis*, 1(2):91–108, 1996. [cited at p. 85]
- [22] Samar S. Mohamed and Magdy M. A. Salama. Computer-aided diagnosis for prostate cancer using support vector machine. *Proceedings of the SPIE*, 5744:898–906, 2005. [cited at p. 90]
- [23] S.S. Mohamed and M.M.A. Salama. Spectral clustering for TRUS images. *BioMedical Engineering OnLine*, 6(1):10, 2007. [cited at p. 82, 84]
- [24] SS Mohamed and MMA Salama. Prostate Cancer Spectral Multifeature Analysis Using TRUS Images. *Medical Imaging, IEEE Transactions on*, 27(4):548–556, 2008. [cited at p. 84, 90]
- [25] M.D.G. Montoya, C. Gil, and I. García. The load unbalancing problem for region growing image segmentation algorithms. *Journal of Parallel and Distributed Computing*, 63(4):387–395, 2003. [cited at p. 83]
- [26] M. Moradi, P. Mousavi, and P. Abolmaesumi. Computer-Aided Diagnosis of Prostate Cancer With Emphasis on Ultrasound-Based Approaches: A Review. *Ultrasound in Medicine & Biology*, 33(7):1010–1028, 2007. [cited at p. 30, 34, 35, 30, 34, 35, 89, 92]
- [27] I. NetMed and N. Las Vegas. Artificial Neural Network Analysis (ANNA) of Prostatic Transrectal Ultrasound. *The Prostate*, 39:198–204, 1999. [cited at p. 90]
- [28] J.A. Noble and D. Boukerroui. Ultrasound Image Segmentation: A Survey. *IEEE Transaction on Medical Imaging*, 25(8):987, 2006. [cited at p. 82]
- [29] TN Pappas. An adaptive clustering algorithm for image segmentation. *Signal Processing, IEEE Transactions on [see also Acoustics, Speech, and Signal Processing, IEEE Transactions on]*, 40(4):901–914, 1992. [cited at p. 84, 94, 95]
- [30] SD Pathak, PD Grimm, and V. Chalana. Pubic arch detection in transrectal ultrasound guided prostatecancer therapy. *Medical Imaging, IEEE Transactions on*, 17(5):762–771, 1998. [cited at p. 83]
- [31] H. Peng, F. Long, and C. Ding. Feature Selection Based on Mutual Information: Criteria of Max-Dependency, Max-Relevance, and Min-Redundancy. *IEEE TRANSACTIONS ON PATTERN ANALYSIS AND MACHINE INTELLIGENCE*, pages 1226–1238, 2005. [cited at p. 98]

- [32] D.L. Pham, C. Xu, and J.L. Prince. Current methods in medical image segmentation. *Annual Reviews in Biomedical Engineering*, 2(1):315–337, 2000. [cited at p. 82, 85]
- [33] JS PRATER and WD RICHARD. Segmenting ultrasound images of the prostate using neural networks. *Ultrasonic imaging(Print)*, 14(2):159–185, 1992. [cited at p. 84, 85]
- [34] U. Scheipers. *Sonohistology: Methods and Systems for Ultrasonic Tissue Characterization Based on a Multifeature Approach and Fuzzy Inference Systems*. Logos-Verl., 2004. [cited at p. 89]
- [35] U. Scheipers, H. Ermert, HJ Sommerfeld, M. Garcia-Schurmann, T. Senge, and S. Philippou. Ultrasonic multifeature tissue characterization for prostate diagnostics. *Ultrasound Med Biol*, 29(8):1137–49, 2003. [cited at p. 17, 90, 92]
- [36] G. Schmitz, H. Ermert, and T. Senge. Tissue-characterization of the prostate using radio frequencyultrasonic signals. *Ultrasonics, Ferroelectrics and Frequency Control, IEEE Transactions on*, 46(1):126–138, 1999. [cited at p. 17, 90, 92]
- [37] JPM Sedelaar, J. de la Rosette, HP Beerlage, H. Wijkstra, FM Debruyne, and RG Aarnink. Transrectal ultrasound imaging of the prostate: review and perspectives of recent developments. *Prostate Cancer and Prostatic Diseases*, 2(5-6):241–252, 1999. [cited at p. 35, 83]
- [38] PM Shankar, VA Dumane, CW Piccoli, JM Reid, F. Forsberg, and BB Goldberg. Classification of breast masses in ultrasonic B-mode images using a compounding technique in the Nakagami distribution domain. *Ultrasound Med Biol*, 28(10):1295–300, 2002. [cited at p. 53, 92]
- [39] T.L Szabo. *Diagnostic ultrasound imaging*. Elsevier, 2004. [cited at p. 17, 19, 17, 19, 89]
- [40] S. Theodoridis and K. Koutroumbas. *Pattern Recognition*. Academic Press, 2006. [cited at p. 93]
- [41] R. Tibshirani, G. Walther, and T. Hastie. Estimating the number of clusters in a dataset via the gap statistic. *Journal of the Royal Statistical Society, Series B*, 63, No. 2:411–423, 2001. [cited at p. 83, 84, 94, 98, 99]
- [42] M.K. Varanasi and B. Aazhang. Parametric generalized Gaussian density estimation. *The Journal of the Acoustical Society of America*, 86:1404, 1989. [cited at p. 92]
- [43] U. von Luxburg. A tutorial on spectral clustering. *Statistics and Computing*, 17(4):395–416, 2007. [cited at p. 84]
- [44] T. Wagner. Texture Analysis. *Handbook of Computer Vision and Application, Academic Press, San Diego*, pages 275–308, 1999. [cited at p. 92, 97]
- [45] Y. Zhan, D. Shen, J. Zeng, L. Sun, G. Fichtinger, J. Moul, and C. Davatzikos. Targeted Prostate Biopsy Using Statistical Image Analysis. *IEEE TRANSACTIONS ON MEDICAL IMAGING*, 26(6):779, 2007. [cited at p. 85]
- [46] Y. Zhu, S. Williams, and R. Zwigelaar. Computer technology in detection and staging of prostate carcinoma: A review. *Medical Image Analysis*, 10(2):178–199, 2006. [cited at p. 34, 35, 34, 35, 85]



## Chapter 6

---

# Primate behavioural tasks modelling

---

The goal of this project, developed at the Laboratory of Nonlinear Systems (LANOS) of the Polytechnical federal School of Lausanne - Switzerland, was to build up a simplified neural microcircuit model, to support different conclusions derived from the machine learning based analysis presented in [1]. Such analysis was motivated by the study on the neural activity in parietal area 7a (inferior parietal lobule of the posterior parietal cortex) of trained monkeys performing several eye-hand directional motor tasks, presented in [2] and [3] and reviewed in chapter 3. Data analysis procedures rely on the hypothesis that even if the available recordings are too limited to extract precise motor information, it could be possible to read motor intention from the set of simultaneously recorded spike trains, by combining information from all the available recordings. Unfortunately, the available recording sets were too limited and the results obtained strongly depend on the available data and on the window size used for the computation of the spiking rate.

**Author contributes.** In order to assess the effect on classification performance of the number of available recordings and of the window size, an abstract model able to learn an abstract representation of some of the behavioural tasks presented in [2] and [3] was built. Such model was built following a liquid state machine (LSM) approach [12][20]. Although the models employed were very simple, the number of parameters to be tuned is quite high and at the moment, no simple design strategies are available for LSM. Thus, following the approach proposed in [5], biologically motivated settings for some model parameters were adopted in order to simplify the network design and its training procedure. Following this approach, we developed a tuning procedure that allowed the design of artificial neural microcircuits able to learn correctly abstract representations of the real behavioural tasks.

### 6.1 Third generation neural networks and liquid state machines

The task of understanding the principles of information processing in the brain poses, apart from numerous experimental questions, challenging theoretical problems on all levels of modelling, from molecules to behaviour. Advanced models of the human brain present it as a recurrent neural network (RNN): a network of neurons with feedback connections. This type of neural network can learn many behaviours/sequence processing tasks, algorithms and programs that are not learnable by traditional machine learning methods. Moreover

RNN are computationally more powerful and biologically more plausible than other adaptive approaches such as Hidden Markov Models (no continuous internal states), feedforward networks and Support Vector Machines (no internal states at all). Recent applications of RNN include adaptive robotics and control, handwriting recognition, speech recognition, keyword spotting, music composition, attentive vision, protein analysis, stock market prediction, and many other sequence problems. All these considerations explain the rapidly growing interest in artificial RNNs for technical applications: general computers which can learn algorithms to map input sequences to output sequences, with or without a teacher.

However, the main drawback of RNN is the complex training procedure, often task dependent. Various algorithms like back-propagation through time and real-time recurrent learning have been proposed to train RNNs; however all these algorithms suffer of computational complexity, resulting in slow training, complex performance surfaces, instability and decay of performances according to the network topology and complexity.

To overcome this problem Jaeger [13] and Maas [20] introduced independently a new training paradigm for RNN named Echo State Network (ESN) and Liquid State Machine (LSM) respectively. While ESN have been introduced with the purpose of developing a simpler and more powerful training paradigm for RNN of sigmoidal neurons, LSM have been introduced aiming to realistic model of information processing in biological system; thus the latter approach uses more sophisticated models for spiking neurons and chemical synapses.

In this chapter we will present the mathematical models employed in the present work to build recurrent neural networks of spiking neurons (SRNN) and train them with the ESN/LSM approach. Such paradigm will be used in the present work to build a toy model.

## Neurons

Detailed conductance-based neuron models can reproduce electrophysiological measurements with an high degree of accuracy, but because of their intrinsic complexity these model cannot be easily analyzed and employed to build neural network for engineering computational purposes [9].

For these reason, simple phenomenological spiking neurons models are usually employed. In the present work we will adopt a formal threshold model of neuronal firing, and in particular the Leaky Integrate and Fire (LIF) model, which is the simplest model for spiking neurons.

The leaky integrator model basically consists of a parallel of capacitor  $C$  and a resistor  $R$ , driven by a current  $I(t)$ . Thus the membrane potential of the neuron  $u(t)$  is ruled by the following dynamic eq.:

$$\tau_m \frac{du}{dt} = -u(t) + RI(t) \quad (6.1)$$

where  $\tau_m = RC$  is the leaky integrator time constant.

A spike event is then formally described by firing time  $t^{(f)}$ , defined by the threshold criterion

$$t^{(f)} : u(t^{(f)}) = \theta. \quad (6.2)$$

Immediately after a spike event  $t^{(f)}$ , the membrane potential is reset to a new value  $u_r < \theta$  and the dynamic (6.1) is forced to the reset value during an absolute refractory time  $\tau_r$ . At the end of the refractory time  $\tau_r$  the integration restart with the new initial condition  $u(t^{(f)} + \tau_r^+) = u_r$ .

The combination of the leaky integrator dynamic (6.1) and reset (6.2) define the LIF neuron model. In case the neuron is stimulated by a constant current  $I(t) = I_0$ , the trajectory of the membrane potential after a spike has occurred at  $t = t^{(1)}$ , with  $u_r = 0$ , is given by

$$u(t) = RI_0 \left[ 1 - \exp \left( -\frac{t - t^{(0)}}{\tau_m} \right) \right] \quad (6.3)$$

For  $t \rightarrow \infty$  the membrane potential tends to  $RI_0$ . For  $RI_0 < \theta$  no spikes will occur, while for  $RI_0 \geq \theta$  a spike will occur at time  $t^{(2)} = t^{(1)} + T$  where

$$T = \tau_m \ln \frac{RI_0}{RI_0 - \theta}. \quad (6.4)$$

Therefore the neuron firing rate can be defined as

$$R = \frac{1}{T + \tau_r} = \left[ \tau_r + \tau_m \ln \frac{RI_0}{RI_0 - \theta} \right]^{-1}. \quad (6.5)$$

Since  $T \rightarrow 0$  for  $RI_0 \rightarrow \infty$ , the maximum firing rate is therefore  $R_M = 1/\tau_r$ .

In a network context, the input current of the neuron can be thought as the sum of two different terms: an internal constant current  $J$ , due to self-induction effect present in the neuron, an external current  $I_{ext}(t) = I_i(t) + I_e(t) + I_n(t)$  due to the current induced by the input synapses  $I_i(t)$ , external analog inputs  $I_e(t)$  and to diffusive noise  $I_n(t)$ [9] (where  $I_n(t)$  is a white zero mean Gaussian noise).

### Synapses

In a network context the input current  $I_i(t)$  is generated by the activity of pre-synaptic neurons, namely all the neurons which output is connected to the considered neuron through a synapse.

In the framework of LIF model, each pre-synaptic spike generates a post-synaptic current pulse, which will excite all the neurons connected to it through the different synapses. These synapses will be called *spiking synapses* in order to distinguish them from the synapses that are inducing the external current  $I_e(t)$ , here called *analog synapses*.

The total input current to a neuron  $i$  due to pre-synaptic activity is therefore modelled as:

$$I_i(t) = \sum_{j,g} w_{ij}(t - t_i^{(g)}) \sum_f \alpha_{ij}(t - t_j^{(f)}) \quad (6.6)$$

where  $\alpha_{ij}(t - t_j^{(g)})$  are the synapses current pulses,  $w_{ij}(t - t_j^{(g)})$  are the synaptic weights and  $t_j^{(g)}$  are the spike instants of neuron  $j$ .

In general, as indicated in (6.6), the synaptic weights  $w_{ij}$  can be dependent by all the spiking times  $t_i^{(g)} < t$ . In this case we will call the synapses *dynamic spiking synapses*. This type of dynamic modification of synaptic weights is a short-term effects and it should not be confused with the long-term dynamic modification of synaptic weights induced by synaptic plasticity. Short term dynamic modification of synaptic weight has been evidenced by a large number of experimental studies [24].

In the other hand, when the synaptic weights are not dependent by all the spiking times  $t_i^{(g)} < t$  we will call the synapses *static spiking synapses*.

**Dynamic synapse model.** In this work we will employ the dynamical synapse model presented in [24] and derived from the results presented in [22]. In this model, the synaptic weight of each synapse is modified for each incoming spike  $g$  at time  $t^{(g)}$  according to following discrete-time dynamical model:

$$\begin{aligned} w_{ij}^g &= w_{ij} \cdot u_g \cdot R_g \\ u_g &= U + u_{g-1}(1 - U) \exp(-\Delta_{g-1}/F) \\ R_g &= 1 + (R_{g-1} - u_{g-1}R_{g-1} - 1) \exp(-\Delta_{g-1}/D) \end{aligned} \quad (6.7)$$

where  $\Delta_k = t^{(k)} - t^{(k-1)}$  are the inter-spike intervals,  $F$  and  $D$  are the model parameters and  $u_1 = U$  and  $R_1 = 1$  the initial conditions.

**Post-synaptic current.** For both static and dynamic spiking synapses a relatively simple and quite realistic model for the post-synaptic current pulses is the following

$$\alpha_{ij}(s) = \frac{q}{\tau_s^{ij} - \tau_t^{ij}} \left[ \exp\left(-\frac{s - \Delta^{ij}}{\tau_s^{ij}}\right) - \exp\left(-\frac{s - \Delta^{ij}}{\tau_t^{ij}}\right) \right] \theta(s - \Delta^{ij}) \quad (6.8)$$

where  $\tau_s^{ij}, \tau_t^{ij}$  and  $\Delta^{ij}$  are the pulse decay time constant, pulse rise time constant and propagation delay constant of synapse  $ij$  respectively, and  $q$  is a normalization constant (for  $q = \exp(1)$  the maximum value of  $\alpha(s)$  will be 1).

Such model can be simplified imposing  $\tau_t \rightarrow \tau_s$  in eq. (6.8), obtaining

$$\alpha_{ij}(s) = q \frac{s - \Delta^{ij}}{(\tau_s^{ij})^2} \exp\left(-\frac{s - \Delta^{ij}}{\tau_s^{ij}}\right) \theta(s - \Delta^{ij}) \quad (6.9)$$

### Complete model

The complete model for LIF neuron excited by spiking synapses, external analog inputs, self-induction current and noise is therefore

$$\tau_m \frac{du_i}{dt} = -u_i(t) + R \left[ \sum_{j,g} w_{ij}(t - t_i^{(g)}) \sum_f \alpha_{ij}(t - t_j^{(f)}) + I_e(t) + I_n(t) + J_i \right]. \quad (6.10)$$

Since in general in a network neurons have the same time constant  $\tau_m$  and the same resistance  $R$ , we can rewrite eq. (6.10) in an equivalent form, introducing the equivalent synaptic weights  $w'_{ij}$ , the external potential  $U_e(t)$ , the noise potential  $I_n(t)$  and the self-induction potential  $E_i$ :

$$\tau_m \frac{du_i}{dt} = -u_i(t) + \sum_{j,g} w'_{ij}(t - t_i^{(g)}) \sum_f \alpha_{ij}(t - t_j^{(f)}) + U_e(t) + U_n(t) + E_i, \quad (6.11)$$

thus reducing the number of the parameters.

### Model discretization

In order to integrate the eq.(6.11) we must discretize it and apply numerical integration methods. Since the model is quite simple, it can be integrated with sufficient accuracy by one-step Euler method.

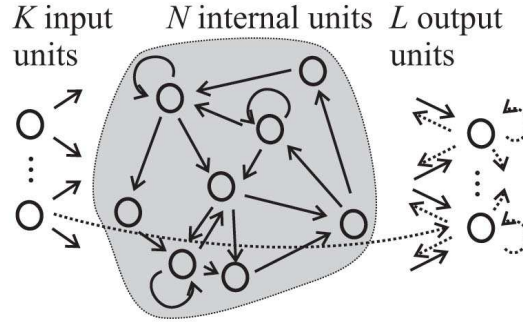


Figure 6.1: ESN architecture (figure taken from [13]).

Defining a sampling step  $\delta$  such that  $t_n - t_{n-1} = \delta$  and applying Euler numerical integration method, we obtain the following discrete-time equivalent model:

$$\begin{aligned}
 U_i(t_{n+1}) = & u_i(t_n) \left( 1 - \frac{\delta}{\tau_m} \right) \\
 & + \frac{\delta}{\tau_m} \left[ \sum_j w'_{ij}(t_{n+1} - t_i^{(f)}) \sum_f \alpha_{ij}(t_{n+1} - t_j^{(f)}) \right. \\
 & \left. + U_e(t_{n+1}) + U_n(t_{n+1}) + E_i \right]
 \end{aligned} \tag{6.12}$$

### Network architecture

In the following section we will show how it is possible to build recurrent neural networks of spiking neurons, in order to employ an ESN learning approach. The ESN (of LSM) training approach [13] consist in building recurrent neural networks of either analog or spiking neurons, organized with a special topology, shown in figure. The network is composed of three main sub-network: an input network composed by a single layer of neurons, an internal unit usually called *reservoir* and an output layer composed by a single layer of neurons.

**Input layer.** The input layer acts like a converter of the input signals and as an interface with the reservoir layer and its mad of spiking neurons. The input signals, which can be both spike trains and analog signal, are converted in spike trains and transmitted to the reservoir by means of static spiking synapses. The input layer is completely characterized by:

- synaptic weights  $[N \times K]$  matrix  $\underline{W}_{in}$ ;
- synapses time constants  $[N \times K]$  matrix  $\underline{\tau}_{in}$ ;
- synapses transmission delays  $[N \times K]$  matrix  $\underline{\Delta}_{in}$ ;
- neurons self induction potentials  $[1 \times K]$  vector  $\underline{E}_{in}$ ;

**Reservoir layer.** In the present work, the reservoir is a recurrent neural network of  $N$  spiking neurons interconnected with either static or dynamic spiking synapses. The reservoir is therefore completely characterized by:

- synaptic weights  $[N \times N]$  matrix  $\underline{W}$ ;
- synapses time constants  $[N \times N]$  matrix  $\underline{\tau}$ ;
- synapses transmission delays  $[N \times N]$  matrix  $\underline{\Delta}$ ;
- dynamic synapses parameters  $[N \times N]$  matrixes  $\underline{E}$ ,  $\underline{D}$  and  $\underline{U}$ ;
- neurons self induction potentials  $[1 \times N]$  vector  $\underline{\tilde{E}}$ ;

**Output layer.** The output layer act as a filter that converts spikes incoming from the reservoir in analog values and is therefore made of analog neurons connected to the reservoir through static spiking synapses. The output layer is completely characterized by:

- synaptic weights  $[L \times N]$  matrix  $\underline{W}_{out}$ ;
- synapses time constants  $[L \times N]$  matrix  $\underline{\tau}_{out}$ ;
- synapses transmission delays  $[L \times N]$  matrix  $\underline{\Delta}_{out}$ ;

As defined independently in [13] and [20], the ES approach to RNN train consist in randomly generate, according to some criteria, the input layer and reservoir parameters and training only the parameters for the output layer. In the next chapter we will illustrate the dynamical properties and the theoretical computational performances of this approach, proving its generality and giving some measure to quantify experimentally the computational performance of this architecture with respect to some class of tasks.

## 6.2 Proposed model

### 6.2.1 Behavioural tasks modelling and information representation

Among the possible experimental behavioural tasks described in [2] and [3], summarized in chapter 3.2, we focused our attention on the modelling of the reach task (RT) and of the no-go task (NGT), since these are the simpler tasks that require only short-term memory to be solved, leaving as further possible developments the modelling of more complex tasks like memory tasks.

The model adopted for the behavioural task modelling is a recurrent neural network that, designed with a LSM approach, will be trained in order to correctly solve abstract representations of the behavioural tasks RT and NGT. The first goal of the training procedure is to develop a network that is able to encode through its dynamic the spatial information incoming from the input layer, in order to be able to manifest the intention of moving towards a specific direction. The second and more demanding requirement is to integrate along time the visual stimulus provided by the input layer (central target followed by a peripheral target), in order to manifest correctly moving intention towards a specific direction only in presence of a specific sequence of inputs. Both the training and the test dataset must be designed in order to verify the fulfilment of these properties.

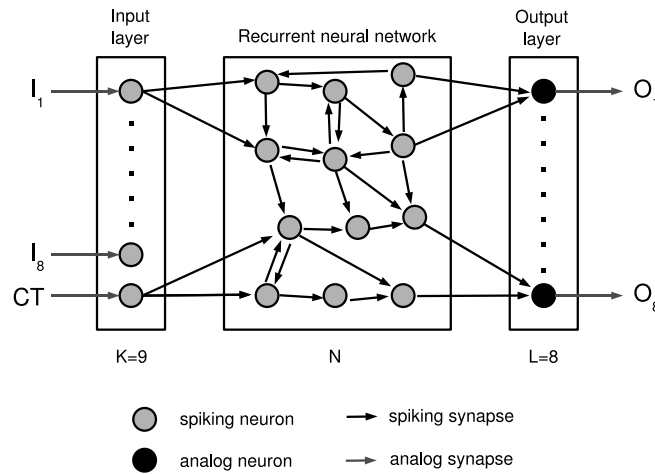


Figure 6.2: Schematic representation of the toy model network architecture.

The structure of the network is the one shown in fig. 6.2. As in LSM approach, the network is organized in three layers: an input layer, an internal (recurrent) layer and an output layer. The input layer comprises nine different analog inputs, one for each of the eight possible peripheral targets and for the central target. The output layer comprises eight analog outputs, one for each possible direction of movement.

**Information encoding.** The information that we want to represent is the activations of input targets and the activations of the movement commands towards the different possible directions. Since both input and output of the network are analog signals, the activation of a specific input or output during a time interval  $T$  was represented with a continuous pulse of current with unitary amplitude, while the inhibition of a with a zero level, as shown in fig. 6.3.

A behavioral RT was therefore represented as the activation of the start signal ( $CT$ ) of random duration  $T_s$ , followed immediately by the activation of a target signal ( $PT_1, \dots, PT_8$ ) of duration  $T_t$ . The exact values for  $T_s$  and  $T_t$  are randomly chosen with uniform probability above two intervals  $[T_{s1} T_{s2}]$  and  $[T_{t1} T_{t2}]$ . The desired output corresponds to the activation of only the output correspondent to the activated input and it was represented as a pulse of the same length and synchronized with it, as shown in fig. 6.4.

To assure that the network correctly ingrate along time the information presented, it is necessary to include into the training and test data sets examples of NGT. Due to the representation of the input information (no task encoding information is present), such tasks couldn't be modelled exactly as real behavioural tasks described in section 3.2. Thus, NGT were represented as tasks in which the central target before the peripheral target is missing (see fig. 6.5). The training data set and the test data set must include several examples of different duration of all the possible real and fake targets. An example of a complete set of tasks is shown in fig. 6.6).

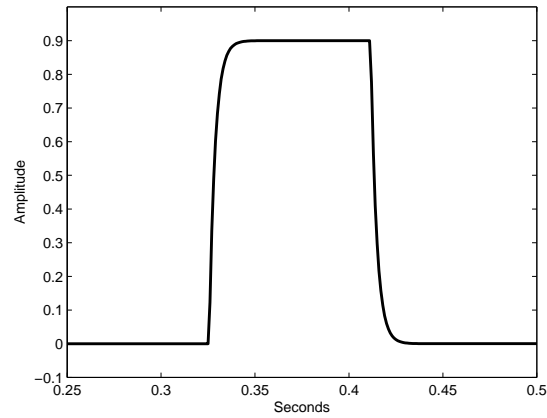


Figure 6.3: Activation of input/output of the network represented as a current pulse.

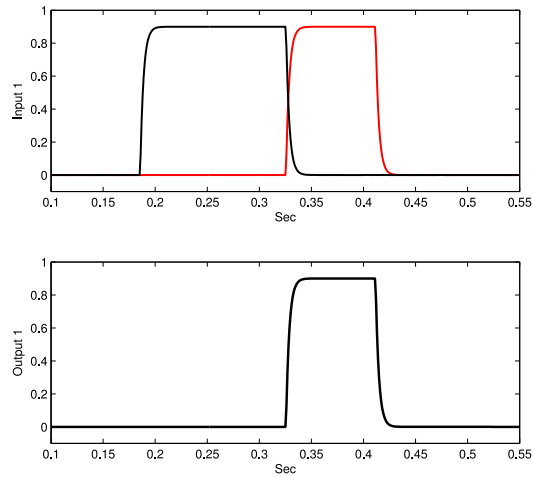
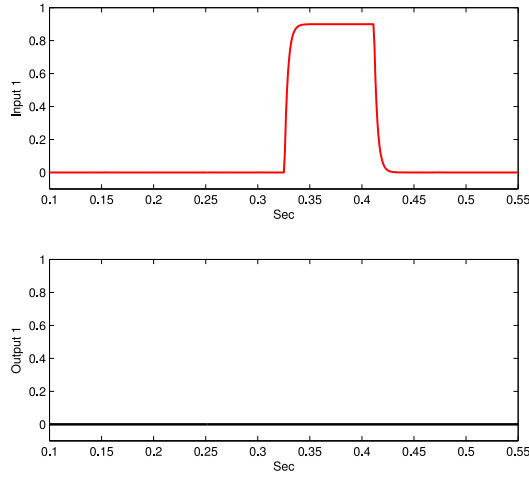


Figure 6.4: Representation of a reach task (RT) as a sequence of activation of the central target (continuous line) and activation of a peripheral target (dotted line) and correspondent desired output.

## 6.2.2 Network architecture

**Input Layer.** The input layer is an abstract representation of the information coming from the visual cortex, i.e., the activation of one of the eight possible peripheral targets ( $PT_1, \dots, PT_8$ ) and of the central target (CT). Since the activation of the different target is encoded in an analog current value that must be converted in spike trains, the input layer is constituted of nine excitatory LIF neurons, each of them connected to only one input. Therefore each neuron acts like a current to spikes converter. This conversion is realized injecting directly the input currents into the neurons through analog synapses. Since no spiking synapses are present, the mathematical model of the input neurons is described by



**Figure 6.5:** Representation of a no-go task (NGT) as activation of a peripheral target (dotted line) without the activation of the central target and correspondent desired output.

the eq.

$$\tau_{in} \frac{du_i}{dt} = -u_i(t) + w_{inj} R l_i(t), \quad 1 \leq i \leq 9 \quad (6.13)$$

obtained from (6.10) adding a time dependent input current  $l_i(t)$  scaled by a factor  $w_{inj}$ , and neglecting both the spiking synapses and the noise term. The noise term was neglected since the input neurons purely act like converters from the input information representation, analog values, to the recurrent neural network information representation, spike events. Indeed, in neural modelling noise take into account both statistic nature of neurons behaviour and stimulus coming from unknown sources. Both of these effects will be considered in the model of the recurrent neural network neurons adding an escape noise term.

The results of this conversion are spike trains that are transmitted from the input layer to the recurrent neural network through static spiking synapses, whose post-synaptic potential is described by eq. 6.9 and whose connection topology and strength are defined by the connection matrix  $\underline{W}_{in} = \{w_{ij}^{in}\} \geq 0$ . In conclusion, the input layer is completely defined by:

- scaling factor of input analog synapses  $w_{inj}$ ;
- synaptic weights  $[N \times 9]$  matrix  $\underline{W}_{in}$ ;
- synapses time constants  $[N \times 9]$  matrix  $\underline{\tau}_{in}$ ;
- synapses transmission delays  $[N \times 9]$  matrix  $\underline{\Delta}_{in}$ ;
- neurons time constant  $\tau_{in}$  and threshold  $\theta_{in}$ ;

that we will indicate with the notation  $\mathcal{N}_{in} = \{\underline{W}_{in}, \underline{\tau}_{in}, \underline{\Delta}_{in}, \tau_{in}, \theta_{in}\}$ .

**Recurrent network.** The recurrent neural network is an abstract representation of the neural circuits responsible for spatial information representation and temporal information integration in area 7a of the parietal cortex. As revealed by neurophysiologic studies,

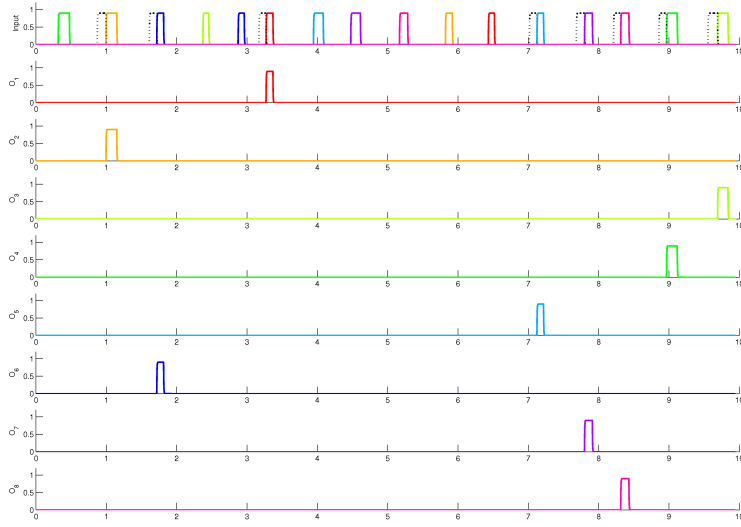


**Figure 6.6:** Example of input and output signals for complete set of real and fake task. The different target position are represented with different colors, while the star signal is represented with dotted line.

the 7a area of the parietal cortex is responsible of the integration of visual perception of the space and movement control and its cells exhibit directional tuning properties both an single cell and populations of cells level [2][3]. The data analysis procedures presented in [1] revealed the possibility of extracting motor intention from the neural activity of trained monkey performing behavioural task involving hand and eyes coordinated movements.

Therefore, the toy model should be able to capture both the temporal information integration property and the directional tuning property. These properties require a spatially organized and specialized network endowed of short term memory property [12]. For these reasons, we decided to employ a recurrent neural network of LIF neurons connected through static spiking synapse, with fading memory property, that will be trained with an ESN/LSM approach.

The RNN is composed of  $N$  LIF neurons from which  $N_E$  are excitatory and  $N_I$  are inhibitory. The excitatory and inhibitory populations of neurons are described respectively by

- synaptic weights  $[N \times N_E]$  matrix  $\underline{W}_E$ ;
- synapses time constants  $[N \times N_E]$  matrix  $\underline{\tau}_E$ ;
- synapses transmission delays  $[N \times N_E]$  matrix  $\underline{\Delta}_E$ ;
- neurons time constant  $\tau_E$ , threshold  $\theta_E$  and self induction potentials  $[1 \times N_E]$  vector  $\vec{E}_E$ ,

that we will indicate with the notation  $\mathcal{N}_E = \{\underline{W}_E, \underline{\tau}_E, \underline{\Delta}_E, \tau_E, \theta_E\}$  and by

- synaptic weights  $[N \times N_I]$  matrix  $\underline{W}_I$ ;

- synapses time constants  $[N \times N_I]$  matrix  $\underline{\tau}_I$ ;
- synapses transmission delays  $[N \times N_I]$  matrix  $\underline{\Delta}_I$ ;
- neurons time constant  $\tau_I$ , threshold  $\theta_I$  and self induction potentials  $[1 \times N_I]$  vector  $\bar{E}_I$ ,

that we will indicate with the notation  $\mathcal{N}_I = \{\underline{W}_I, \underline{\tau}_I, \underline{\Delta}_I, \tau_E, \theta_I\}$ .

**Output layer.** The output layer is an abstract representation of an hypothetic cortical brain area connected to the RNN which try to extract the information encoded by it and tries to express the intention of moving in a particular direction, according to the given visual stimulus.

The layer is constituted by eight analog linear neurons, one for each possible target position, connected via static spiking synapses to the RNN. Each neuron simply performs a linear combination (readout) of the activity of the RNN, according to

$$U_i^{out}(t) = R \sum_j w_{ij}^{out} \sum_f \alpha^{out}(t - t_j^{(f)}) \quad (6.14)$$

where

$$\alpha^{out}(t) = q \frac{t - \Delta_{out}}{(\tau_{out})^2} \exp\left(-\frac{t - \Delta_{out}}{\tau_{out}}\right) \theta(t - \Delta_{out}) \quad (6.15)$$

is the kernel that converts spikes into potentials. The internal potential is finally transmitted through analog synapses to the eight output  $(MT_1, \dots, MT_8)$ .

The output layer is completely defined by:

- synaptic weights  $[8 \times N]$  matrix  $\underline{W}_{out}$ ;
- synapses time constant  $\tau_{out}$ ;
- synapses transmission delay  $\Delta_{out}$ .

The synaptic weights matrix  $\underline{W}_{out}$  will be computed in the training phase of the network according to the problem to be solved (regression or classification), while all the parameters of the input layer and of the recurrent neural network will be tuned in order obtain the desired performances.

### 6.2.3 Model parameters tuning and network training

The model is completely defined by the set of parameters  $\mathcal{N}_{in}, \mathcal{N} = \{\mathcal{N}_E, \mathcal{N}_I\}, \tau_{out}, \Delta_{out}$ , and  $\underline{W}_{out}$ . Since we adopted the LSM training paradigm, only the output layer will be tuned through the training procedure in order to obtain the desired performance. Both the input layer and the recurrent neural network parameters will be fixed, according to some design criteria, to obtain the desired properties and performances, indeed the short term memory property necessary to correctly classify all the possible tasks.

Several studies investigating analytical properties of ESN, analytical conditions for short term memory and different design strategies are available [19][14]. The strategies developed so far can be divided in three main categories:

- GENERAL: methods/guidelines to generate good reservoirs without regarding of the task.

- UNSUPERVISED: pre-training of the reservoir with respect to the given input;
- SUPERVISED: pre-training of the reservoir with respect to both the given input and the desired output.

Since in the proposed model both input and output signal are an abstract representation of the real behavioural tasks and no detailed information about the real representation in the brain of the visual stimuli and motor command are available, the design paradigms that can be employed for our purposes belong to the first class. Moreover, since no information about the real structure of the 7a brain area and about how its topology is influenced by training are available, among the possible approach belonging to this class, the random generation approach seems to be the more suitable for a preliminary study [14].

In LSM, the number of parameter to be tuned is bigger and the dynamical behaviour of the model more complex, thus general design strategies are still lacking. Despite the lack of general design paradigms, in [18] an analytical proof of LSM approximation properties and a quantitative measure for evaluating LSM computational are given. Moreover, LSM were successfully applied to real problem like movement prediction from images [5]. In that work, the network parameters were tuned according to experimental evidences exposed in [10] and [26]. Although these models are still only a rough approximation of a real neural microcircuit, they take into account some important features observed in biological neural networks like synaptic depression and facilitation [10], the columnar functional organization and the connectivity ratio between different layers of the neocortex [26]. Synaptic depression and facilitation are modelled through the dynamical model of synaptic weights 6.7, whose parameters are chosen according to the data reported in [10]. Columnar organization and connectivity are modelled organizing the neural microcircuit as a 3D structure and randomly generate the connectivity matrix with the following probability of connection between two neurons  $i$  and  $j$

$$p(i, j) = Ce^{-\frac{D(i, j)}{\lambda^2}} \quad (6.16)$$

where  $D(i, j)$  is the distance between the neurons  $i$  and  $j$ ,  $C$  is a parameter depending on the connection type (excitatory or inhibitory) and  $\lambda$  is the connection probability parameter.

**Neurons parameters.** In the present work, following the approach proposed in [5], we adopted biologically realistic settings for neurons and synapses parameters but we didn't take into account the depression/facilitation effect in synapses, since we used the static model in order to simplify the tuning procedure.

For neurons parameters we chose to keep constant inside all the network layers the following

- membrane time constant  $\tau_m = 30$  ms;
- leakage resistance  $R = 10$  M $\Omega$ ;
- spiking threshold  $\theta = 15$  mV;
- refractoriness time constant for excitatory neurons  $\tau_r = 3$  ms;
- refractoriness time constant for inhibitory neurons  $\tau_r = 2$  ms;
- diffusive noise variance  $\sigma_n = 5$  mV;

and to generate randomly the following

- autoinjection current uniformly distributed on [13.5 14.5] nA;
- reset potential uniformly distributed on [13.5 14.5] mV.

The membrane time constant defines the neurons memory. Compared to the duration of the toy model tasks (from 130 ms to 310 ms) neurons memory is too small to correctly solve them and network integration is therefore mandatory. Refractoriness time limits the maximum spiking frequency of excitatory and inhibitory neurons to 333 Hz and 500 Hz, respectively. All the other model parameters are set individually with different criteria for each layer.

**Input layer.** Input layer mainly act just like a rate to spikes train converter and is therefore formed only by excitatory neurons. The only requirement is a proper mapping of the input dynamic range on neurons spiking rate. This condition is assured by the input current levels that, compared to leakage resistance, neurons threshold and input current scaling, is set to obtain a spike rate which is close to the maximum, in correspondence of an input activation. The second function of this layer is the transmission of the input signal into the recurrent network and it is realized by the synapses whose parameters were generated according to the following settings

- connections topology: randomly generated to obtain a connectivity of 20 % for each input neuron;
- connections strength: equal for all the synapses,  $\underline{W}_{in} = w_{in} = 10^{-2}$ ;
- synapses time constants: randomly generated with uniform distribution on [2.5 3.5] ms;
- synapses transmission delays: randomly generated with uniform distribution on [.1 1] ms.

Since the synapses time constants are one order of magnitude smaller than neurons membrane time constant, according to the consideration exposed in [17], the neurons of the recurrent network will operate as integrator rather than coincidence detectors with respect to the signal coming from the input layer.

**Recurrent network.** The design of this part of the network is critical for the achievement of the desired properties and performance: the richer will be its dynamical behaviour the better will be the overall network performance. The main goal is to obtain the larger short term memory achievable while keeping the echo state property. Unfortunately, there are no design criteria available in literature. In order to simplify the tuning procedure, we reduce the number of parameter to be tuned adopting again some biological motivated values for most of them. In particular we set

- 80 % of the neuron are excitatory and 20 % are inhibitory;
- connections topology: randomly generated to obtain a connectivity of 20 % for each neuron;

- connections strength for inhibitory neurons: randomly generated with Gaussian distribution, mean value  $W_{mI} = -2W_{mE}$  and root mean square  $\sigma = W_{mE} \cdot 10^{-3}$ ;
- excitatory neurons synapses time constants: randomly generated with uniform distribution on [2.5 3.5] ms;
- excitatory neurons synapses time constants: randomly generated with uniform distribution on [5 7] ms;
- synapses transmission delays: randomly generated with uniform distribution on [.1 1] ms for both excitatory and inhibitory neurons.

Once again, since the synapses time constants are one order of magnitude smaller than neurons membrane time constant, the neurons of the recurrent network will operate as integrator also with respect to the spikes coming from the internal connections.

The design strategy for the recurrent layer adopted in the present work is quite different from the one employed in [5]. In our approach the network is generated with an unstructured fashion, imposing only a sparsity criteria and the only parameter to be tuned is the average value for connection strength  $W_{mE}$

**Output layer.** The output layer simply acts like a kernel that converts the spikes coming from the neurons of the recurrent layer into potential and sum them. Neurons of the output layer are connected with all the neurons of the recurrent network through spiking synapses whose connection strengths are tuned by the training procedure. The remaining parameters were set as

- synapses time constants: equal for all the synapses,  $\tau_{out} = \tau_{out} = 20$ ; ms;
- synapses transmission delays: equal for all the synapses,  $\Delta_{out} = \Delta_{out} = 0$  ms.

Once the network parameters are generated, the only parameter to be tuned is the average connection strength for the excitatory connections  $W_{mE}$ . To tune such parameter we performed a grid search randomly generating a number of networks sufficiently big to evaluate its effect on networks performance. In particular we wanted to maximize the number of networks that have at least 6 output with a classification error lower or equal to 10% (operating output). Thus, after networks were generated, we trained the respective output coefficients matrixes  $\underline{W}_{out}$  with a linear regression with respect to the desired outputs matrix of the training set  $\underline{y}_d$ :

$$\underline{W}_{out} = \underline{U}^{-1} \underline{y}_d \quad (6.17)$$

where  $\underline{U}^{-1}$  is the pseudoinverse of the matrix  $\underline{U}$ , which rows are the time evolution of the network internal states

$$U_i(t) = \sum_f \alpha_{ij}^{out}(t - t_i^f) \quad (6.18)$$

computed for different time instant  $t_n$  feeding the network with the training set input, as shown in fig. 6.7.

The output pulses classification is then realized computing the pulses energy and comparing it with a fixed threshold value  $\sigma$ : all the output pulses whose energy is above threshold will be classified as activation of the output and viceversa as no activation, as shown in fig. 6.7. Finally, classification error for each network output is computed and the

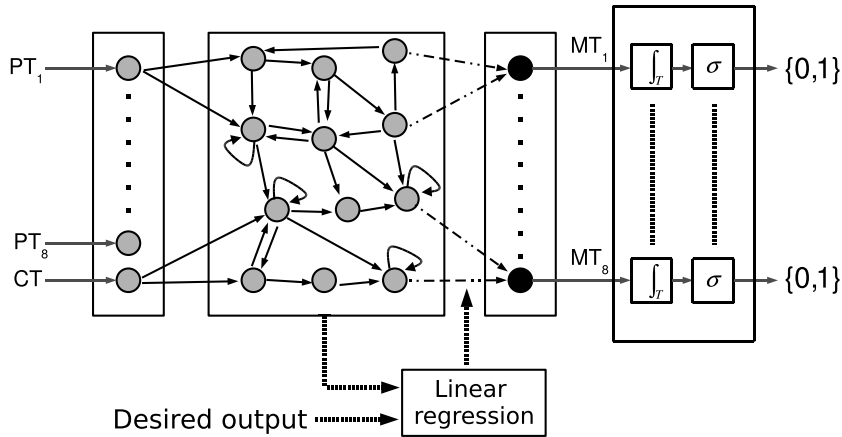


Figure 6.7: Output connection linear training and output classification.

$W_{mE}$	% of selected nets
$1 \cdot 10^{-3}$	4.5
$3 \cdot 10^{-3}$	25
$5 \cdot 10^{-3}$	49
$10 \cdot 10^{-3}$	29
$15 \cdot 10^{-3}$	21
$20 \cdot 10^{-3}$	7

Table 6.1: Percentual number of selected networks vs average connection strength of excitatory synapses measured on 1000 networks.

networks are selected according to the number of operating outputs. In tab.6.1 the results obtained for different values of  $W_{mE}$  computed on 1000 randomly generated networks are shown: the best absolute performance, measured as the number of selected networks, where obtained for  $W_{mE} = 5 \cdot 10^{-3}$ .

In conclusion, once  $W_{mE}$  is tuned, the networks selection procedure can be summarized in the following steps:

- randomly generates all the network parameters according to the defined distributions;
- train the output coefficients with the training set;
- compute the output signals and the classification error for the test set;
- if the number of outputs with classification error  $\leq 10\%$  is  $> 6$  the network is selected, otherwise discarded.

### 6.3 Performance evaluation

Following the procedure presented in the previous section, we selected 200 networks made of 500 neurons and 200 networks made of 100 neurons, storing their spiking instants while fed by a suitable long training and testing sets of tasks. Subsequently we used this data to study how the number of available neurons affects the classification performance of all the network outputs. Moreover we tested how the neurons number and the window length for the rate computing affect the performance of a SVM classifier that try to distinguish RT tasks from NGT tasks, comparing the obtained results with the ones obtained on the real data in [1].

#### 6.3.1 Linear classifier.

In order to understand how the number of available cells reduces the number of operating outputs, we applied 100 times the following procedure to all the selected networks:

- random selection of  $M\%$  of the network neurons ( $M = 50\%, 30\%, 20\%, 10\%, 5\%$ );
- training of the output layer connected only to the selected neurons;
- performance evaluation on the testing set;

Networks performance are evaluated in terms of number of operating outputs (outputs with classification error  $\leq 10\%$ ). Average performances, computed meaning the results obtained on the complete set of 200 selected networks, are shown in fig. 6.8 and fig. 6.9. We observed that networks with 500 neurons globally outperform the networks with 100 neurons (fig. 6.8 and fig. 6.9); for both cases, a clear drop of average performance is visible when the number of available neurons decreases, while the variance increases due to the decreasing of the number of available neurons.

The effect of the random selection of network neurons is better represented in fig. 6.10 and fig. 6.11. Such picture show the results obtained for each network for a sample of 80 networks of size 500 and 100, with best and worst performance displayed by bins around the average values. Comparing the average values, the effect of the random generation of the network is clear: once the number of available neurons is reduced, the performance of networks that were performing in the same interval (from 7 to 8 outputs operating) are pretty different, if only few neurons are available. Performance dispersion vs. the different combinations of neurons, displayed by bins around the average value, shows that for most of the networks the same performance can still be obtained with a sufficiently high number of neurons, if the best neurons are selected. .

#### 6.3.2 SVM classifier.

In order to asses how the number of the available cells and the length of the window for the rate computing influence the classification performance, when we try to distinguish RT form NGT basing on the rate activity of the available neurons, we modified the network architecture substituting the output layer with a block of spike to rate conversion followed by an SVM classifier with a radial basis functions (RBF) kernel, as shown in fig. 6.12. For the SVM classifier we adopted the freeware library LIBSVM [6].

The spiking rate for neuron  $i$  is computed as the number of spike events in a time slot of duration  $W$ :

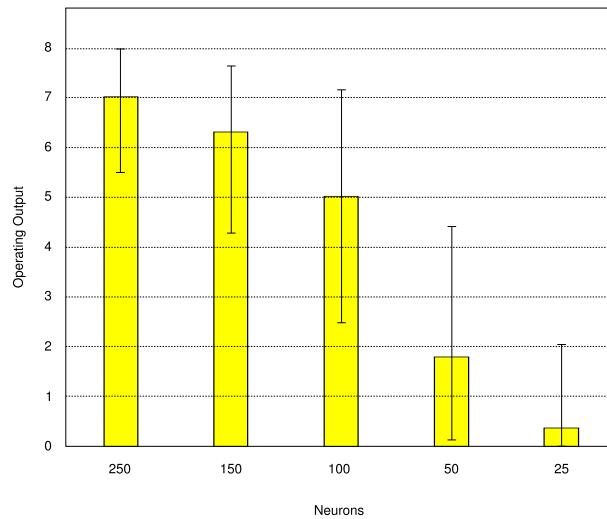


**Figure 6.8:** Average number of operating outputs measured on 200 networks of 500 neurons (yellow bars). Maximum and minimum number of operating output are displayed by bins around the average performance.

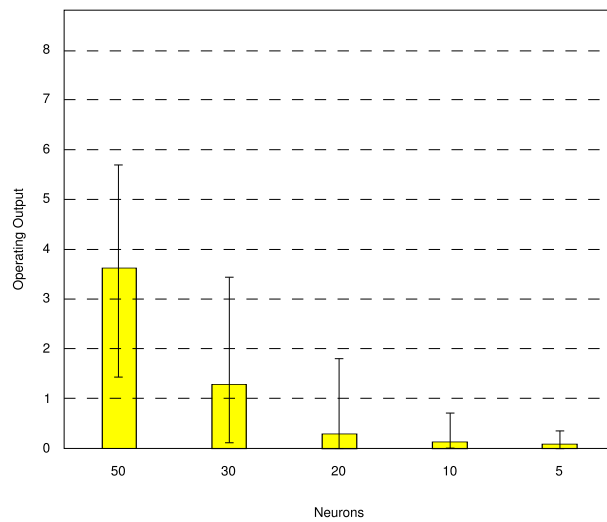


**Figure 6.9:** Average number of operating outputs measured on 200 networks of 100 neurons (yellow bars). Maximum and minimum number of operating output are displayed by bins around the average performance.

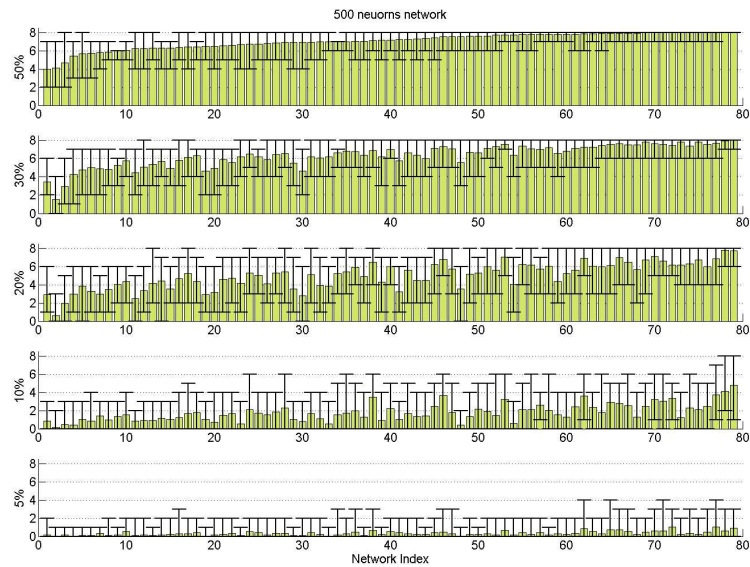


**Figure 6.10:** Average number of operating outputs of different networks of 500 neurons (yellow bars), measured over 100 random selection of different percentage of available neurons. Maximum and minimum number of operating output for each network are displayed by bins around the average performance.

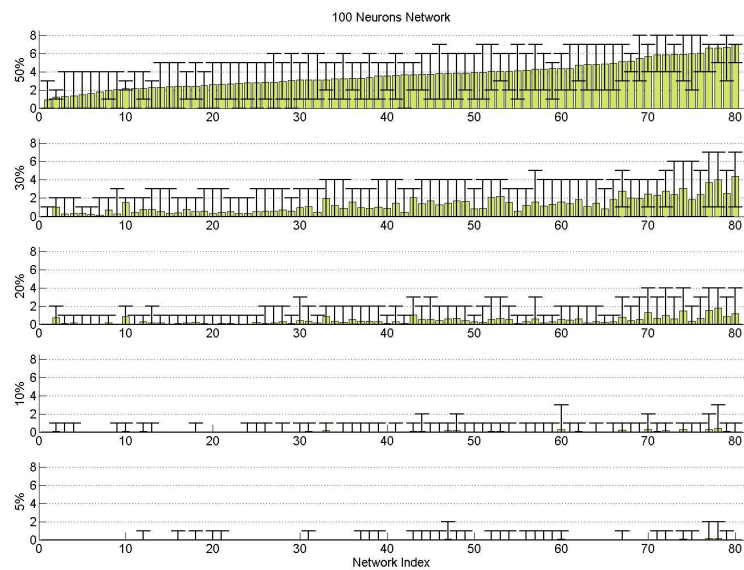


**Figure 6.11:** Average number of operating outputs of different networks of 100 neurons (yellow bars), measured over 100 random selection of different percentage of available neurons. Maximum and minimum number of operating output for each network are displayed by bins around the average performance.

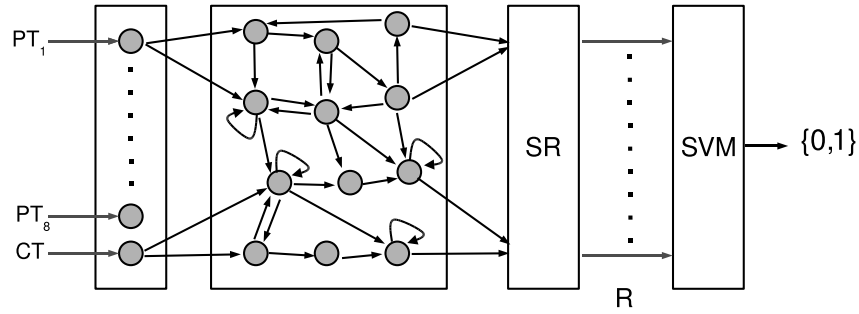


Figure 6.12: Schematic representation of the SVM based classification procedure.

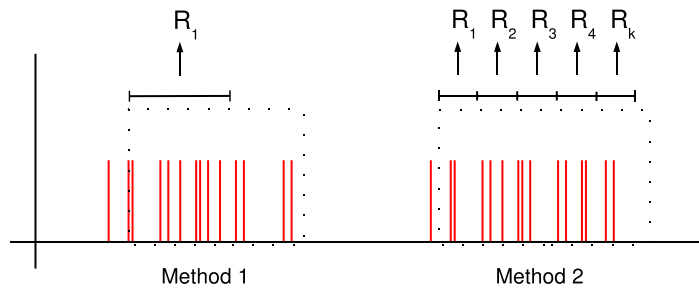


Figure 6.13: Methods employed for rate computing.

$$R_i(k) = \frac{\#\{f | k \cdot W \leq t_i^{(f)} < (k+1) \cdot W\}}{W} \quad \text{where } k = 1, 2, \dots, \left\lfloor \frac{T_{rec}}{W} \right\rfloor \quad (6.19)$$

where  $T_{rec}$  is the epoch duration. In order to model the two different data analysis procedures and verify some neurophysiologists experimental evidence about the effect of the window length in classification based on rates, we used two different methods to compute rate from spike train. As shown in fig. 6.13, in the first method we take a portion or the whole epoch of interest and compute a rate value for each neuron, obtain a rate vector  $\bar{R}$ . This method resembles the first data analysis procedure presented in section 3.2. In the second method we split the whole epoch of interest in not overlapping windows of constant length, computing a rate value for each neuron, obtain thus a rate vector for each window. This method resembles the second data analysis procedure presented in section 3.2.

Finally, we applied 100 times on the rate datasets obtained through the conversion methods the following procedure:

- random selection of  $M\%$  of the network neurons ( $M = 50\%, 30\%, 20\%, 10\%, 5\%$ );
- grid search to tune the SVM classifier parameters  $C$  and  $\gamma$ ;
- training of the output layer connected only to the selected neurons;
- performance evaluation on the testing set.

For both methods, networks performances were evaluated in terms of percentage number of correctly classified tasks.

**Method one.** Average performance of method one for different numbers of available neurons and window lengths are shown in fig. 6.14. Such curves were obtained with 200 networks of size 100, first averaging the results obtained by each network with 100 random neurons selections and then averaging such mean values above all the networks. Best and worst performances are displayed by bins around the average values. Like for the linear classifier, a clear drop of the average performance is noticed when the number of available neurons decreases. In particular, the effect of the number of available neurons on networks performance is highlighted in pic.6.16 (gray panel), where the results obtained with a sample of 50 networks setting  $w = 30$  ms are shown. Like for the linear classifier, the reduction of the number of available neurons degrades the average performance and increases its variance.

Best average results were obtained for  $W = 10$  ms; a slight drop of performance as the window length increases is visible. The effect of the window length for rate computing can be better evaluated in pic.6.15 (gray panel), where the results obtained by each network are averaged above 100 random selection of 20 % of all the neurons. Such result seems to be in contradiction with the experimental evidence presented in some work in literature where it's argued that classification accuracy should increase by increasing the length of the window for rate computing. This contradiction is probably a model limitation due to the dynamic behaviour of the network chosen to solve the proposed tasks: short-term memory. In network with short term memory property the state excited by an inputs sequence tends to vanish as  $T \rightarrow \infty$  and therefore, increasing the window length we don't add any information useful for classification purposes but on the contrary add more uncertainty about the network state.

**Method 2.** Average performance of method two for different numbers of available neurons and window lengths are shown in fig. 6.17. Such curves were obtained with 200 networks of size 100, first averaging the results obtained by each network with 100 random neurons selections and then averaging such mean values above all the networks. Best and worst performances are displayed by bins around the average values. Average performance obtained with method two are generally worst than performance obtained with method one. Such result was expectable since method two represents a more complex classification problem. In particular, while for big values of window length (80 ms and the whole epoch) performances are almost the same, for smaller values performance of method one are sensibly worst. This is due to the presence of many rate vectors belonging to the last part of the tasks epoch, where the network memory is fading and classification is therefore more difficult.

Once again a clear drop of the average performance is observed when the number of available neurons decreases. In particular, the effect of the number of available neurons on networks performance is highlighted in pic.6.16, where the results obtained with a sample of 50 networks setting  $w = 30$  ms are shown. By increasing the window length we observed

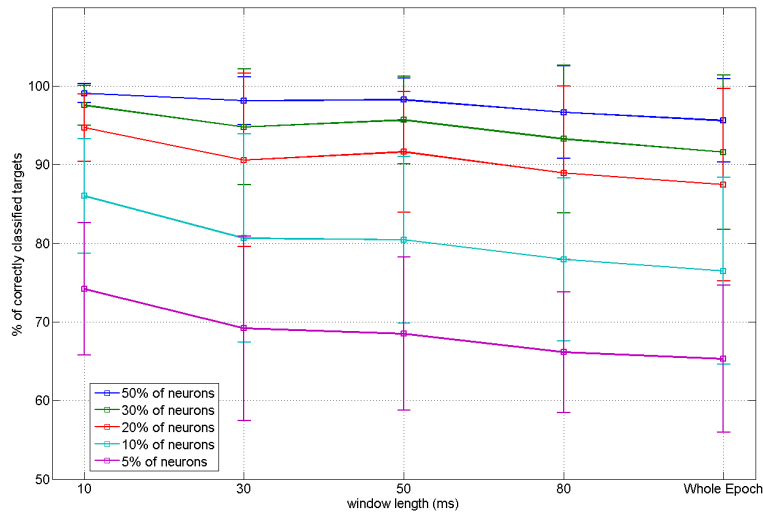


**Figure 6.14:** Average percentage number of correctly classified tasks of method 1, for different numbers of available neurons and rate computing window lengths. Performances were measured and averaged on 200 networks of 100 neurons. Maximum and minimum performance are displayed by bins around the average values.

an increasing of the average performance, until an optimum value is reached. Such value seems to be dependent by the neurons number: around 80 ms for 50%, 30% and 20% and around 50 ms for 10% and 5%. The effect of the window length for rate computing can be better evaluated in pic.6.15, were the results obtained by each network are averaged above 100 random selection of 50 % of all the neurons. Such results are qualitatively similar to the ones obtained with method one.

## 6.4 Discussion

The goal of the project presented in this chapter was the devotement of an artificial neural microcircuit model to support different conclusion derived from an experimental data analysis conduced on in vivo recorded neural activity of primate monkeys.

The proposed model is based on a liquid state machine approach [24]. The model includes leaky integrate and fire neurons and chemical synapses models. The design procedure developed is based on a random generation of the network topology, according to some biological motivated settings for the main parameters. The proposed model is able to learn and solve, with a satisfactory level of accuracy, simple abstract representations of the behavioural tasks performed by real monkeys presented in [2][3].

The aim of this study was the investigation of the effect of some critical parameters in classification procedure based on the analysis of neural activity measured at the level of individual cells. Such parameters are the number of simultaneously available cells and the length of the window used for the spiking rate computation.

The results obtained with the artificial model highlighted the critical role of these parameters in the success of data analysis and classification procedures based on neural spike trains. In particular, the performance bound obtained are similar to one observed

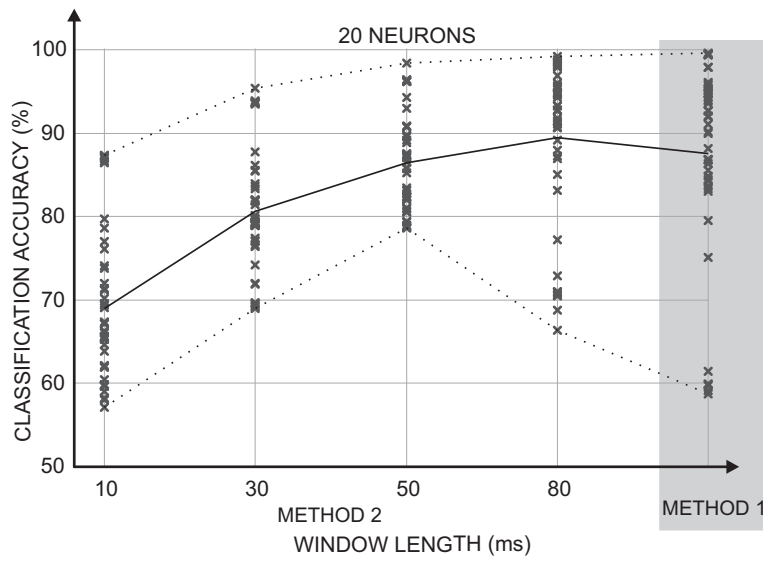


Figure 6.15: Average percentage number of correctly classified tasks of method 1 and 2, for different rate computing window lengths with 50% of network neurons available. Performance were measured and averaged on 200 networks of 100 neurons.

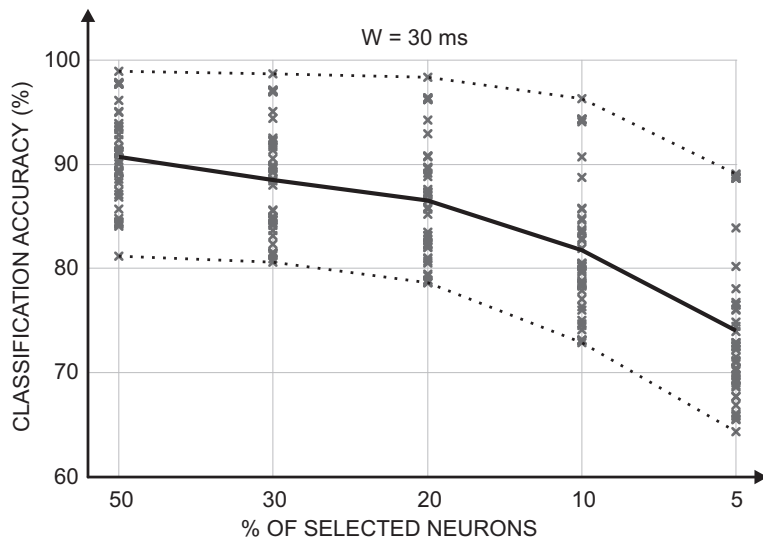
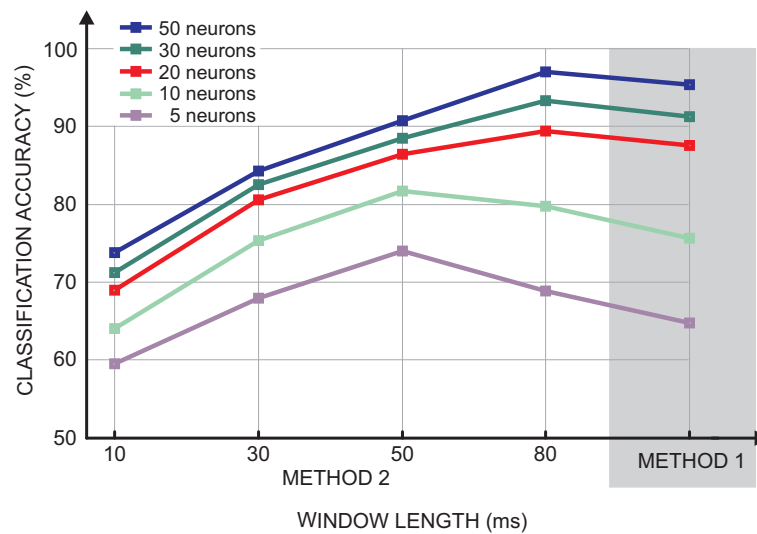


Figure 6.16: Average percentage number of correctly classified tasks of method 1 and 2, for different number of available neurons, with  $W=30$  ms. The performance were measured and averaged on 200 networks of 100 neurons. Maximum and minimum performance are displayed by bins around the average values.



**Figure 6.17:** Average percentage number of correctly classified tasks of method 1 and 2, for different numbers of available neurons and rate computing window lengths. The performance were measured and averaged on 200 networks of 100 neurons.

applying the same classification procedure on real data in [1].

Possible developments of this project can include:

- study and comparison of properties of the selected networks;
- investigation of the literature to understand deeply the dynamical properties of the model and try to overcome to its limitations and model more complex task requiring longer memory [4][7][8][23][25][21];
- use of biological motivated criteria [26][15] and prior information about how topology is influenced by learning process[16];
- use of more complex and more biological related neurons models [11];
- use of more complex and more biological related synapses models [10];

### Publications

1. A. Palladini, J. Acimovic, M. Hasler: **Modeling behavioral tasks to asses visual information integration and Motor information encoding in parietal cortex**. Proceedings of the International Symposium on Nonlinear System Theory and Application 2008 (NOLTA 2008). **Awarded as best student paper.**



---

## Bibliography

---

- [1] J. Acimovic, A. Battaglia-Meyer, R. Caminiti, and M. Hasler. Automatic methods for motor intention recognition from spike rates. In *International Symposium on Nonlinear Theory and its Applications*, pages 361–364. NOLTA, September 2007. [cited at p. 41, 45, 41, 45, 111, 120, 126, 133]
- [2] A. Battaglia-Meyer, M. Mascaró, M. Brunamonti, and R. Caminiti. The over-representation of contralateral space in parietal-cortex: a positive image of directional motor compensation of neglect? *Cerebral Cortex*, 15:514–525, 2005. [cited at p. 40, 41, 43, 40, 41, 43, 111, 116, 120, 131]
- [3] A. Battaglia-Meyer, M. Mascaró, and R. Caminiti. Temporal evolution and strength of neural activity in parietal cortex during eye and hand movement. *Cerebral Cortex*, 17:1350–1363, 2007. [cited at p. 40, 41, 43, 40, 41, 43, 111, 116, 120, 131]
- [4] N. Brunel and V. Hakim. Fast global. *Neural Computation*, 11:1621–1671, 1999. [cited at p. 133]
- [5] H. Burgsteiner, M. Krüger, A. Leopold, and G. Steinbauer. *Movement prediction from real-world images using a liquid state machine*, volume 3533/2005 of *Innovation in Applied Artificial Intelligence*. Springer Berlin / Heidelberg, 2005. [cited at p. 111, 122, 124]
- [6] C. Chang and C. Lin. *LIBSVM: a library for support vector machines*. Department of Computer Science, National Taiwan University, Taipei. [cited at p. 126]
- [7] A. Compte, N. Brunel, P. s. Goldman-Rakic, and X. Wang. Synaptic mechanism and network dynamics underlying spatial working memory in a cortical network model. *Cerebral Cortex*, 10:911–923, September 2000. [cited at p. 133]
- [8] J. Eggert and J.L. van Hemmen. Modeling neural assemblies: theory and implementation. *Neural Computation*, 13:1923–1974, 2001. [cited at p. 133]
- [9] Gerstner and W. Kistler. *Spiking neuron models*. Cambridge University Press, 2002. [cited at p. 112, 113]
- [10] A. Gupta, Y. Wang, and H. Markram. Organizing principles for a diversity of gabaergic interneurons and synapses in the neocortex. *Science*, 287:273–278, 2000. [cited at p. 122, 133]
- [11] E.M. Izhikevich. Which model to use for cortical spiking neurons? *IEEE Transactions on Neural Networks*, 15(5), September 2004. [cited at p. 133]

- [12] H. Jaeger. Short term memory in echo state networks. Technical Report 152, GMD – Forschungszentrum Informationstechnik GmbH, March 2002. [cited at p. 111, 120]
- [13] Herbert Jaeger. The echo state approach to analysing and training recurrent neural networks. Technical report, GMD – Forschungszentrum Informationstechnik GmbH, 2001. [cited at p. 112, 115, 116]
- [14] Herbert Jaeger, Mantas Lukoševičius, Dan Popovici, and Udo Siewert. Optimization and applications of echo state networks with leaky- integrator neurons. *Neural Networks*, 20(3):335–352, April 2007. [cited at p. 121, 122]
- [15] C. Jhonassonm and A. Lansner. Towards cortex sized artificial neural systems. *Neural Networks*, 20:48–61, 2007. [cited at p. 133]
- [16] H. Kato, K. Han-nuki, T. Kimura, and T. Ikeguchi. Emerging of self-organized structures in a neural network using two types of stdp learning rules. In *Proceedings of NOLTA 2007*, pages 429–432. NOLTA 07, 2007. [cited at p. 133]
- [17] P. Koenig, Andreas K. Engel, and Wolf Singer. Integrator or coincidence detector? the role of the cortical neuron revisited. *Trends in Neuroscience*, 19(4):130–137, 1996. [cited at p. 123]
- [18] Robert Legenstein and Wolfgang Maass. Edge of chaos and prediction of computational performance for neural circuit models. *Neural Networks*, 20(3):323–334, April 2007. [cited at p. 122]
- [19] M. Lukosevicius and H. Jaeger. Overview of reservoir recipes. Technical Report 11, Jacon University – School of Engineering and Science, July 2007. [cited at p. 121]
- [20] W. Maas, T. Natschlager, and H Markram. Real-time computing without stable states: a new framework for neural computation based on perturbation. *Neural Computation*, 14(11):2531–2560, 2002. [cited at p. 111, 112, 116]
- [21] W. Maass, P. Joshi, and E. D. Sontag. Computational aspects of feedback in neural circuits. *PLoS Computational Biology*, 3(1), 2007. [cited at p. 133]
- [22] H. Markram, Y. Wang, and M. Tsodyks. Differential signalling via the same axon of neocortical. *Proc. Natl. Acad. Sci.* 95, 95:5323–5328, 1998. [cited at p. 114]
- [23] M. Mattia and P. Del Giudice. Population dynamics of interacting spiking neurons. *Physical Review E*, 66(5), 2002. [cited at p. 133]
- [24] T. Natschlager and W. Maas. Finding the key to a synapse. Technical report, Institut for Theoretical Computer Science – Technische Universität Graz. [cited at p. 113, 114, 131]
- [25] A. Roxin, N. Brunel, and David Hansel. The role of delays in shaping spatio-temporal dynamics of neural activity in large networks. *Physical review letters*, 94, 2005. [cited at p. 133]
- [26] A. M. Thomson, D.C. West, Y. Wang, and A. P. Bannister. Synaptic connections and small circuits involving excitatory and inhibitory neurons in layers 2–5 of adult rat and cat neocortex: triple intracellular recordings and biocytin labeling *in vitro*. *Cerebral Cortex*, 12:936–953, 2002. [cited at p. 122, 133]